In presenting this thesis in partial fulfillment of the requirements for an advanced degree at Idaho State University, I agree that the Library shall make it freely available for inspection. I further state that permission for extensive copying of my thesis for scholarly purposes may be granted by the Dean of the Graduate School, Dean of my academic division, or by the University Librarian. It is understood that any copying or publication of this thesis for financial gain shall not be allowed without my written permission.

Signature _____

Date _____

Micro-tensile Characterization of Select TRISO-coated Particle Layers and Interlayer Regions

by

Tanner Mauseth

A dissertation

Submitted in partial fulfillment

of the requirements for the degree of

Doctor of Philosophy in the Department of Nuclear Engineering

Idaho State University

Fall 2023

To the Graduate Faculty:

The members of the committee appointed to examine the dissertation of Tanner Mauseth find it satisfactory and recommend that it be accepted.

_____
Mary Lou Dunzik-Gougar
Major Advisor, Committee Chair

_____
Fei Teng
Committee Member

_____
Daniel LaBrier
Committee Member

_____
Amir Ali
Committee Member

_____
John Dudgeon
Graduate Faculty Representative

Acknowledgements

The credit of this work goes to the guidance and leadership of Dr. Mary Lou Dunzik-Gougar, Dr. Fei Teng, Dr. Amir Ali, and Dr. Daniel LaBrier, the technical support and expertise of Dr. John Dudgeon at Idaho State University's Center for Archaeology, Materials and Applied Spectroscopy (CAMAS), the insight on DIC practices of Dr. Yachun Wang, the technicians from Superior Technical Services of Portland, Oregon, the microscopy experts from Bruker Hysitron's headquarters in Eden Prairie, Minnesota, the microscopy experts and support staff from the Microscopy and Characterization Suite (MaCS) at the Center for Advanced Energy Studies (CAES), the Idaho National Laboratory (INL) microscopy experts and support staff from the Idaho National Laboratory Research Center (IRC) and Irradiated Materials Characterization Laboratory (IMCL), the love and endless support of my wife, and to all my friends and family who kept pushing me to overcome any and all obstacles set before me along this journey.

This dissertation work is financially supported through the Department of Energy's Nuclear Energy University Program (NEUP) grant for project 17251. We thank Dr. Isabella Van Rooyen for providing the surrogate fueled TRISO particle samples and the INL for providing the unirradiated and irradiated fueled TRISO particle samples in this dissertation.

Table of Contents

List of Figures

List of Tables

List of Equations

Micro-tensile Characterization of Select TRISO-coated Particle Layers and Interlayer Regions

Dissertation Abstract--Idaho State University (2023)

A novel micro-tensile sample fabrication technique for determining the tensile strength of the buffer, IPyC, and buffer-IPyC interlayer regions of surrogate fueled (ZrO_2), unirradiated fueled (UCO), and irradiated fueled (UCO) TRISO fuel particle layers was refined and implemented. Copper micro-tensile samples served as baseline materials to verify the methods used. Data from tensile tests performed in this dissertation, while limited in number, were analyzed using standard and Weibull statistics. While the buffer layer was weakest and the IPyC layer was strongest for the surrogate and unirradiated TRISO particles, the buffer-IPyC interlayer region was weakest and the IPyC layer was strongest for the irradiated TRISO particles. These results are desirable because IPyC layer fractures are strongly associated with buffer layer adhesion. All buffer-IPyC interface samples fractured either in the buffer layer region or at the buffer-IPyC interface, yet some of the buffer-IPyC interlayer samples displayed stress-strain and fracture behavior more comparable to the IPyC layer than the buffer layer. These results suggest the buffer-IPyC interlayer region has unique properties, perhaps associated with pyrocarbon infiltration into the buffer layer during particle coating. The clear increase of porosity, major reduction of the ultimate tensile strength, and major reduction of the Weibull modulus/shape parameter in the irradiated TRISO particles buffer-IPyC interlayer region suggests that irradiation induced porosity is the primary cause of delamination between the TRISO particles buffer and IPyC layers.

Key words: Tristructural isotropic (TRISO); buffer carbon; inner pyrolytic carbon (IPyC); focused ion beam (FIB); PicoIndenter; micro-tensile.

1.0 Introduction

1.1 Background

The United States Department of Energy founded the Generation IV International Forum (GIF) in the year 2000 to assess future energy needs and to improve nuclear energy technology. The GIF had four main objectives in mind in regard to nuclear power: sustainability, economic competitiveness, safety and reliability, and proliferation resistance and physical protection. The goal of sustainability aims to provide energy now that can be used indefinitely into the future. This encompasses areas such as waste management, resource utilization, transportation, and hydrogen production. The goal of economic competitiveness aims to make nuclear energy more financially attractive in comparison to other energy sources. This includes strategies such as reducing operating and capital cost through increased efficiency, design simplification, advances in fabrication and construction techniques, and standardization and modularization techniques. The goal of safety and reliability aims to remove the stigma surrounding nuclear energy and to provide safe living and operating conditions. Generation IV reactors plan to accomplish this by the use of inherent safety features and designs. The goal of proliferation resistance and physical protection aims to make access to nuclear materials more secure in order to protect against unintentional and intentional threats to nuclear facilities. With these goals in mind, ten separate countries set out to tackle different nuclear reactor designs in order to accomplish the objectives set out by the GIF. The United States decided to focus on two priorities: develop the Next Generation Nuclear Plant (NGNP) Program in the mid-term and develop a fast reactor to improve proliferation resistance in the long-term (Chapin et al., 2004). A subdivision of the NGNP was the Advanced Gas Reactor (AGR) Fuel Development Program. This program aimed to further advanced fabrication and characterization technologies and conduct irradiation and safety performance testing for the

licensing of TRISO particle fuel, which was meant for use in future high temperature gas reactors (HTGR)(Office of Nuclear Energy, 2009). While the NGNP no longer exists, TRISO fuel particle testing is still in continuation and is being sought after for use in future HTGRs and other nuclear reactor types. The HTGR design, using TRISO particles as its fuel source, offers a promising solution for our future energy needs.

1.11 HTGRs

HTGRs possess numerous qualities that differentiate them from other reactor types, including lower costs overall, a safer waste stream, inherent safety, proliferation resistance, and high performance characteristics that would enable nuclear to provide more energy to the future United States energy supply. These qualities are made possible by a few defining design and physical characteristics of the HTGR, such as helium coolant that has a high exit temperature, graphite moderated core, and TRISO particle fuel. The HTGR typically has a helium exit temperature in the range of 850°C to 900°C that provides a 40 to 48% thermal efficiency by the use of the recuperated Brayton cycle. HTGRs possess greater electrical generation efficiency for the same thermal power and reduced component complexity in comparison to light water reactors, reducing the large capital cost usually associated with the current nuclear plants. It should be noted, however, that the first generation of HGTRs will still be expensive and that the reduced price will only come into effect once a number of HTGRs have been built. The high temperature that leads to HTGR electric generation efficiency also maximizes burn up efficiency of the fuel, minimizing the nuclear waste stream. The HTGR is inherently safe through its graphite moderated cores characteristics, being that the graphite core conducts and absorbs away excessive core heat even if coolant is lost. This enables the HTGR to passively shut down if there is an accident. The encapsulation of fuel in TRISO particles also makes the HTGR more proliferation resistant than

other fuel forms. These performance characteristics maximize electrical generation efficiency and enable efficient thermochemical cycles for hydrogen production, providing a potential foot hold in the future United States energy grid for HTGR technology to thrive (Parma et al., 2003).

There are two main types of HTGR core design: prismatic core and pebble-bed core. In a prismatic block fuel assembly, the TRISO fuel particles are molded into cylindrical fuel compacts before being inserted into hexagonal graphite fuel elements, as seen in Fig. 1 (Kallman, 2013). Isolated fuel and coolant holes are drilled into the graphite block with six fuel holes encompassing each coolant hole in a hexagonal formation. Prefabricated fuel compacts, around 12.5 mm-diameter by around 50 mm long contain the TRISO fuel particles in a close-packed array, mixed throughout a carbonaceous matrix. The fuel compacts are then arranged in the fuel holes (Verfondern et al., 2013).

Figure 1. From left to right: TRISO particles, fuel compacts, and graphite block matrix (IAEA, n.d.).

In a prismatic core, hexagonal moderator and fuel blocks are organized to form an inner graphite reflector, a center active fuel core, and an outer graphite reflector. In conjunction with the graphite components, the prismatic core also includes a side graphite reflector, vessel coolant

channels, and a core barrel. A schematic of this set-up is shown in Fig. 2. Helium and molten salts are the two most commonly used primary coolants in prismatic cores. The coolant enters the reactor core and flows up through the vessel coolant channels before flowing downward through the integral coolant channels in the fuel assemblies. This exposes the core barrel to the cooler inlet coolant, rather than the hotter outlet coolant, thereby reducing the operating temperature of the barrel material. Compared to a pebble-bed core, the integral coolant channels allow better core cooling, which in turn allows greater power density and total core power with prismatic block fuel (Kallman, 2013).

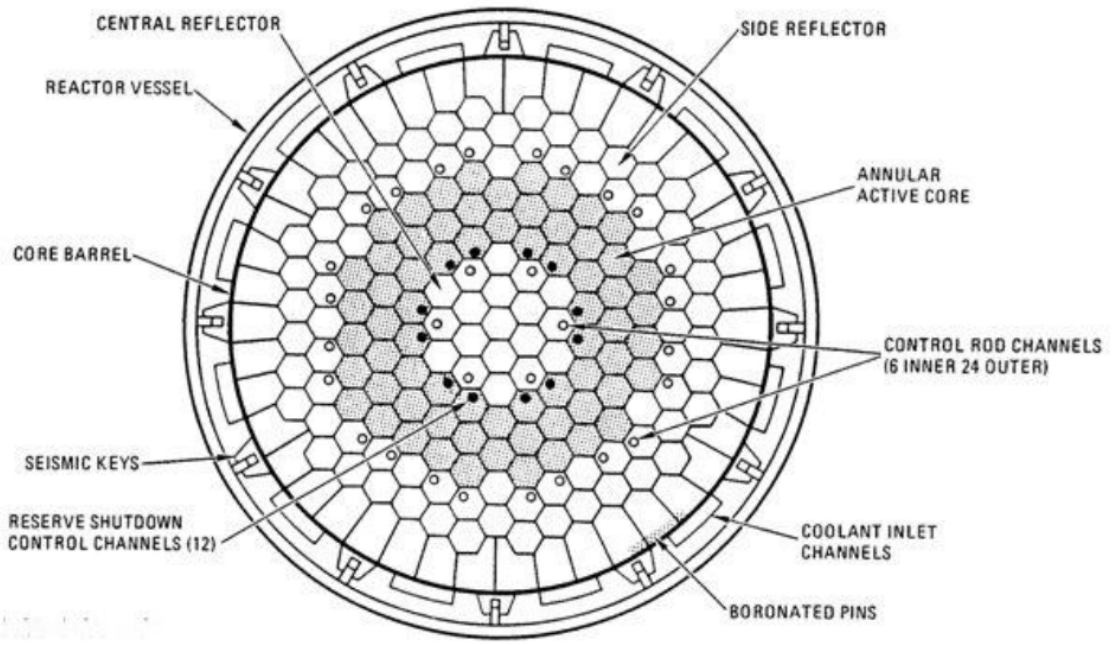

Figure 2. Diagram of prismatic reactor core assembly (IAEA, n.d.).

The prismatic core design was originally pursued in the United States of America, United Kingdom, and Japan. Today, the prismatic core continues development in the USA and Russia. Meanwhile, in Japan, the prismatic core design takes the form of a Pin-in-Block design with a

different fuel configuration and coolant path (Verfondern et al., 2013). A diagram of The Gas Turbine – Modular Helium Reactor (GT-MHR), a joint project between the United States (General Atomics) and Russian Federation program, is shown in Fig. 3 (Chapin et al., 2004).

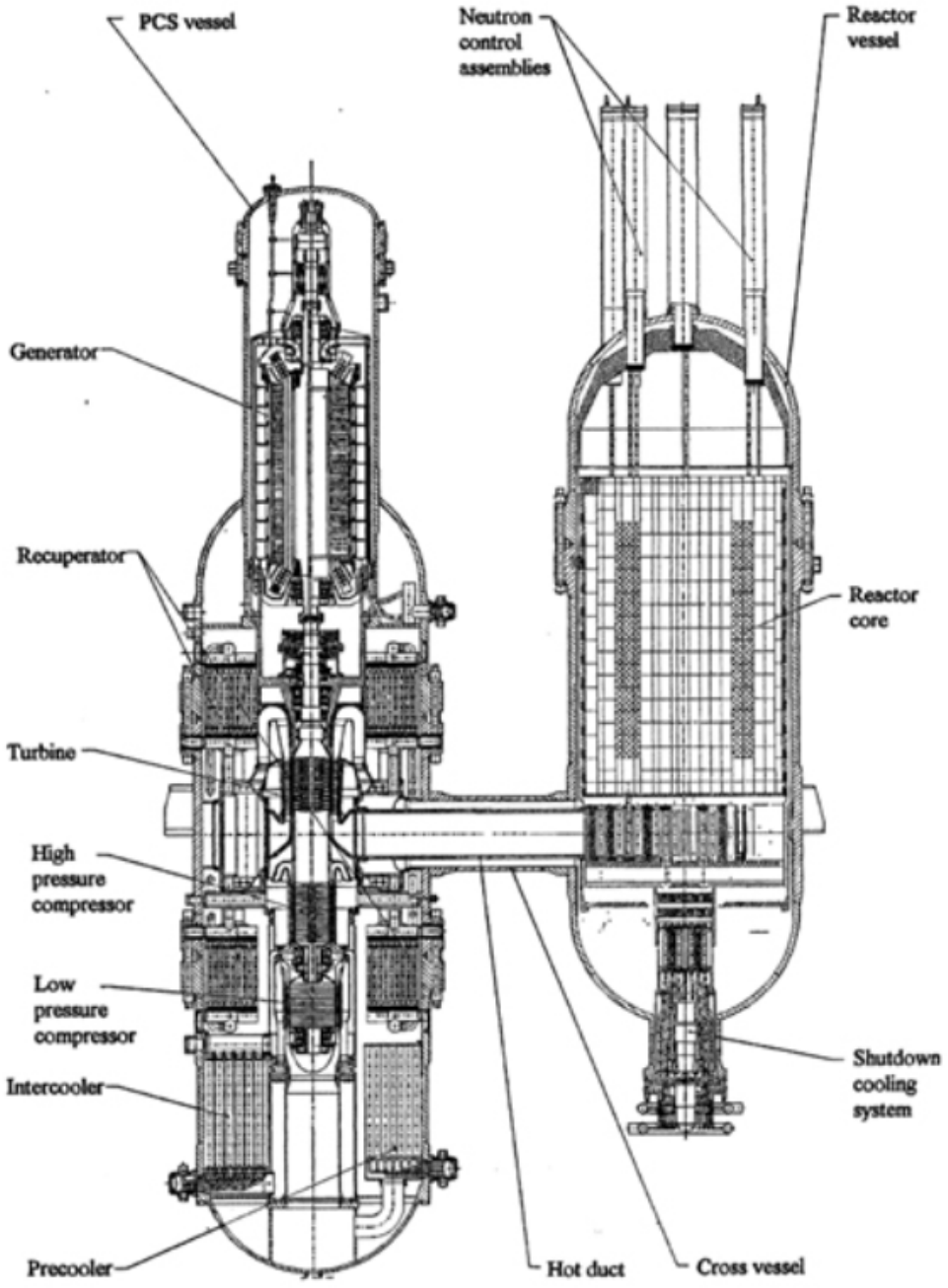

Figure 3. Schematic of The Gas Turbine – Modular Helium Reactor (GT-MHR) (Chapin et al., 2004).

In the pebble-bed reactor, spherical fuel elements approximately 60-mm in diameter are used and are referred to as fuel pebbles (as seen in Fig. 4). The pebbles are a two-part design, comprised of an inner fuel zone 50 mm in diameter encompassed by a 5 mm-thick shell of graphitized fuel matrix material. The inner fuel zone contains the TRISO particles and is homogenously dispersed within the graphitized matrix (Verfondern et al., 2013).

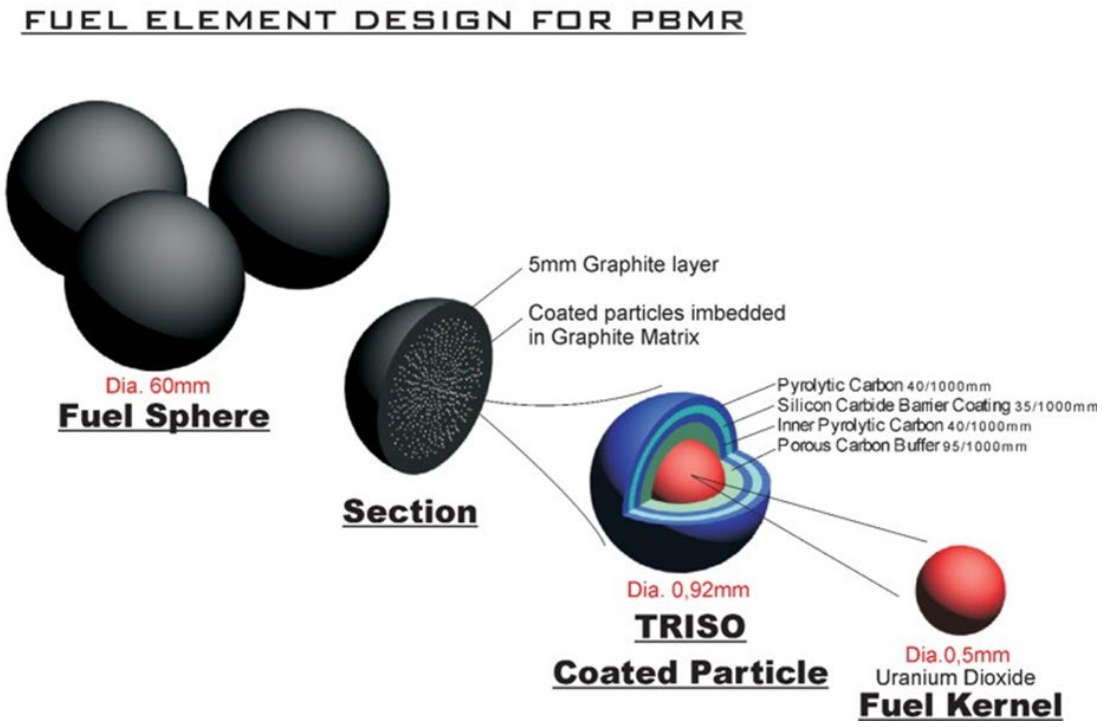

Figure 4. Components of a fuel pebble, descending in scale from left to right (PBMR, 2017).

The arrangement of the pebble-bed core is similar to the prismatic core, where prismatic fuel blocks in the active annular core region are replaced by mobile fuel pebbles. These pebbles constantly circulate downward through the core, driven by gravity (as seen in Fig. 5). The pebbles are taken from the bottom of the core, at which point their total burn-up is assessed. Active pebbles are returned to the top of the core, while spent pebbles are taken to storage/reprocessing. Much

like in a prismatic core, the inner and outer reflectors in a pebble-bed core are constructed from static moderator blocks. In the pebble design, either helium or molten salt coolant flows between the gaps of the pebbles (Kallman, 2013).

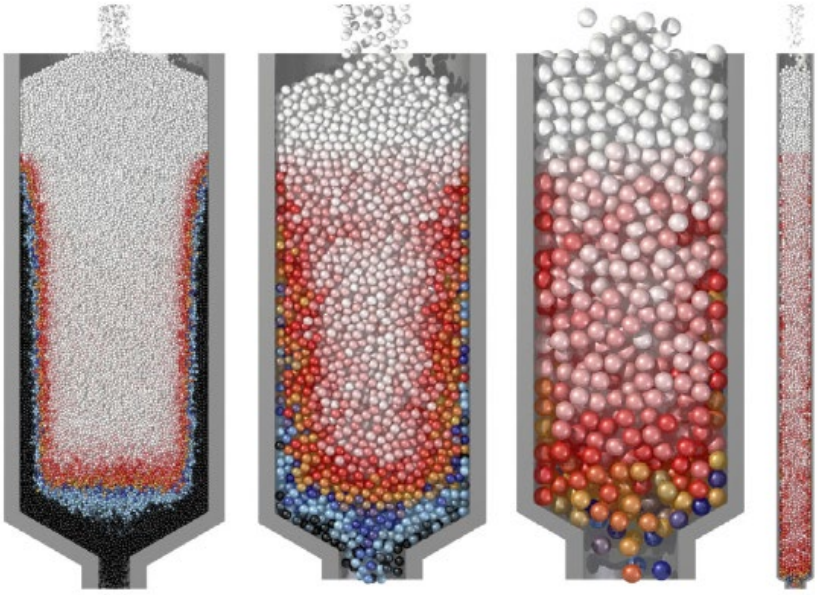

Figure 5. Visual of fuel pebbles in pebble-bed core. This particular diagram shows how varying fuel pebble sizes would arrange themselves in the core (S. Jiang et al., 2019).

The pebble bed concept was initially pursued in Germany, Russia, and South Africa, and today China is where the pebble-bed HTGR is being developed (Verfondern et al., 2013). A diagram of the HTR-10 reactor from Tsinghua University in China is shown in Fig. 6.

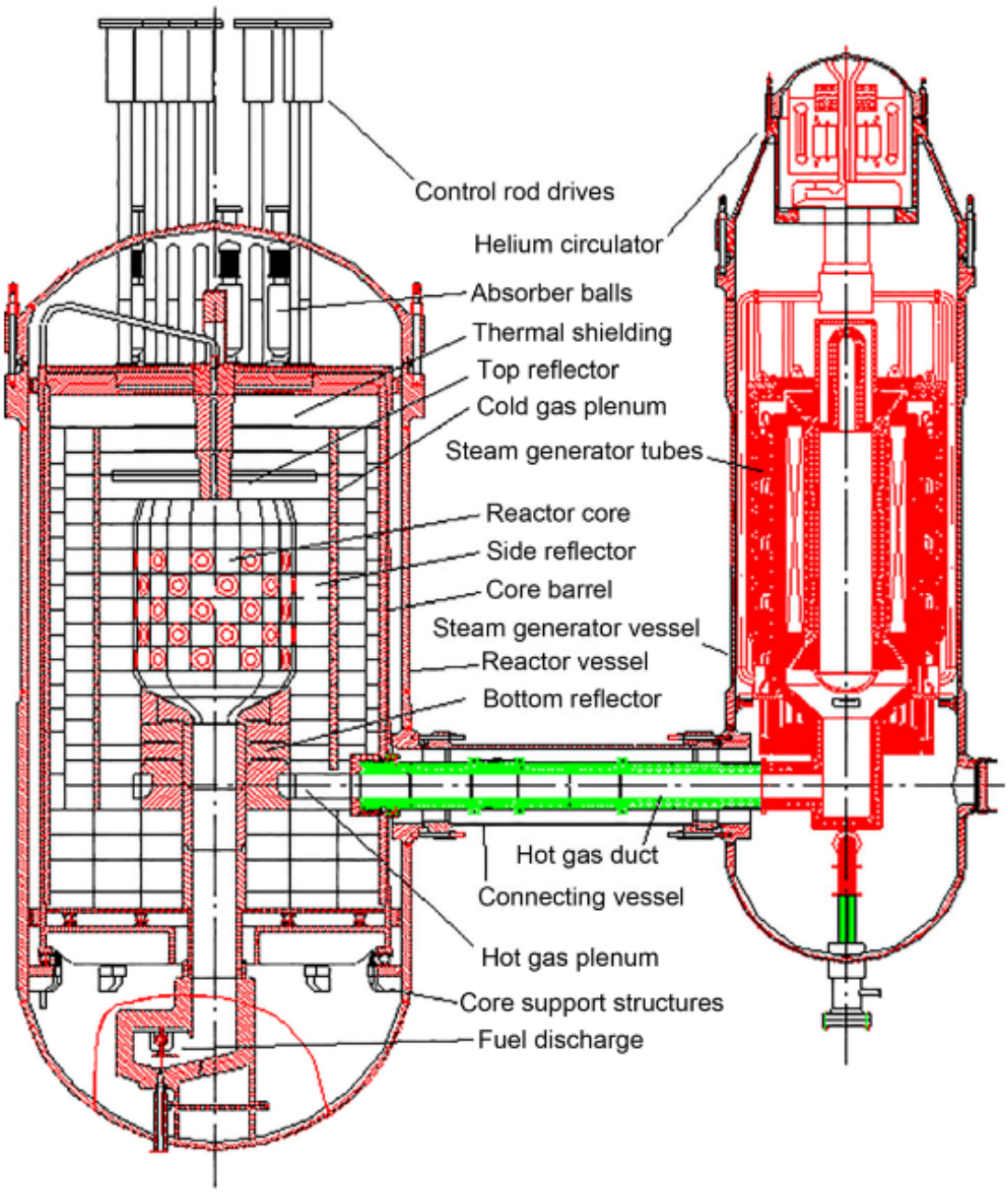

Figure 6. Schematic of the HTR-10 reactor from Tsinghua University in China (Jiang et al., 2019).

1.12 TRISO Particles

The TRISO particle is the primary fuel form used by current and future HTGR designs. The TRISO particle is ~1 mm in diameter and consists of a fuel kernel (UO_2, UCO, ThO_2, etc.) surrounded by layers of various materials that serve to protect the TRISO particle and other layers

and to contain fission products. The first layer is a low-density, porous pyrolytic carbon (PyC) layer, called the buffer, which provides void volume for the buildup of gaseous fission products freed from the fuel kernel. It also considers fuel kernel swelling and serves as a sacrificial layer to mitigate fission fragments. The second layer is a high-density, isotropic PyC layer, named the inner PyC (IPyC) layer. The IPyC layer is a gas-tight layer that shields the fuel kernel from hot, gaseous chlorine compounds during the silicon carbide (SiC) layer deposition process and provides a smooth surface for SiC layer deposition. The IPyC also aids as a diffusion barrier for gaseous and metallic fission products. During irradiation it contracts, helping to reduce tensile stresses on the SiC layer. The third layer is an isotropic SiC layer which acts as the pressure bearing element of the TRISO particle and the main metallic fission product diffusion barrier (Verfondern et al., 2013). Fission products created from the fuel contain no free oxygen, which could otherwise aggravate chemical degradation of the ceramic SiC layer. The layer begins to lose its integrity above around 1600 °C, which signifies the limiting fuel temperature under accident conditions (Kallman, 2013). The fourth layer is a high density, isotropic PyC layer, called the outer PyC (OPyC) layer. This layer functions as the outermost diffusion barrier for gaseous and metallic fission products. Much like the IPyC layer, it contracts during irradiation. This property assists in reducing tensile stress on the SiC layer. The OPyC also shields the SiC layer during particle handling and pebble/compact creation and offers a bonding surface for the over coating process (Verfondern et al., 2013). These particles are combined with graphite powder and binders before being shaped and formed into the final fuel element (Kallman, 2013). Fig. 7 and 8 depict the various layers contained within a TRISO particle.

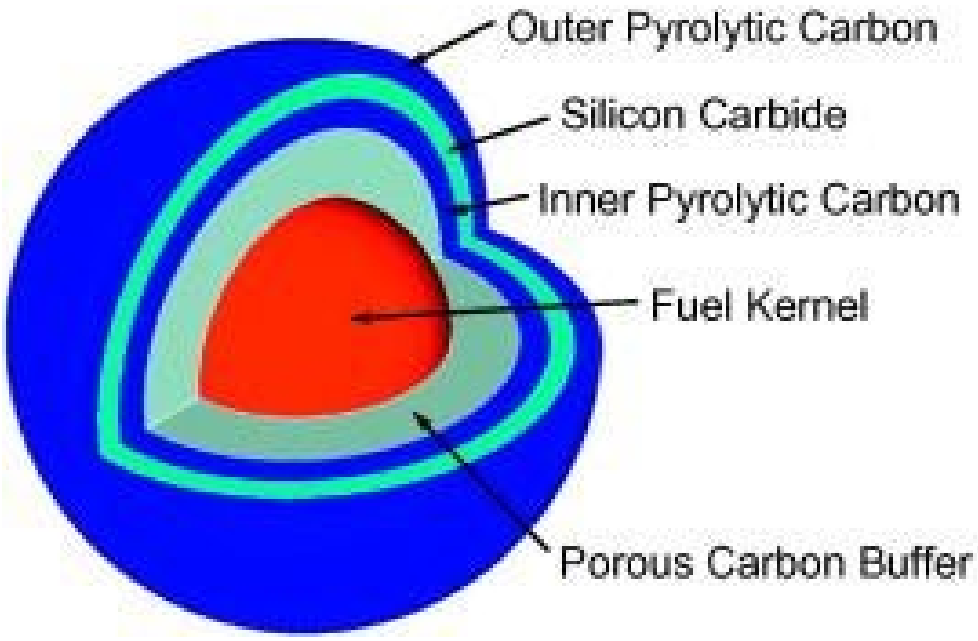

Figure 7. Illustration of the various layers of a TRISO particle (Hales et al., 2013).

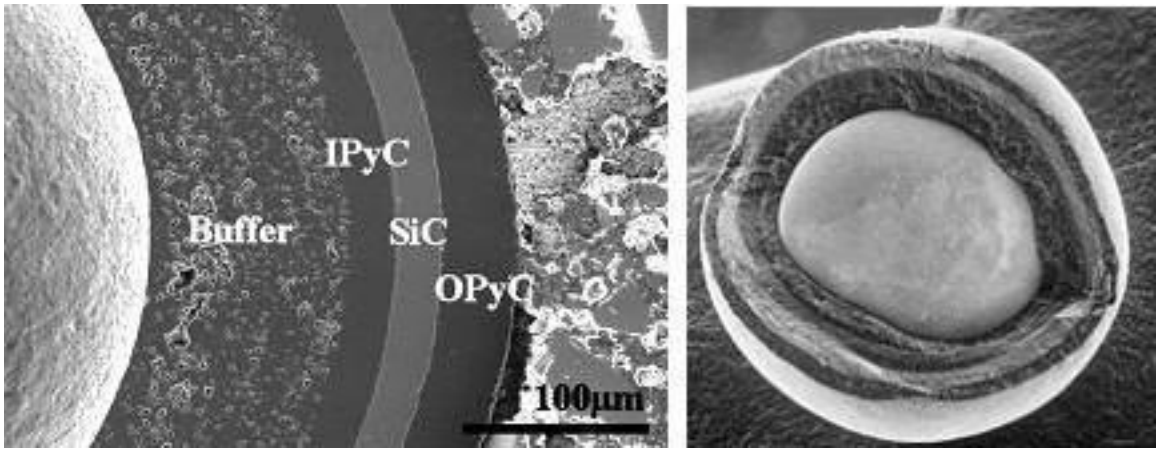

Figure 8. Scanning electron microscope (SEM) image of an exposed TRISO particle (Honorato, 2011).

According to Verfondern et al. (2013), the conditions under which layer deposition takes place are very important as they determine the material properties of the coated particles formed. Parameters such as time, temperature, pressure, gas composition and gas ratios all play an important role in fixing the coated particle properties. Therefore, understanding the process in

which TRISO particles are formed is vital in understanding how TRISO particles will perform. TRISO particle kernels receive their four coating layers in a fluidized bed coating furnace in a procedure termed chemical vapor deposition (CVD). A flowchart for the coating process is shown in Fig. 9. The deposition gases in the furnace cause the kernels to float, where organic gases are designed to decompose and deposit at up to 1600°C. The films formed on the kernels are termed as pyrolytic, as they undergo pyrolysis of organic materials brought about by the high temperatures and form the carbonaceous layers on the TRISO particle. All the constituent layers formed in this process are deposited in an uninterrupted sequential process by the same fluidized bed coating furnace, as seen in Fig. 10 (Verfondern et al., 2013). Changing the parameters at any point in the CVD process will alter the final layer thickness for any of the four layers and will affect the final material properties of the TRISO particle.

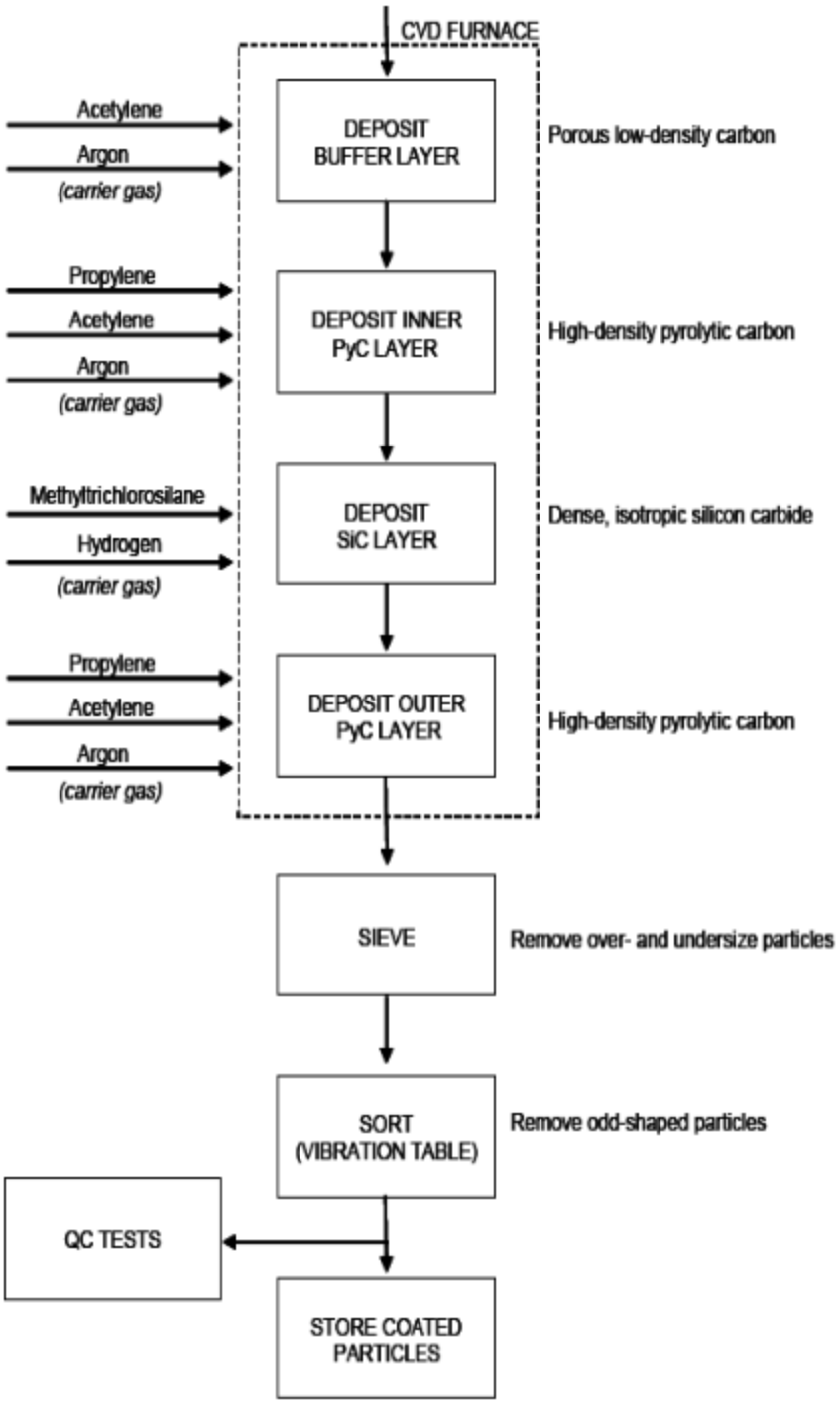

Figure 9. Various steps of the chemical vapor deposition process (Verfondern et al., 2013).

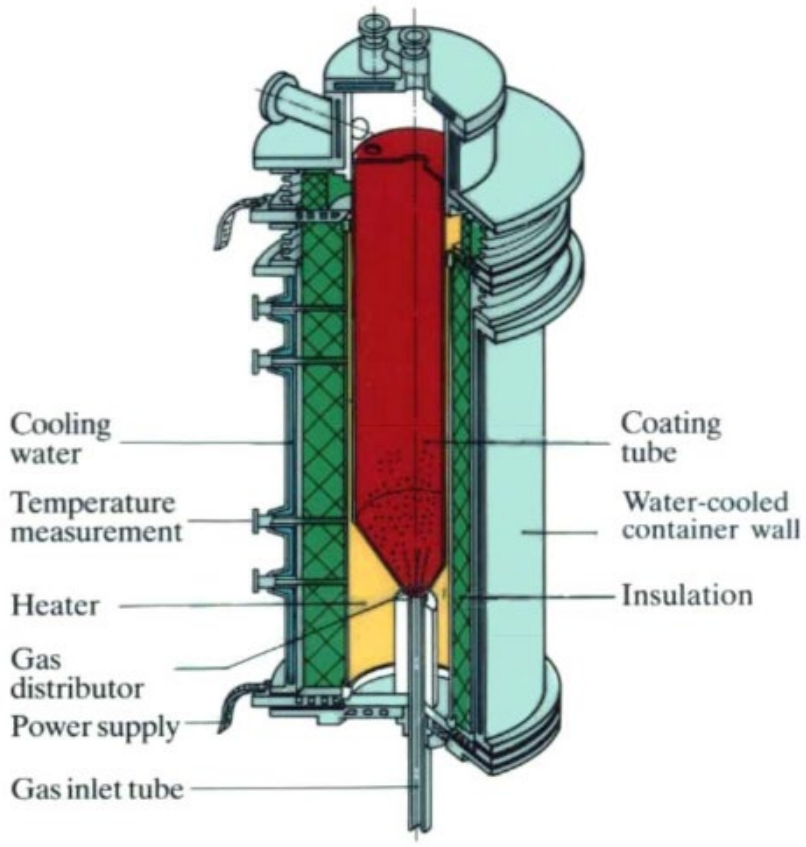

Figure 10. Illustration of a fluidized bed coating furnace (Verfondern et al., 2013).

TRISO fuel particles offer a very flexible fuel arrangement by fundamentally separating the cooling geometry and neutronic optimization of the fuel. The fuel assembly shape, core alignment, number of coolant channels, and packing fraction of fuel particles can all be changed independently for different power levels, outlet temperatures, and fuel cycles. The fuel flexibility can encompass different fuel cycles, such as a closed fuel cycle with a fast or thermal neutron spectrum. However, the current SiC layer in TRISO fuel particles has increased vulnerability to fission product release under the fast neutron conditions shown in the U-Pu closed fuel cycle. TRISO fuel particles possess other inherent advantages within reactor cores. With each fuel particle being able to retain its own fission products, it results in very little radioactive release

during operation. Furthermore, the carbide layers retain fission products even after the operational lifetime of the fuel is over. TRISO fuel particles embody an ideal final waste form, if they can be disconnected from the large amounts low-level radioactive graphite waste. Because of this, TRISO fuel may also require less overpacking than traditional LWR fuel, reducing the total amount of repository space needed (Kallman, 2013).

1.13 Buffer-IPyC Interlayer

The mechanical and structural properties of the IPyC and buffer carbon layers are the focus of this dissertation work and are very important when determining the material properties and structural integrity of TRISO particle fuel. As mentioned in the TRISO particle section, the parameters of the chemical vapor deposition process can affect the performance of the IPyC layer. In particular, the deposition temperature and coating gas fraction (acetylene-propylene ratio) greatly affected the measured properties of IPyC. This was found in a study done by Hunn & Lowden (2005), where polished cross-sections of TRISO particle layers were viewed under an ellipsometry microscope to determine the average diattenuation and thus anisotropy of the IPyC layer. A plot of this diattenuation can be viewed in Fig. 11.

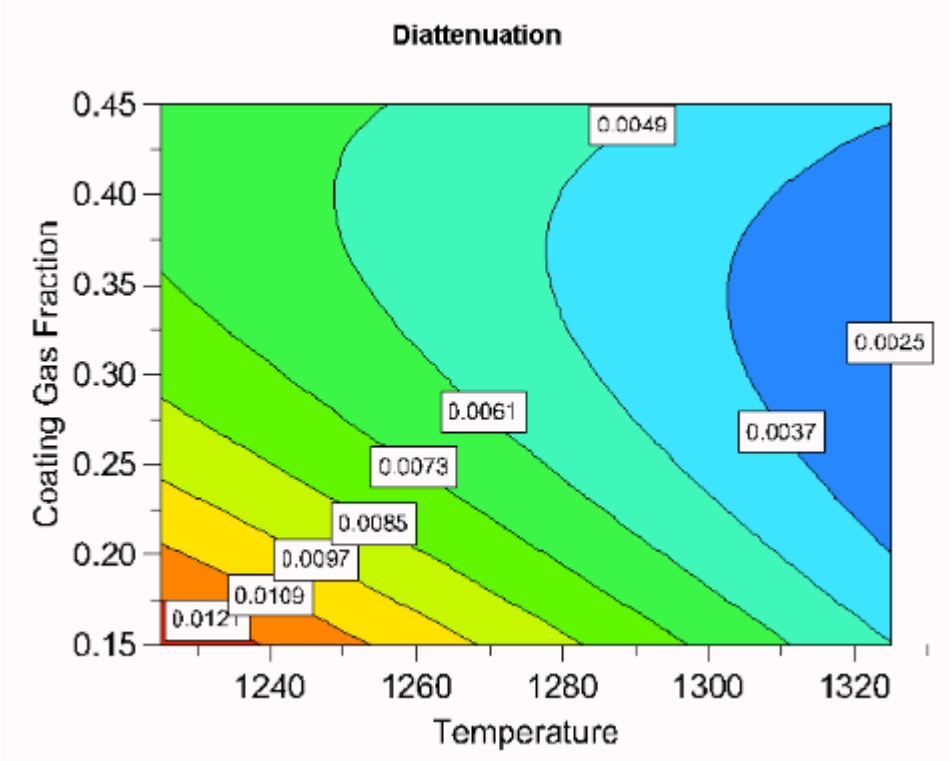

Figure 11. Plot of diattenuation that shows the dependence on both coating temperature and coating gas fraction (Hunn & Lowden, 2005).

Variance in the diattenuation (and thus variance in isotropic configuration) of the IPyC layer can have important physical repercussions. The inner and outer pyrolytic carbon layers support and stabilize the SiC layer by introducing additional compressive force through carbon coating shrinkage during neutron irradiation. This force acts against the tensile stress imposed by internal pressure buildup from fission products. However, it has been shown that excessive contraction of the PyC layers can lead to cracking which can devolve into a failure of the whole TRISO particle layer assembly. Neutron irradiation favors contraction along graphene planes but expansion perpendicular to these planes; so, TRISO particles with higher abundance of anisotropic graphene planes (single preferred orientation) will experience much higher carbon coating shrinkage than TRISO particles with primarily isotropic graphene planes (random orientation) (López-Honorato et al., 2010). TRISO particles with the highest abundance of isotropic graphene

planes will be the most structurally sound. Therefore, it is important to control the coating temperature and coating gas fraction to facilitate the production of isotropic graphene planes in the chemical vapor deposition process. A visualization of the differences between anisotropic and isotropic pyrolytic carbon can be seen in Fig. 12.

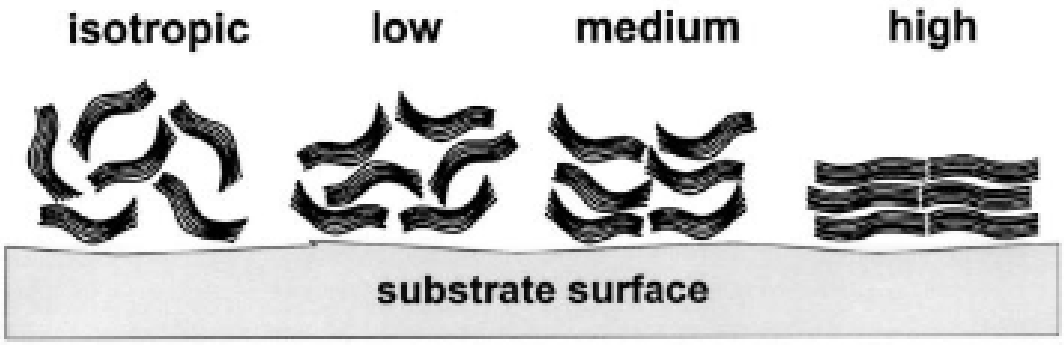

Figure 12. Differences in physical structure between isotropic and anisotropic pyrolytic carbon. Individual illustrations become more anisotropic from left to right (Reznik & Hüttinger, 2002).

The buffer carbon layer is important in the fission product transport properties of TRISO particles. The buffer layer is composed of porous pyrolytic carbon and acts as a void volume to accommodate fission gases, fission recoils, and swelling of the fuel kernel. During irradiation, the porosity of the buffer carbon layer can become altered, and the layer can undergo densification and contraction. This can lead to tangential stresses that cause the buffer to crack. The buffer layer also has the lowest thermal conductivity of all the layers in the TRISO particle, due to its high porosity. Irradiation can cause the buffer's thermal conductivity to change over time and to produce a temperature gradient within the layer that can cause Soret fission product diffusion to occur ("Longer Term Accident Tolerant Fuel Technologies," 2021). Buffer densification can also lead to reduced buffer layer thickness, causing the buffer and IPyC layers to delaminate from each

other and create a gap between the two layers (Bower et al., 2017). Fig. 13 displays both buffer cracking due to kernel swelling and delamination of the buffer and IPyC layers.

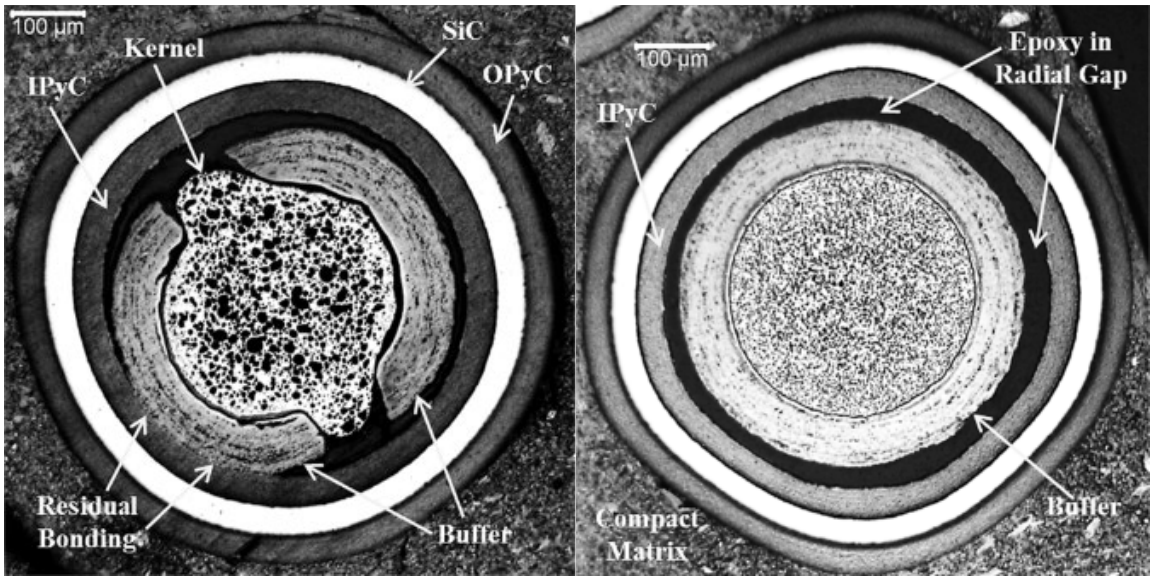

Figure 13. Left, buffer cracking due to kernel swelling. Right, delamination of IPyC and buffer layer. Buffer densification is present in both cases (Bower et al., 2017).

Post-irradiation examination of AGR-1 TRISO particles has uncovered that multiple particles released fission products through degraded SiC layers due to incomplete tearing of the buffer layer. This SiC layer failure appeared to manifest as a two part mechanism. The first step involved exposure of the SiC layer through either the formation of arrowhead cracks passing through the buffer and IPyC layers or fractures in the IPyC layer induced by incomplete buffer tearing. Arrowhead cracks formed when buffer layer material fractured where the buffer and IPyC layers were still attached. Untorn buffer layer material adhering to the IPyC layer during buffer densification was also shown to induce IPyC layer fracturing. The second step involved accumulation of palladium at the IPyC-SiC interface due to the IPyC fractures and subsequent degradation of the SiC layer through the formation of palladium silicides. As the IPyC layer fractures are strongly associated with buffer layer adhesion, low buffer-IPyC interface strength

and therefore full buffer-IPyC delamination/tearing is desirable (Hunn et al., 2014; Mauseth et al., 2023; Paul A. Demkowicz et al., 2015; Stempien et al., 2021).

1.2 Objective

Quantifying the mechanical characteristics of the buffer-IPyC interlayer would inform a better understanding of buffer cracking and buffer-IPyC delamination, resulting in an improved capability to predict the behavior of TRISO particle layers for TRISO particle fuel qualification. To date, statistical failure modeling software such as PARFUME and BISON use numerical integration and Monte Carlo techniques to derive thermal, mechanical, and mass diffusion material properties in simulated TRISO particles. However, while these software packages have proven to be quite accurate at modeling wholistic TRISO particle failure (Jiang et al., 2021, 2022; Skerjanc et al., 2016), there is still a lack of experimental literature on the micro-tensile properties in the buffer-IPyC interlayer region. Using a micro sized (rather than macro sized) tensile gauge section serves two purposes. First, it reduces the radioactivity of the tensile samples to nearly zero, making them safer to handle. Second, the micro-tensile samples are meant to fit within the curvature and size of the targeted layers (~72-100 μm thick) to give an in situ representation of these layers while working within the given geometrical constraints. It should be acknowledged that while the tensile strengths for the selected gauge dimensions may or may not be biased towards certain microstructural features such as porosity, the goal of this dissertation and ongoing work is to assess the change in tensile properties of the chosen TRISO particle regions in unirradiated and irradiated conditions (Mauseth et al., 2023). Through the work done by Mauseth (2021), a capability that enables micrometer scale tensile strength characterization of the buffer, IPyC, and buffer-IPyC interface of TRISO particles was developed. The primary objective of this dissertation work is to determine the micro-tensile properties of the buffer, IPyC, and buffer-IPyC interface regions of

surrogate fueled, unirradiated fueled, and irradiated fueled TRISO particles. It should be noted that the tensile data reported in this dissertation is part of an overall effort working towards establishing micro-tensile testing as a viable technique to measure layer properties of TRISO particles. The sensitivity of the results to tensile gauge length and the impact of gauge width was not studied relative to the porosity distribution and pore size. As such, the accuracy of the data is questionable in that it is not confidently representative of modern TRISO fuel particles (though it may be precise). The relative changes seen in the tensile properties in this study provide context on the variable layer properties but the ultimate magnitude of the measured Weibull parameters, ultimate tensile strength, and ultimate tensile strain may not be representative of real fuel systems. When the micro-tensile testing technique is validated for porous materials and the tensile properties of the buffer-IPyC region are experimentally determined, the knowledge gap in literature can be filled and TRISO failure models for these regions can be verified (Mauseth et al., 2023).

2.0 Literature Review

2.1 Mechanical Testing

2.11 Nanoindentation

Nanoindentation is a useful materials characterizing technique and can be used to study the mechanical properties of TRISO particles. The most common use of nanoindentation is a measurement of properties such as modulus and hardness of materials in different shapes, sizes, and scales. The technique is applicable to a variety of materials differing over a large range of hardness and does not require extensive sample preparation. The two main variables of nanoindentation testing are load and depth. The load is the amount of force exerted on the nanoindentation instrument, while depth is the distance moved by the instrument. Nanoindentation probes come in a variety of shapes, including spherical for stress-strain, Berkovich for elasticity

and height, flat punch for complex modulus, wedge for three-point bending, spherical cone for scratch measurements, and cube corner for fracture toughness. The process of nanoindentation includes multiple steps. The first step involves an actuation process to apply a load. The instrument senses the displacement and then adjusts accordingly. These adjustments are used to calibrate the frame stiffness, which can be used to calculate the elastic, viscoelastic, and soft material properties. This process is also rate dependent, temperature dependent, and plasticity dependent. The depth of penetration during this process helps define the area of the tip in contact during indentation, which determines hardness. When combining the stiffness obtained from displacement adjustments and the hardness obtained from the surface area of the indentation tip, the reduced modulus of the system can be calculated (Nanoscience Instruments, 2021). Fig. 14 illustrates a common load-displacement diagram, the geometry of the indentation procedure, and the equations for hardness (H) and reduced elastic modulus (E_r). Hardness is defined as the maximal indentation load (P_{max}) over the projected contact area at maximal indentation load (A_c). A_c can be deduced by multiplying the contact depth (h_c) by the indenter geometry variable (f), where f is dependent on the indenter type being used. When determining reduced elastic modulus (E_r), stiffness (S) and the indenter geometry constant β also need to be taken into consideration. Stiffness is calculated by taking the derivative of the tangent line to the unloading curve at the point of P_{max} (NanoScan, 2018).

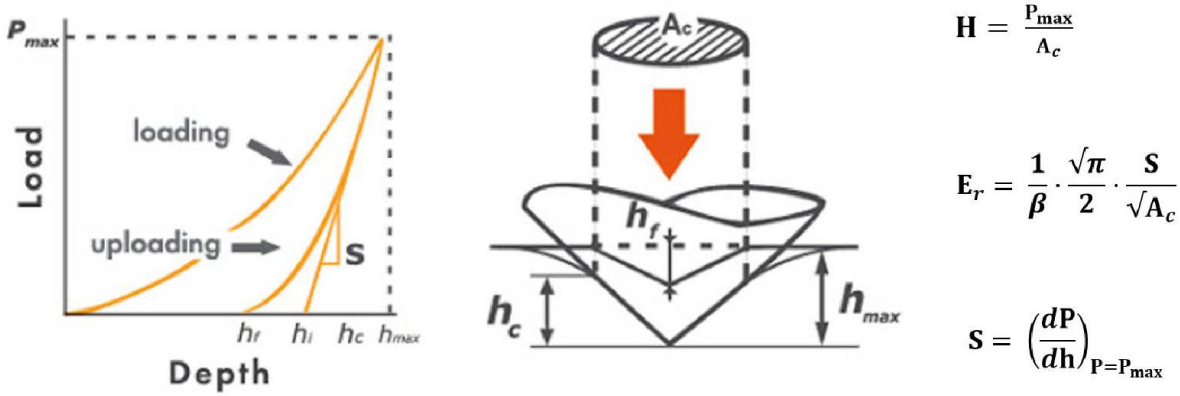

Figure 14. Illustration of the indentation procedure accompanied by the equations for hardness (H) and reduced elastic modulus (E_r) (NanoScan, 2018).

The studies done by López-Honorato et al. (2010), van Rooyen et al. (2011, 2012), Rohbeck & Xiao (2016), and Bellan & Dhers (2004) demonstrate good work in respect to nanoindentation for TRISO particle layers. In the study done by López-Honorato et al. (2010), nanoindentation was used to determine the Young's modulus of the IPyC layer in the given TRISO particle. The measurement proved that the Young's modulus of the IPyC layer decreased after SiC deposition. This observation was in line with other studies, which showed that a similar change occurred after SiC deposition in which the Young's modulus changed from 29 to 18 GPa (López-Honorato et al., 2010). These findings are further complemented by work done by van Rooyen et al. (2011), which found that PBMR coated particles (ZrO_2 kernels) batches G146 and G149 had hardness values of 27.75 ± 7.87 GPa and 27.74 ± 3.31 GPa and elastic modulus values of 14.2 ± 1.89 GPa and 15.5 ± 0.69 GPa in their respective IPyC layers (Van Rooyen I, 2011).

In the study done by van Rooyen et al. (2012), the hardness of the SiC layer in the sample TRISO particle was measured using a CSM Nano-indentation Hardness tester. A load of 100 mN was applied to the polished cross-section pieces of the SiC equator for 15 seconds before unloading. All measurements were conducted on a single particle but at three different locations,

leading to a total of 27 measurements per batch. The measured Nano-Indentation hardness for batches D and E from the experiment are shown in MPa in Fig. 15, with values ranging from around 27 to 35 GPa. This study focused on forming relationships between grain size and hardness, with the hardness values obtained in this study offering valuable information in regards to the performance parameters of TRISO particle layers (I. J. Van Rooyen et al., 2012).

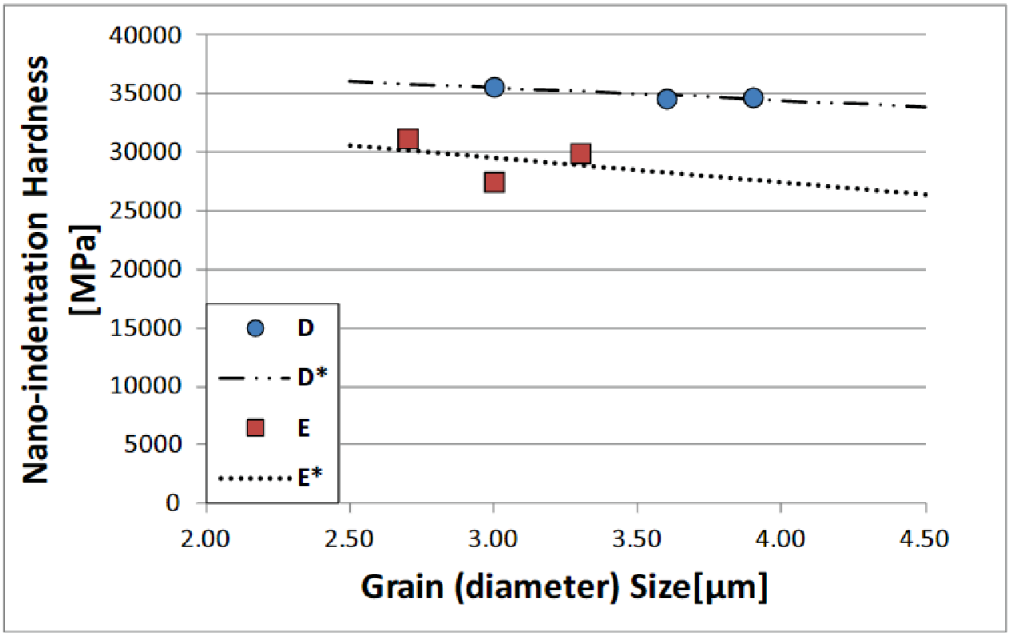

Figure 15. Measured Nano-Indentation hardness of the SiC layer for batches D and E from study done by van Rooyen et al (2012).

In the study done by Rohbeck & Xiao (2016), hardness values were obtained for the SiC layer using a Nano indenter XP (MTS systems) and the elevated temperature measurements were performed using a Micro Materials (UK) system. The maximum load applied to the polished cross section of the TRISO particles was 100 mN for the MTS system or 500 nm for the UK system. The diamond indenter used was of Berkovich shape. The values obtained in this study are comparable to prior nanoindentation studies, and the hardness ranging from 30 to more than 40

GPa (see Fig. 16). With this study providing the hardness values over a large range of temperatures, it provides comprehensive information with regards to the SiC layer in TRISO particles (Rohbeck & Xiao, 2016).

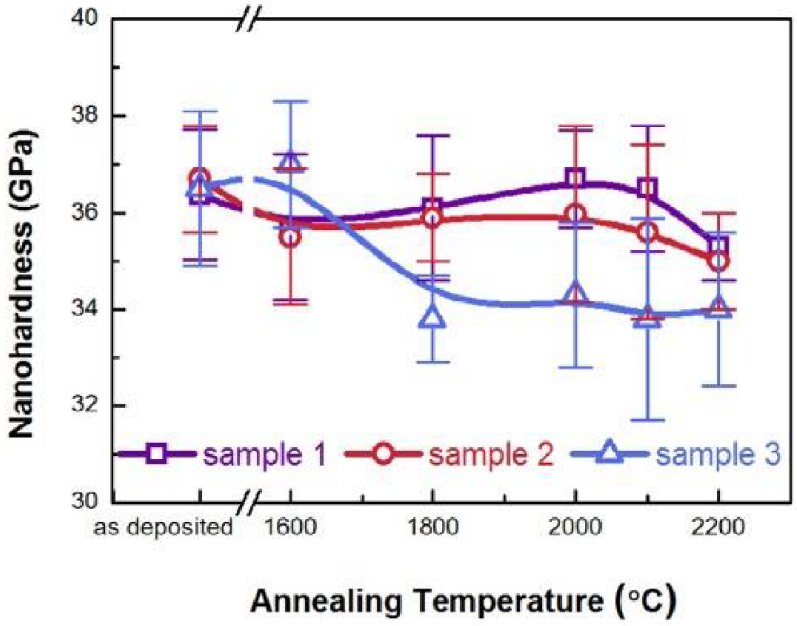

Figure 16. The nano hardness values of the SiC layer at various temperatures (Rohbeck & Xiao, 2016).

The study done by Bellan and Dhers determined the elastic modulus of SiC and PyC deposited by way of fluidized bed chemical vapor deposition (FBCVD) onto flat substrates. Nanoindentation tests done in the study unveiled an average elastic modulus of 25.5±2 GPa for the pyrocarbon substrates. This value was compared to other tests done in the same study by the impulse excitation method, which uncovered a value of between 28.9 and 30.8 GPa for the pyrocarbon substrates. The final conclusion of Bellan and Dhers was that while the nanoindentation technique is highly reproducible and simple to perform, it is not the most accurate method for determining elastic modulus (Bellan & Dhers, 2004).

2.12 Compression/Crush Testing

The studies of many research teams have uncovered valuable information in respect to compression/crush testing for TRISO particle layers. An important study to note is one done by van Rooyen et al., which successfully conducted compression tests on full TRISO particles by crushing them in between anvils of varying materials. While the load required for fracture of the TRISO particles remained nearly the same between hard and soft anvils, the study found that hard anvils cause high local contact bending stresses at the point of contact while soft anvils cause tensile stresses to develop along the latitudinal direction of the TRISO particle. These tensile stresses lead to the development of cracks at right angles to the stress, giving insights into how much internal pressure can be applied for fracture. This led to the conclusion that soft anvils are better for crush testing than hard anvils. The final results of using this crushing technique yielded an average fracture strength of 935 MPa in batch A of the TRISO particles. This value includes all layers of the TRISO particle, including the zirconia kernels, SiC layer, and PyC layers, so a direct comparison to individual layers is not possible (I. van Rooyen, n.d.). An illustration of the crushing apparatus is shown below in Fig. 17.

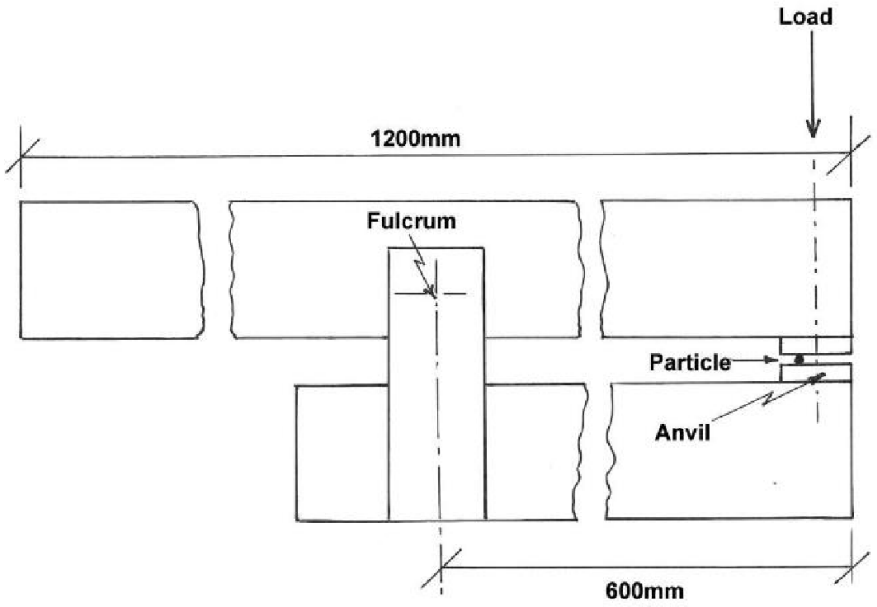

Figure 17. Illustration of crushing apparatus used by van Rooyen et al. (I. van Rooyen, n.d.).

Another style of compression testing, the ring crush test, is similar to micro-cantilever and nanoindentation testing and involves creating a ring shape out of the desired material and pressing until fracture. Fig. 18 illustrates a sample preparation technique developed by Frazer et al. (2017) for creating a ring style TRISO particle specimen for crush testing, while Fig. 19 illustrates how samples of this type are loaded into the crushing anvil (Byun et al., 2008). While this technique has only been used to assess the SiC layer, it still provides valuable insight that can be used for future testing of the PyC layers.

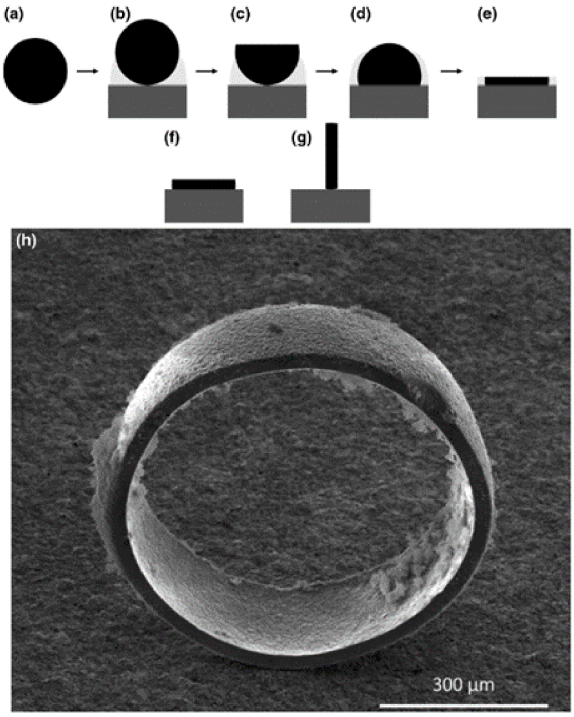

Figure 18. Diagram of ring style TRISO particle sample preparation for ring crush test (Frazer et al., 2017).

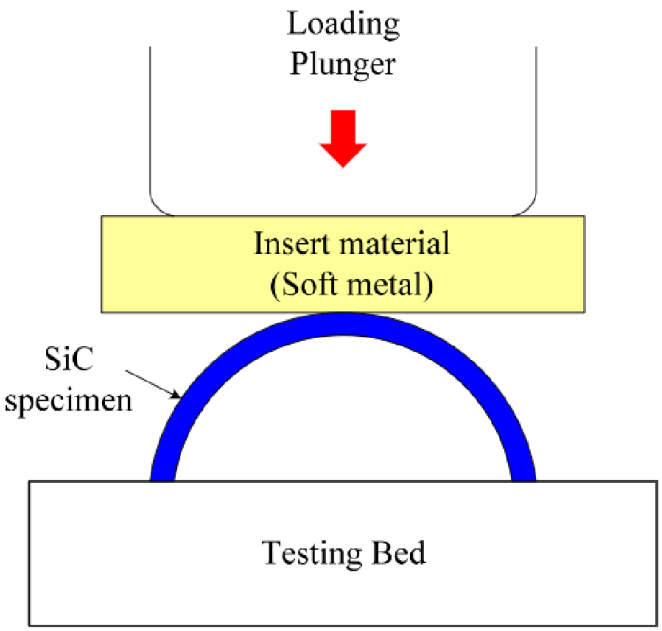

Figure 19. Crushing anvil set-up (Byun et al., 2008).

An interesting study conducted by Wereszczak et al. (2007) served as a hybrid between strict anvil and ring crush tests. In this study, a method was developed to measure the hoop tensile strength of one mm diameter brittle ceramic spheres through the use of 'C-sphere' flexure strength specimens. By applying a monotonically increasing uniaxial compressive force to the C-sphere's outer surface, hoop tensile stresses are produced that ultimately initiate fracture and enable strength quantification and strength limiting flaw identification of the sphere itself. The ultimate goal of the study was to provide relevant design optimization and durability assessments of ceramic fuel particles and breeder/multiplier pebbles for fusion when particle surfaces are subjected to tensile stresses during their manufacturing or service. The study revealed that a relatively large area on the spheres was subjected to high first principle tensile stresses and fracture always occurred in this region. The uncensored characteristic strength was found to be 942 MPa with an effective area of 0.1084 mm^2 and Weibull modulus of 28. Wereszczak et al. determined that at least two surface located flaw types were responsible for fracture initiation at the surface, being micro-structurally small scratches and service located agglomerates containing glassy regions (Wereszczak et al., 2007). Fig. 20 illustrates the shape and dimensions of the carbon spheres.

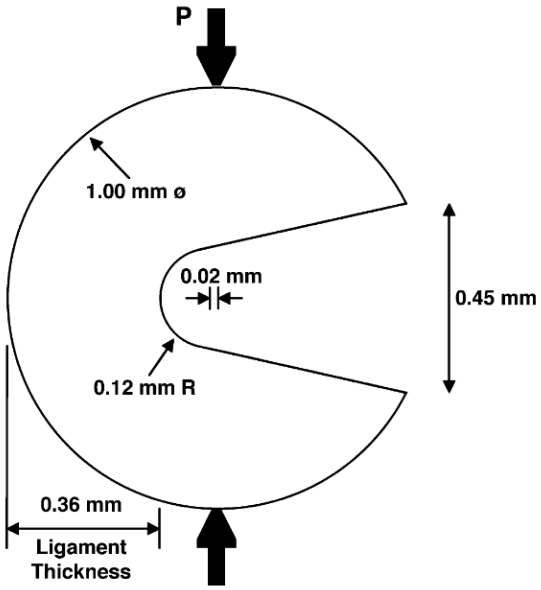

Figure 20. Dimensions of the one mm diameter carbon spheres that were used in the study by Wereszczak et al. (2007).

In the study done by Frazer et al. (2017) nanoindentation measurements are compared to ring crush tests of the SiC layer in TRISO particles. The study found the two technique styles may be correlated to each other, as seen in Fig. 21. The values derived from this study ranged from around 350 GPa to over 500 GPa for the SiC layer, which agrees with other studies of this sort (Frazer et al., 2017).

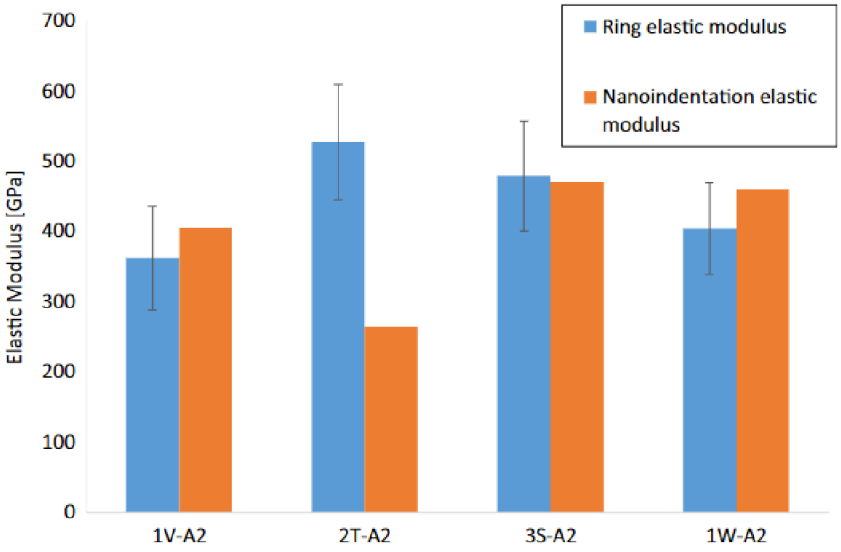

Figure 21. Test results from Frazer et al. (2017) that may lead to a correlation between nanoindentation and ring crush test techniques when applied to the SiC layer of a TRISO particle.

In the study done by Byun et al. (2010), a customized ring crushing technique utilizing a brass blanket foil at load transfer and contact (as seen previously in Fig. 19) was used to identify the fracture stress of a hemispherical SiC shell specimen. This SiC shell specimen was intended to imitate the SiC layer in TRISO particles. Final results indicate that the mean fracture stress varied between 330 and 650 MPa in the test material, as can be seen in Fig. 22 below (Byun et al., 2010).

Table II. Summary of Measured and Calculated Parameters (Data are Mean Values Except for the *m* Values and Scaling Factors for Size Effect)

Material ID	$2r_0$ (mm)	F (N)	m	σ_f^L (MPa)	Scaling factor for Size effect	σ_f^F (MPa)
DUN500S-14B	0.118	2.59	6.61	997.2	2.22	449.8
DUN500S-6B	0.125	3.60	5.49	1050.5	2.57	409.6
DUN500S-7B	0.142	5.32	7.25	1001.5	1.95	514.7
AGR-06	0.147	5.84	6.22	1016.3	2.14	475.4
AGR-10	0.113	4.20	6.40	1232.0	2.16	570.7
LEU01-46T	0.153	11.36	3.98	1203.3	3.02	399.1
LEU01-49T	0.141	8.64	6.35	1324.2	2.05	646.5
B&W-93059	0.151	6.47	6.58	923.1	1.99	463.9
B&W-93060	0.167	6.97	5.15	769.5	2.33	329.9

Figure 22. Table of values linking fracture stress to test specimen as seen in study done by Byun et al. (2010).

In the study done by Rohbeck & Xiao (2016), elastic modulus values for the SiC layer in numerous TRISO particles were obtained by averaging the values of a minimum of 30 samples per batch and temperature conditions in a series of modified crush tests. The elastic modulus found in this study ranged from 200 to 400 GPa, as seen in Fig. 23. With this study providing the elastic modulus values over a large range of temperatures, it provides comprehensive information in regards to the SiC layer in TRISO particles (Rohbeck & Xiao, 2016).

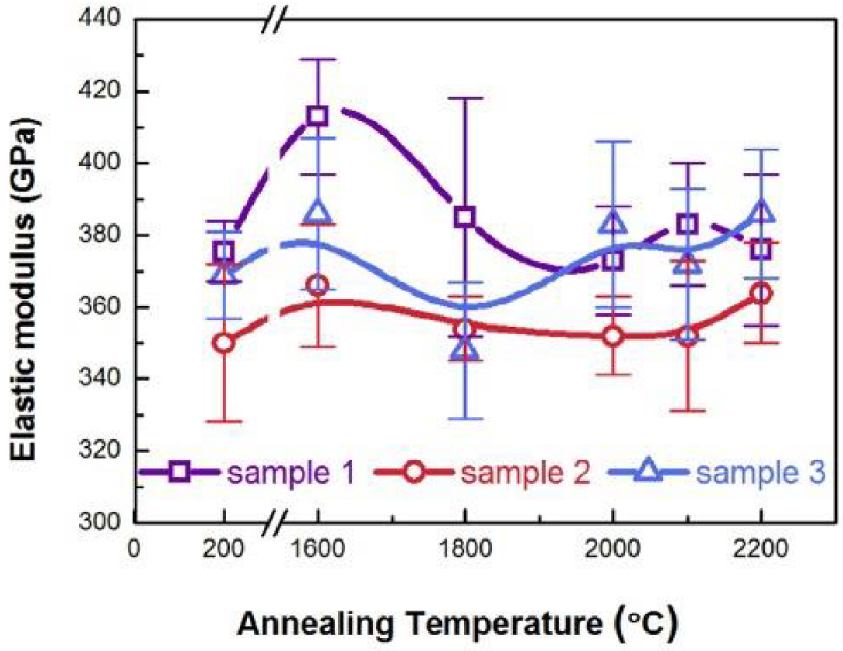

Figure 23. The elastic modulus values of the SiC layer at various temperatures (Rohbeck & Xiao, 2016).

Micro-pillar compression testing is another compression testing technique that has gained popularity in recent years. This technique involves the fabrication of a microscopic column from the desired material and then performing compression tests on the column. This technique primarily reveals the debond sheer strength and internal friction coefficient of the material. A free body diagram showing the stresses involved in micro-pillar compression testing from the work done by Shih et al. (2013) is shown in Fig. 24. The study done by Shih et al. was one of the first studies to use this technique. This study fabricated eight micro-pillar samples from inclined fiber/matrix interfaces that contained a SiC fiber reinforced SiC matrix composite. The SiC fiber was 11 ± 2 μm thick and was coated with five alternating layers consisting of 50-nm of pyrolytic carbon and 1 μm of SiC. These mini composites were then cut with a diamond saw and embedded in epoxy at 45°, 55°, and 60° angles. These pillars were further refined with a low beam current from a FIB to produce 3.5 μm diameter, 15 μm long micro-pillars. These pillars were compressed

with a MTS Nano XP indenter using a flat indenter tip. A diagram of the pillar geometry is shown in Fig. 25. Observing the compression of the micro-pillars showed that debonding occurred at the top fiber/pyrocarbon interface. The debonding shear stress and internal friction coefficient of the SiC fiber/pyrocarbon interface was observed to be 100.3 MPa and 0.73, respectively. This test determined that interfacial properties are important for characterizing the physical properties of fiber composites, which is useful in characterizing the ceramic materials contained within TRISO particle (Shih et al., 2013).

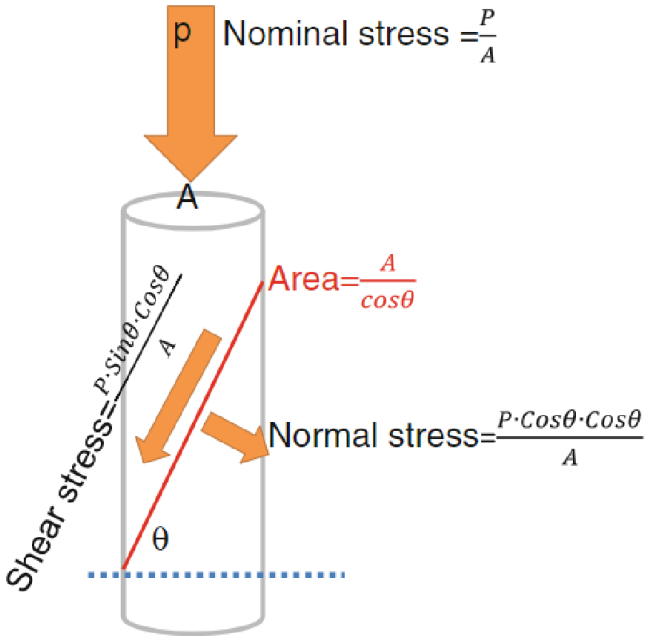

Figure 24. Forces involved in the micro-pillar compression technique (Shih et al., 2013).

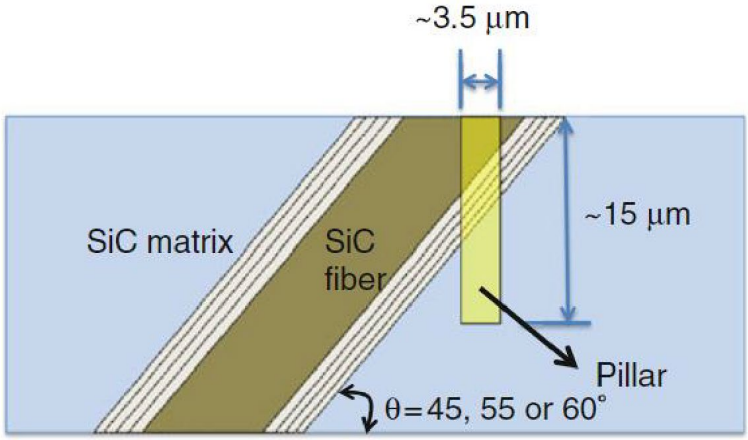

Figure 25. Illustration of final micro-pillar geometry (Shih et al., 2013).

2.13 Tensile Testing

Tensile testing has been extensively demonstrated in materials testing but is a relatively new concept for mechanical testing in TRISO particles. The study done by Gussev et al. (2017) shared many things in common with traditional tensile testing, while including an emphasis on designing a miniature specimen geometry suitable for irradiation in materials test reactors and post-irradiation out-of-hot cell testing. While not initially focused on TRISO fuel specimens, this study demonstrates the utility of tensile testing of nuclear materials on a miniature scale. Dog bones (SSJ and SS-Mini style) consisting of several materials - 304L stainless steel, an aluminum alloy including advanced 3D-printed material, a high nickel 718-alloy, tungsten, and an advanced fuel cladding FeCrAl alloy - were used as the tensile samples. These tensile samples were subjected to mechanical tensile tests inside a High Flux Isotope Reactor (HFIR) rabbit capsule design in order to compare the engineering mechanical properties (yield stress, ultimate tensile stress, uniform and total elongation values, and plastic behavior) between the different SS-J and SS-Mini geometries. This study is significant because it proves that acceptable mechanical property results can be obtained from miniature radioactive materials and can be consistently repeated. The

dimensions of the SS-J specimen geometry and the testing apparatus for the study is shown in Fig. 26 and 27 (Gussev et al., 2017).

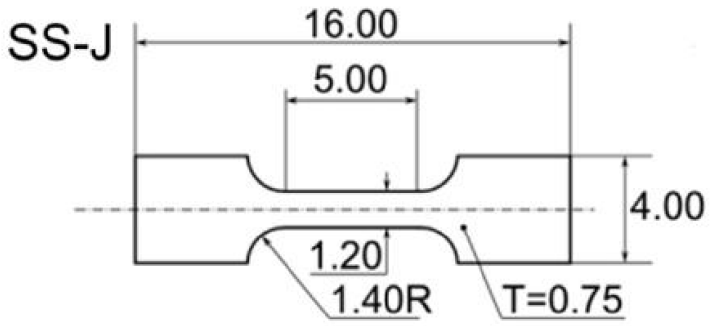

Figure 26. Dimensions of the SS-J specimen geometry, shown in millimeters. This geometry can be comprised of any given material and be subjected to radiation in this experimental design (Gussev et al., 2017).

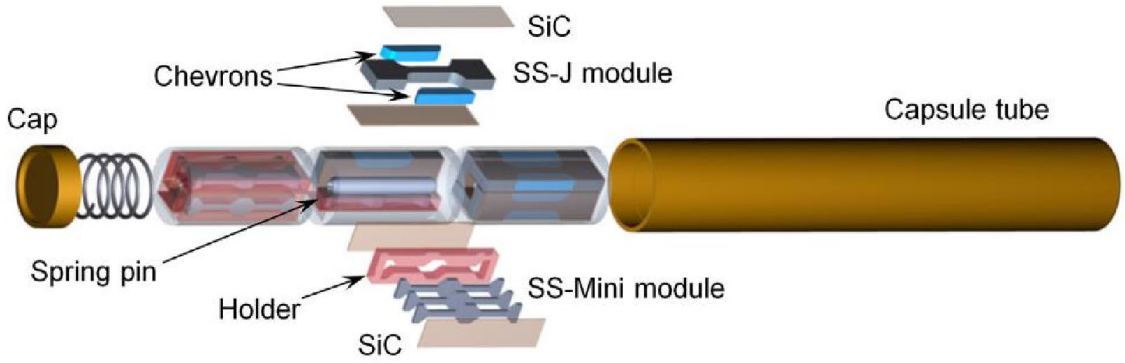

Figure 27. The HFIR rabbit capsule design for SS-J and SS-Mini tensile specimen as seen in the study done by Gussev et al. (2017).

The work shown by Lee et al. (2015) demonstrates a different miniature approach to material tensile testing than Gussev et al. (2017), with the study primarily focusing on the SiC coating layer for the TRISO particle. A novel micro-tensile testing system was developed to evaluate the high temperature fracture strength of these SiC coating layers. Scanning electron microscopy, transmission electron microscopy, x-ray diffractometry, and Raman spectroscopy

techniques were used to characterize these specimens. Fig. 28 demonstrates the sample preparation process, including SiC coating layer deposition, laser etching, and heat treatment to remove samples from bulk material. This study developed a new gripping method for tensile testing of the sample, which involves the specimen being fixed onto small ceramic holders and being held by a ceramic pin, as seen in Fig. 29. In this study, two different types of SiC layers were prepared: SiC-A and SiC-B. The SiC-A specimen had larger grain size (0.4 ~ 0.6 mm) and a round top surface, while the SiC-B specimen had smaller grain size (0.2 ~ 0.3 mm) and a flat top surface. Both coatings decreased in fracture strength when subjected to elevated temperatures. Results of this study indicated that SiC-A was a better candidate for TRISO particle material (Lee et al., 2015).

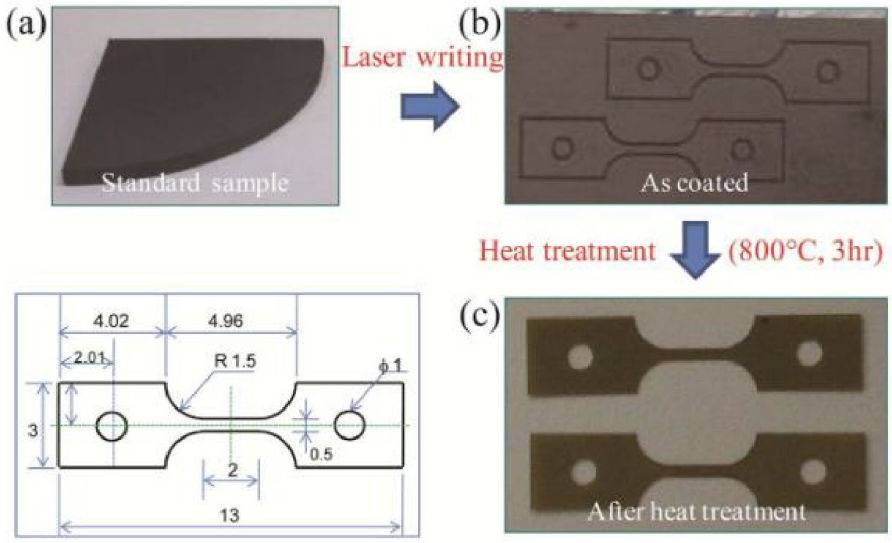

Figure 28. Tensile sample creation display. (a) Is starting sample, (b) is laser etched sample, and (c) is heat-treated sample removed from bulk material (Lee et al., 2015).

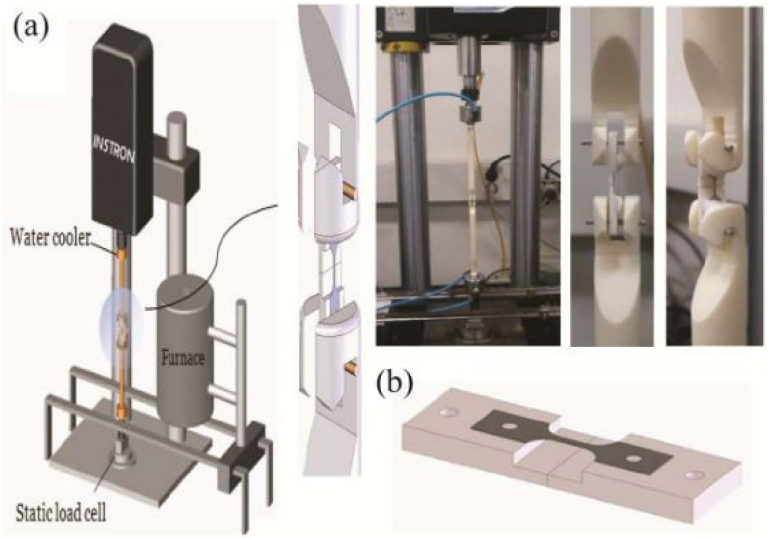

Figure 29. Diagram (a) refers to micro-tensile test set up, while (b) shows sample in place (Lee et al., 2015).

The study done by Bauer et al. (2015) demonstrates a novel tensile testing technique for ceramic materials on a microscopic scale. In this particular study a nanoscale, alumina polymer composite bar is placed in between a hexagonal cellular microarchitecture. Force is applied to the top of the hexagonal cell until the tensile bar is broken, as seen in Fig. 30. The tensile strength obtained from the study was consistent with other literature regarding alumina polymers, marking this technique as a feasible method for measuring microscopic ceramic tensile strengths (Bauer et al., 2015). One of the goals of the research being conducted for this dissertation is to demonstrate the feasibility of testing applications similar to this and to create such geometries in the ceramic TRISO particle layers.

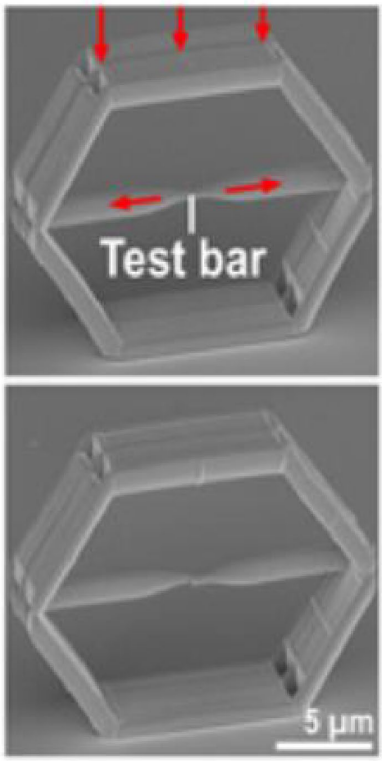

Figure 30. Image of the hexagonal cellular microarchitecture before and after tensile test (Bauer et al., 2015).

Reichardt et al. (2019) performed a unique in situ tensile test on micro-tensile samples of pure Ni single-crystal foils. The dimensions of the dog bones in this study are slightly larger yet comparable to the dimensions to the dog bones fabricated for this dissertation, with the gauge length of the dog bones in the study being 25 to 30 μm and the cross sectional area being approximately 10 μm wide by 13 μm thick. This study used a unique strategy for pulling on tensile samples. A grip in the shape of a rectangular hole was milled into the exposed end of each sample and a hook type gripper made of silicon was placed into the hole, as seen in Fig. 31. The load was applied via pulling on the hole with the gripper. Both unirradiated and irradiated Ni foils were tested. It was determined that there was an increase in fracture stress roughly proportional to the damaging radiation dose, as was predicted (Reichardt et al., 2019). Results of this study

demonstrated that successful tensile testing of irradiated material can be conducted on the micron scale.

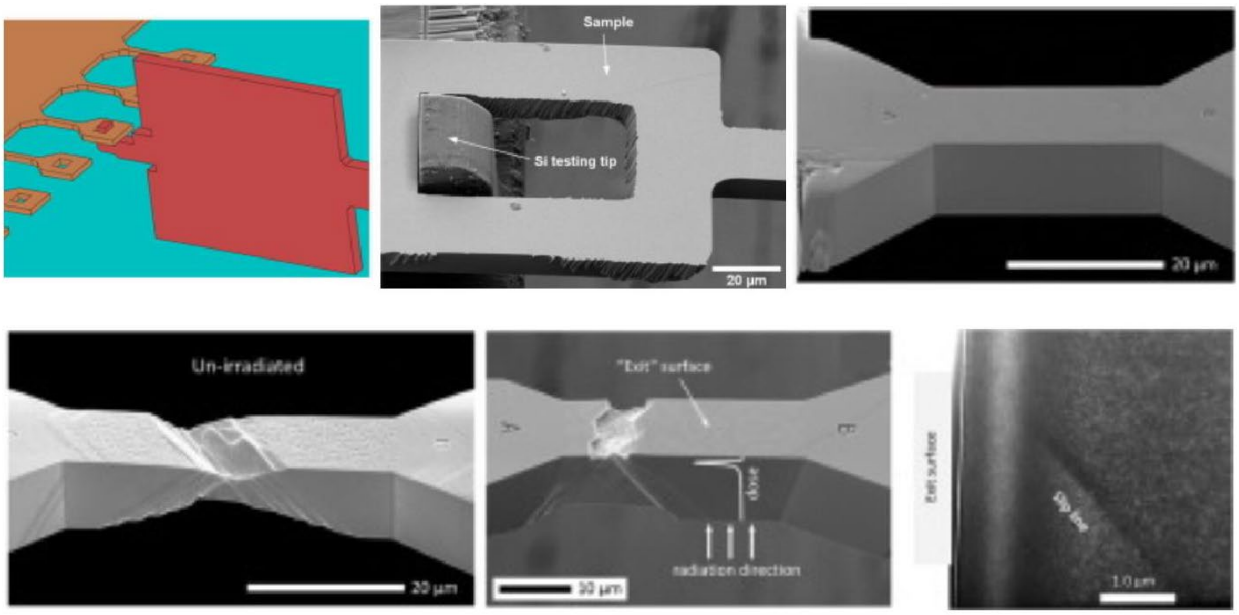

Figure 31. Visuals of the hook gripper set up and various stages of necking of the tensile sample in the study done by Reichardt et al. (2019).

Ando et al. (2018) performed room temperature micro-tensile testing on irradiated and unirradiated F82H steel specimens. The dimensions of the tensile samples in this study are even closer to the dimensions of the tensile samples prepared for this dissertation than in the study done by Reichardt et al. (2019), with the gauge section being around 10-μm long by 1-μm^2 in area. This technique uses a lift-out procedure to remove a lamella from the F82H steel sample and welds it to a SiC micro-beam using tungsten deposition. A dog bone is then milled from the lamella and the tungsten nano-manipulator needle is welded to the top of the dog bone using tungsten deposition, as seen in Fig. 32. The tensile test is performed by pulling upward on the dog bone tensile sample with the tungsten needle. The researchers found that the change in tensile properties due to neutron irradiation is in qualitative agreement with other micrometer-and millimeter-sized

F82H samples. This study demonstrated a unique technique for determining the tensile strength of micron and smaller-sized specimens and could potentially be applied to the layers of TRISO particles and compared to the work done for this dissertation (Ando et al., 2018).

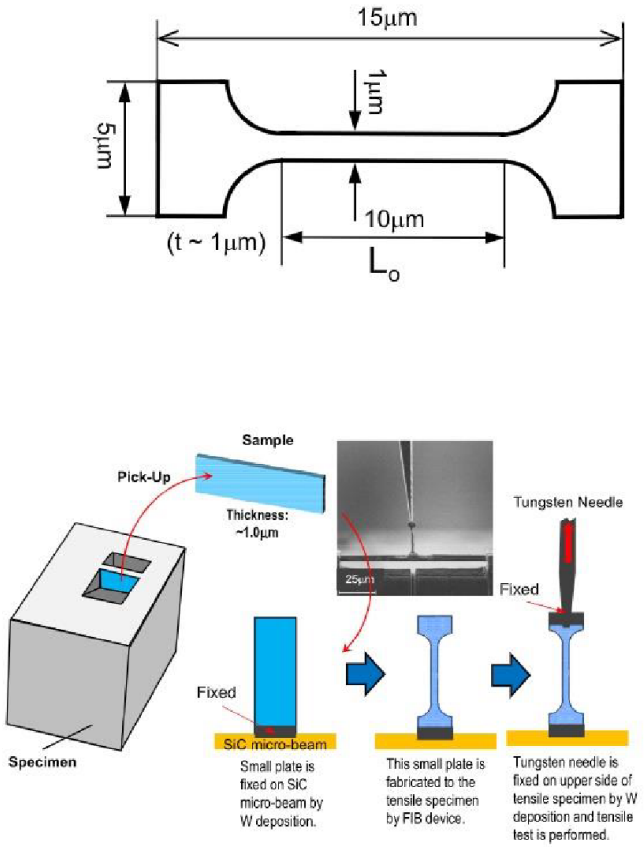

Figure 32. Top diagram shows dimensions of dog bone used for tensile testing. Bottom diagram shows procedure for tensile testing technique (Ando et al., 2018).

Testing performed for this dissertation research was primarily based on work performed by Kiener & Minor (2011). Their work delved into the small-scale plasticity mechanisms that underlie the behavior of nanoscopic materials. To discover these mechanisms, they developed a novel quantitative, in situ nano tensile testing technique that is applied in a TEM setting. The material in question was monocrystalline copper formed into a dog bone shaped tensile sample 100 to 200- nm thick using FIB milling techniques. The copper dog bone was then lined up with

diamond grippers and pulled on until fracture, as illustrated in Fig. 33. The forces involved in fracturing the dog bone determine the tensile strength of the sample (Kiener & Minor, 2011). The technique used for this dissertation work is nearly identical to this process, with the only difference being the scale of the dog bone and diamond gripper. The dog bone and diamond gripper for this dissertation work was on the order of microns, not nanometers.

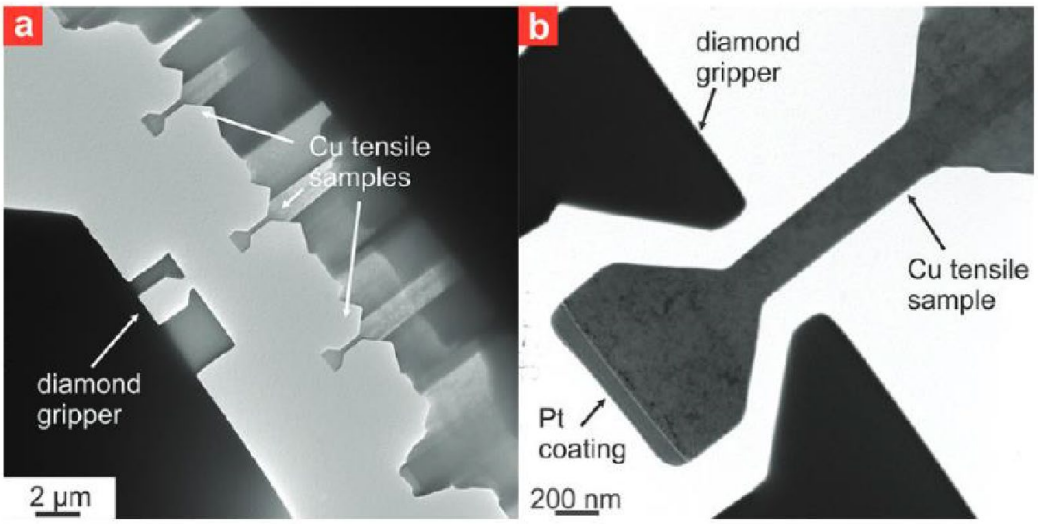

Figure 33. Display of diamond gripper and copper dog bone assembly. (a) Demonstrates a lower magnification image of the copper sample while (b) shows the copper dog bone within the diamond gripper (Kiener & Minor, 2011).

Vo et al. (2017) conducted a study with a testing procedure nearly identical to the one used for this dissertation research, with the only real difference being the materials used for the gripper and the composition of the tensile samples themselves. Vo et al. makes the notable distinction that micro-tensile testing can add tremendous value to materials characterization because it can directly measure the entire stress-strain curve, including the strain to failure. The tensile samples in the study were fabricated from 304 stainless steel specimens in a FEI Quanta 3D FEG dual-beam FIB/SEM and had a final gauge length of around 4.5-μm and a cross-sectional area of around 1.3

x 1.3-μm. Three tensile specimens were created for three different conditions: as-irradiated, post-irradiation annealed (PIA), and unirradiated. The gripper used in this study was fabricated from a tungsten needle mounted on a tip adapter for use in a Hysitron PI-85 PicoIndenter system. The tensile tests were conducted by selecting tension mode in the Hysitron PI-85 software and aligning the dog bone tensile samples with the gripper then pulling on the samples, as seen in Fig. 34. These tests were performed inside the SEM with displacement control and at a rate of 10 nm/s. The study found that the critical resolve shear stress (CRSS) for the unirradiated, irradiated, and PIA samples to be 213 MPa, 438 MPa, and 319 MPa, respectively. These results suggest that micron scale measured strain corresponds well with its macroscopic counterpart, with earlier literature reporting unirradiated macroscopic austenitic stainless steel having a yield strength of around 300 MPa and irradiated specimens having a yield strength of around 1000 MPa (Vo et al., 2017). With the technique used in the study sharing similarities to the technique described herein, we expected great correspondence between the micron scale measured strain and macroscopic measured strain for the TRISO particle layer materials used for this dissertation.

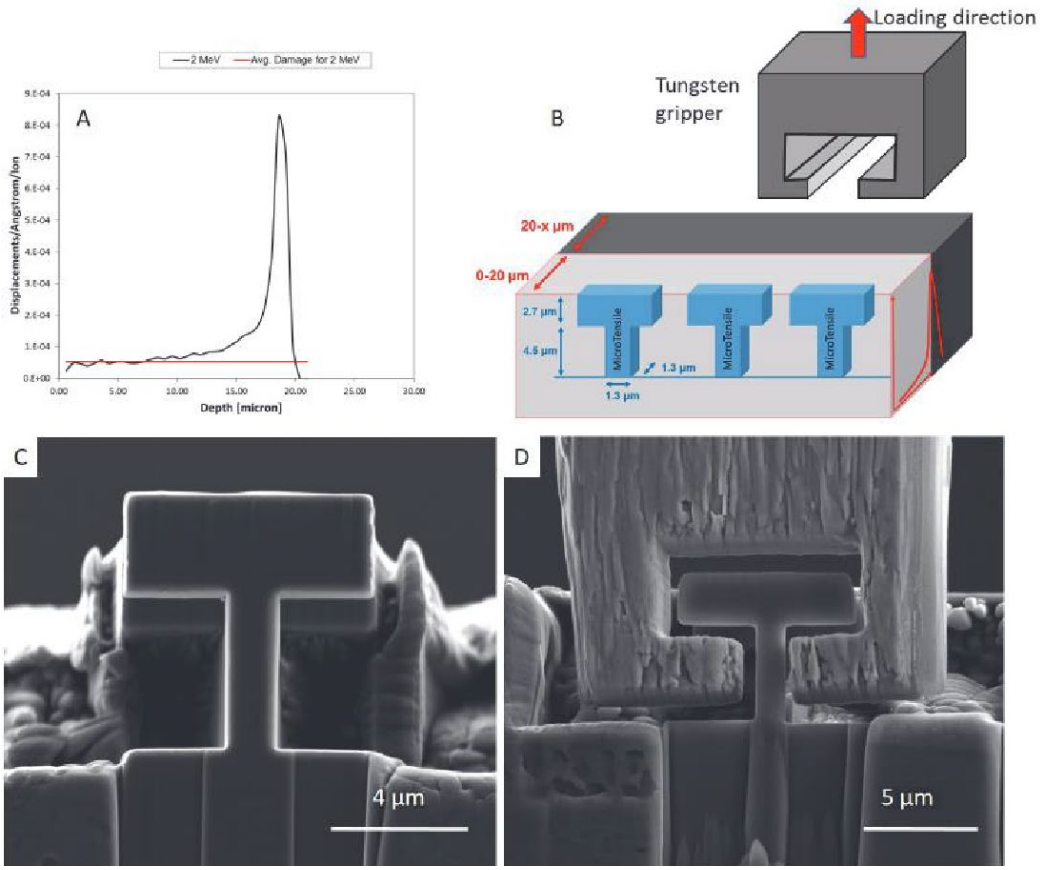

Figure 34. Experimental set up and display of tungsten gripper and steel dog bone. (A) shows a displacement versus depth curve, (B) is an illustration of the tensile testing procedure, (C) is an image of the steel dog bone, and (D) is an image of the tungsten gripper aligned with the steel dog bone (Vo et al., 2017).

As there are no comprehensive experimental tensile results for TRISO particle layers and layer interfaces in literature, mentioning select analytical and modeling approaches for these regions is important. Of particular interest are the studies done by Li et al. (2019) and Wei et al. (2021), both of which solve for the tensile properties of these regions using analytical solution calculations and Monte Carlo approaches. In the study done by Li et al., tangential and radial stresses as well as the failure fraction under normal and extreme conditions for TRISO fuel particles were calculated for the IPyC/SiC/OPyC layers and layer interfaces. Fig. 35 from the study demonstrates their findings that the radial stresses experienced by the IPyC-SiC and SiC-OPyC

interfaces are almost equal in opposition to each other even over a large range of neutron fluences. This ultimately leads to a stable SiC layer that can withstand the extreme conditions experienced inside a nuclear reactor (Li et al., 2019).

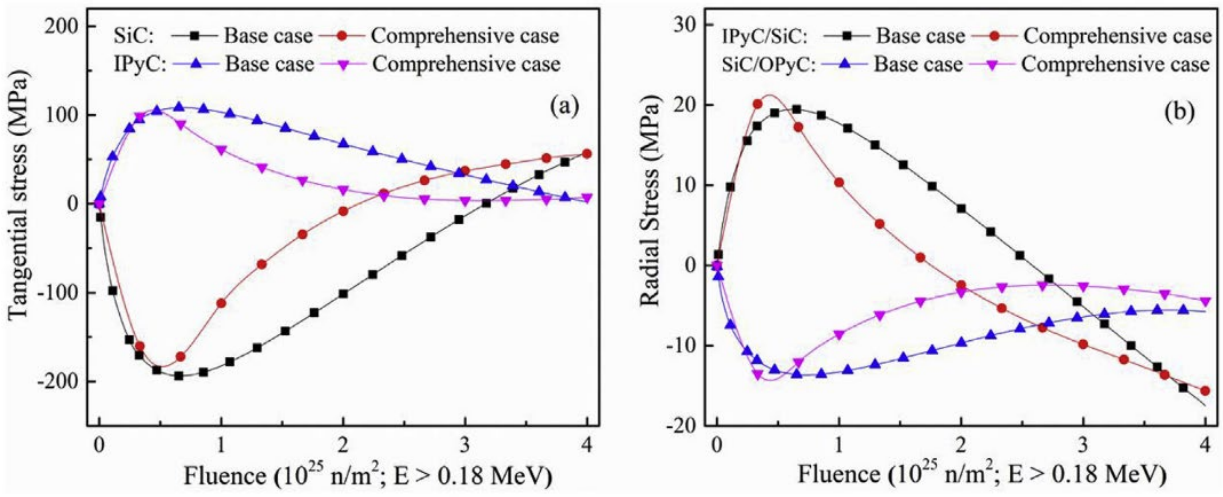

Figure 35. Graphs depicting the relationship between neutron fluence and a) the tangential stress and b) the radial stress in the IPyC-SiC and SiC-OPyC interfaces (Li et al., 2019).

Wei et al. (2021) developed a skeleton stress model for the TRISO particles buffer layer with supporting information for the other layers and layer interfaces. This model was dependent on the current porosity, maximum macroscale tensile stress, and pore pressure values incorporated into the self-developed code of Thermo-mechanical Analysis of Inert Matrix Fuels (TMAIMF). In particular, this model aimed at developing deeper insights into the simulated thermomechanical variables in fully ceramic microencapsulated (FCM) fuel pellets and effects of buffer later porosity on creep coefficients. The main findings by Wei et al. were that macroscale maximum tensile stresses in the particle coating layers of buffer, IPyC and OPyC as well as the SiC matrix exhibit a significant decrease except those in SiC coating layers and that with a rise in the PyC creep coefficient, the maximum tensile stress of buffer layer skeleton and the buffer/IPyC interfacial

tensile stresses will decrease heavily under irradiation conditions, which gives an explanation for the no-cracking phenomenon in irradiated FCM surrogate pellets (Wei et al., 2021). The first principal stresses and interfacial normal stresses calculated for the TRISO particle layers of interests can be seen in Fig. 36 and 37.

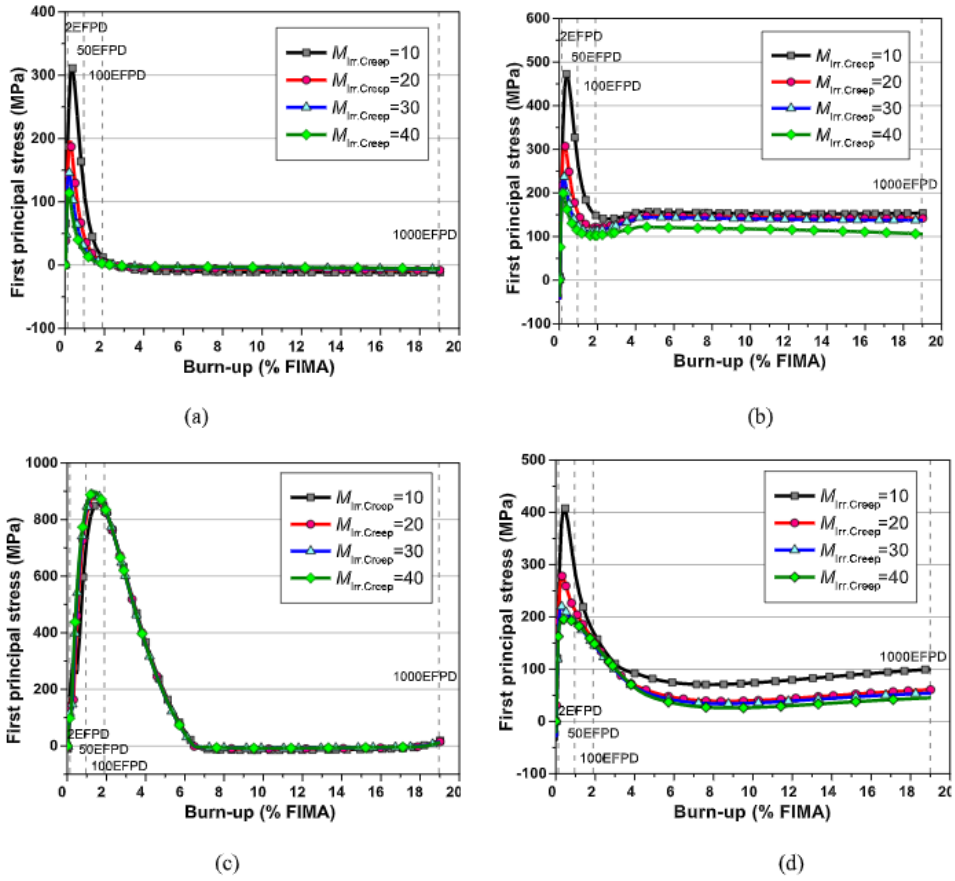

Figure 36. First principal stresses calculated for the a) buffer, b) IPyC, c) SiC, and d) OPyC layers (Wei et al., 2021).

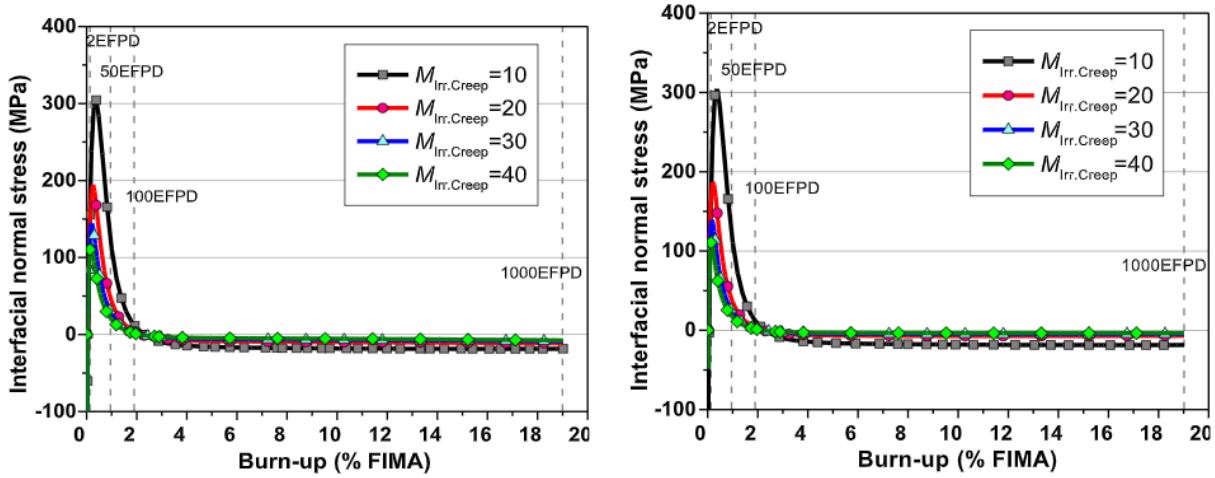

Figure 37. Interfacial normal stresses calculated for the buffer/IPyC interlayer region at a) pellet center and b) pellet periphery (Wei et al., 2021).

2.2 Electron Microscopy Analysis

2.21 TEM Imaging

Transmission electron microscopy (TEM) is by far one of the most commonly used materials characterization techniques, with TRISO particles and their constituent layers being no exception to TEM analysis. While TEM can be utilized in a multitude of ways, it is most commonly known for its ability to produce extremely high resolution images (less than one nanometer depending on experimental parameters) that can be used to distinguish between important micro-structural features. These images come in three main modes: bright field, dark field, and high angle annular darkfield scanning transmission electron microscopy (HAADF-STEM). Bright field mode is the traditional imaging mode where electrons that are transmitted through the sample are used to construct the image. Typically, areas of higher material density/Z number will appear darker whereas areas of lower material density/Z number will appear brighter. Bright field mode is advantageous for its high resolution, mass and crystallinity dependent contrast, and potential for elemental analysis (see EDS section). Dark field mode utilizes the scattered electrons rather than

the transmitted electrons to form the image. Opposite of bright field mode, in dark field mode areas of higher material density/Z number will appear brighter whereas areas of lower material density/Z number will appear darker. Dark field mode is advantageous for its high-resolution, crystallinity dependent contrast, and low noise images. HAADF-STEM is a specialized form of dark field mode that is more sensitive to electrons scattered from high mass/Z number materials. It is particularly useful for detecting high mass/Z number precipitates in low mass/Z number materials, such as fission product precipitates in the pyrocarbon layers of TRISO particles. While HAADF-STEM is useful for detecting these precipitates, this mode is unable to provide crystallinity information (Klein et al., 2015). Illustrations of the workings of the three main TEM imaging modes can be seen in Fig. 38.

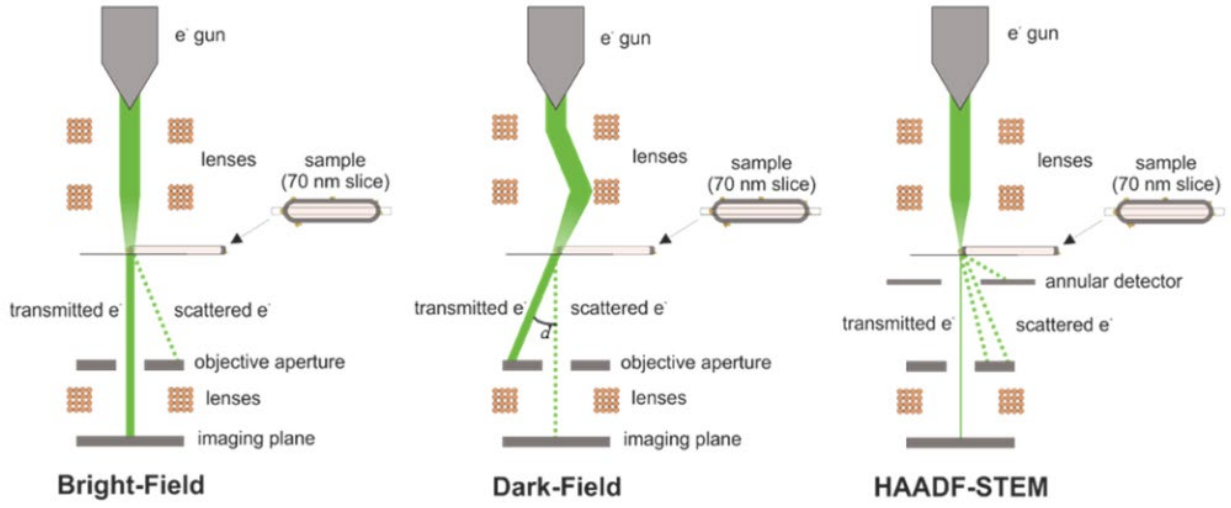

Figure 38. Mechanics of bright field, dark field, and HAADF-STEM imaging modes (Klein et al., 2015).

Multiple studies have revealed that silver and palladium can deposit deep in the IPyC layer and migrate into the SiC layer in TRISO particles. Using the three main TEM imaging modes and other techniques, van Rooyen et al. was able to identify large deposits of palladium and silver on

the IPyC-SiC interface, as seen in images a) and b) of Fig. 39. Silver was also found in triple junctions in the IPyC layer (van Rooyen et al., 2012; van Rooyen, Lillo, et al., 2014; van Rooyen, Nabielek, et al., 2014). The placement of the silver and palladium deposits confirms that the IPyC layer primarily serves as a structural component in the TRISO particle and does little to stop fission product migration. The fission products are stopped by the SiC layer and come to rest at the IPyC-SiC interface.

Wen et al. demonstrated that the precipitates found within the IPyC layer were significantly smaller than precipitates close to the IPyC-SiC interface, with the largest precipitates being found beyond the interface in the SiC layer (Wen et al., 2015). The small precipitates found in the IPyC layer can be seen in image c) of Fig. 39. The precipitates do not pool within the IPyC layer and therefore remain small as they pass through the IPyC layer. They gain size once they accumulate at the IPyC-SiC interface.

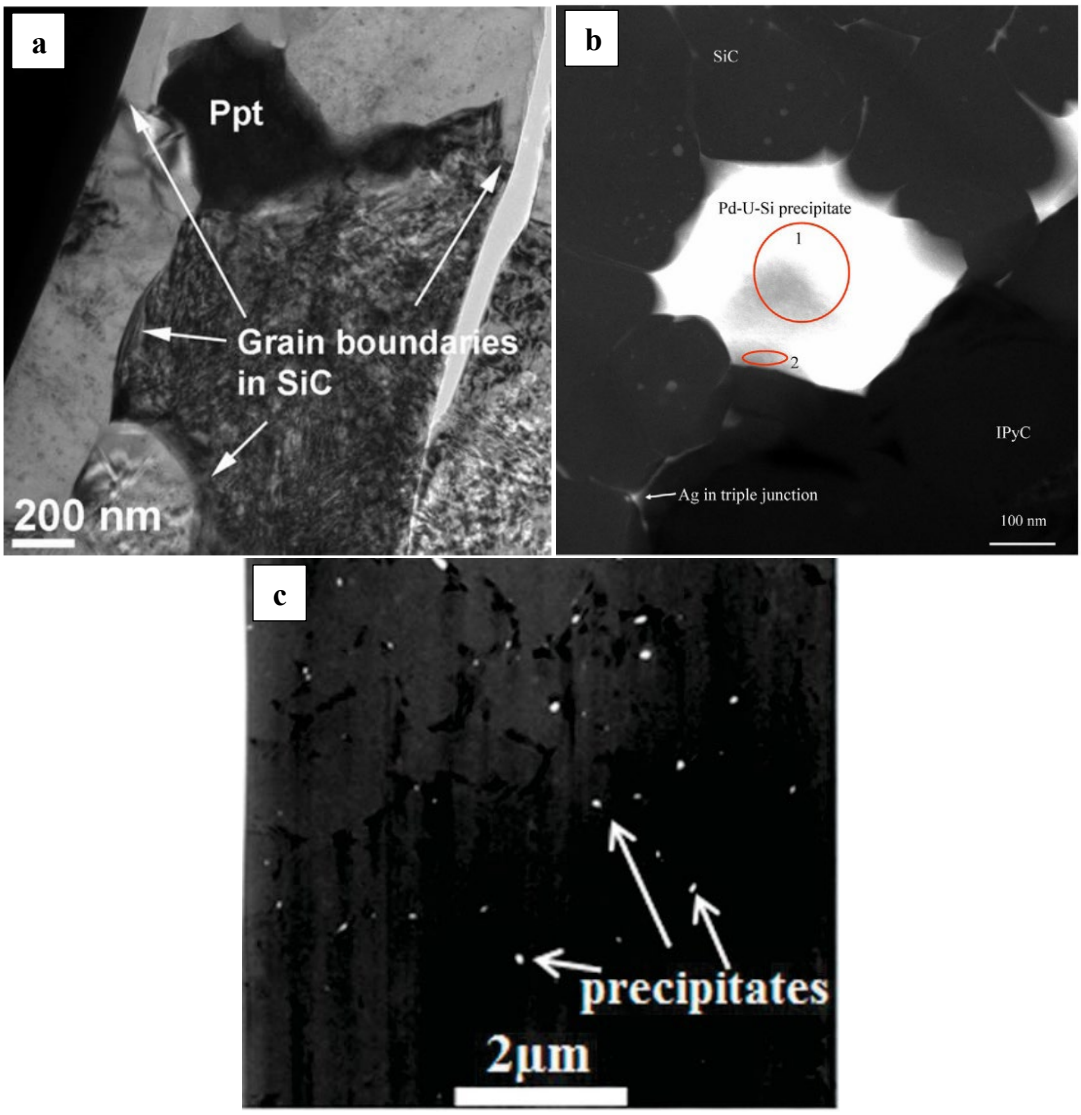

Figure 39. TEM images of fission products found within TRISO particles where a) shows a bright field image of precipitates found on the IPyC-SiC interface, b) a HAADF-STEM image of palladium deposits on the IPyC-SiC interlayer and silver deposits in IPyC triple junctions, and c) a dark field image of relatively small precipitates found in the IPyC layer (van Rooyen et al., 2012; van Rooyen, Lillo, et al., 2014; van Rooyen, Nabielek, et al., 2014; Wen et al., 2015).

Electron microscopy imaging (in the form of both TEM and scanning electron microscopy (SEM)) is also very powerful in identifying microstructural heterogeneity such as porosity. Detailed characterization of the porous microstructure of the buffer layer (such as analysis of the pore size, distribution, shape, and orientation) provides insight into the process-structure-property-performance relationship of TRISO fuel. In a study performed by Griesbach et al., FIB-SEM

tomography was conducted across a TRISO particles full buffer layer thickness (around 100 μm) to produce 3D reconstructions of the buffer microstructure with 50 nm spatial resolution. An average overall porosity of around 14% was found, with the local porosity and its fluctuation increasing from the kernel interface towards the IPyC layer. Additionally, it was found the largest pores drive the increase in porosity and fluctuation and consist of sprawling networks of connected voids. Most of the pores also have shapes that are moderately elongated and not flat, being preferential towards a circumferential directions. It is believed this directionality may also be due to processing conditions and could play a role in fracture initiation and propagation (Griesbach et al., 2023). A detailed schematic illustrating the porosity distribution found in this study can be seen in Fig. 40.

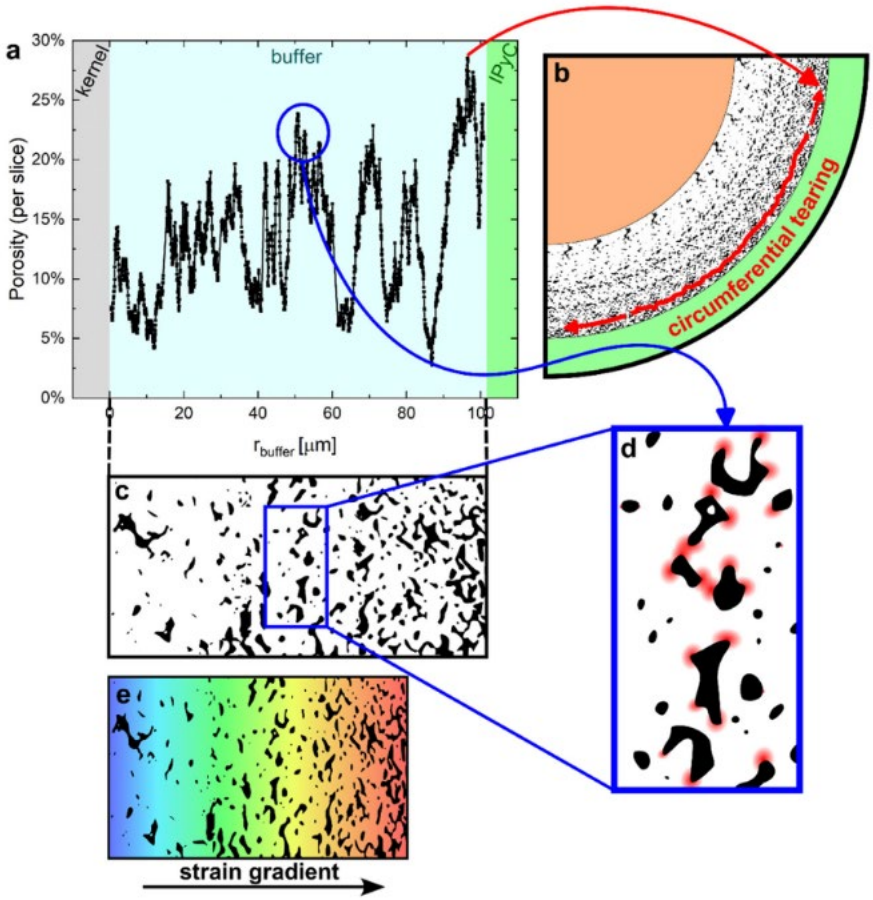

Figure 40. Illustration displaying the porosity distribution of the TRISO particles buffer layer (Griesbach et al., 2023).

2.22 TEM Diffraction

One of the main capabilities of the TEM's is its ability to obtain diffraction patterns, which can be analyzed to give information about the structure of the specimen. Diffraction patterns are obtained when the TEM's objective lens takes electrons emerging from the specimen and produces a magnified image where all the electrons emerging from a single point of the specimen are focused onto a single point of the image, regardless of the angle at which they emerge. As the electrons are conveyed from the specimen to the image, there is a plane, called the back focal plane or diffraction plane, at which all electrons emerging at a single angle are focused onto a single point, regardless of the point on the specimen from which they emerge. When lenses further down in the column

magnify the back focal plane a diffraction pattern can be formed. The diffraction pattern varies from material to material based on the materials microstructure, with the most visible differences being between crystalline, polycrystalline, and amorphous materials. While crystalline materials produce ordered grid-like or "spot" patterns, polycrystalline and amorphous materials produce ring and halo patterns, respectively. The distance, size, and orientation of the spots, rings, and halos found in diffraction patterns can be used to determine the inner atomic spacing and orientation/crystal structure of the material (Tivol, 2010). Illustrations demonstrating the relationship between different diffraction techniques and orientation of the back focal plane can be seen in Fig. 41.

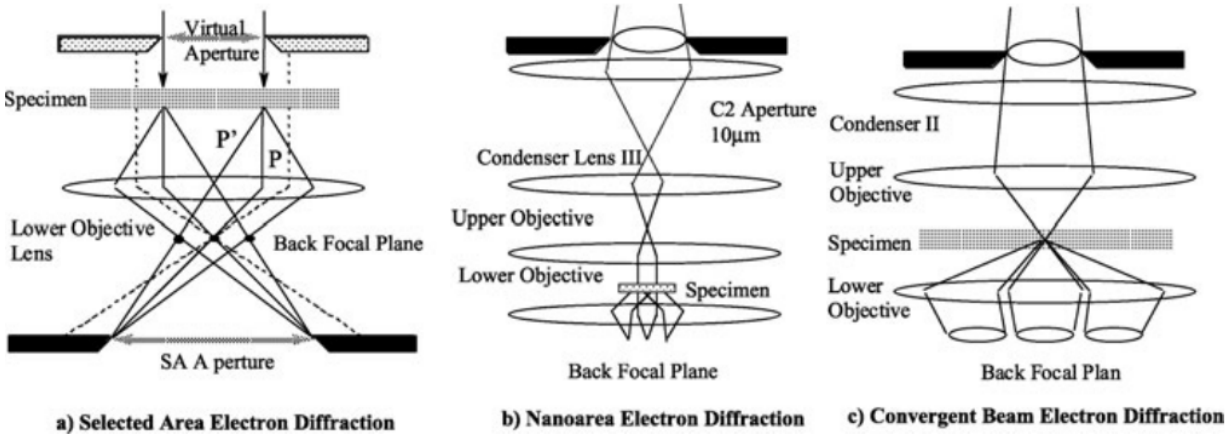

Figure 41. Relationship between the back focal plane and varying diffraction techniques (Zuo, 2006).

During Dr. van Rooyen's dissertation, multiple PBMR TRISO particle batches were manufactured and annealed under varying conditions. Of the many characterization techniques applied to these batches, selected area diffraction (SAD) was one of the most utilized techniques. SAD analysis of one of the batches in particular (unannealed batch G118) can be seen in Fig. 42. SAD analysis of the SiC and IPyC regions of this reference batch revealed a diffraction pattern

consistent with the 3C-SiC phase and a diffraction ring pattern consistent with IPyC materials. When batch G118 was annealed for five hours at 1000° C SAD analysis revealed no significant differences in either the SiC or IPyC layers when compared to the unannealed reference sample. When batch G118 was annealed for one hour and five hours at 1980° C SAD analysis revealed no significant differences in the SiC layer when compared to the unannealed reference sample. However, the IPyC layer demonstrated increasing contrast in its ring patterns, which was an indication of the onset of ordering of the PyC structure, which in turn indicated that the PyC was becoming anisotropic. Being able to detect and decipher these microstructural changes (such as anisotropy) during different fabrication conditions is paramount in assuring quality control of the fabrication process of TRISO particles. Microstructural changes such as anisotropy can significantly impact the performance of TRISO particle fuel under high temperatures and intense neutron fluences (Van Rooyen I, 2011).

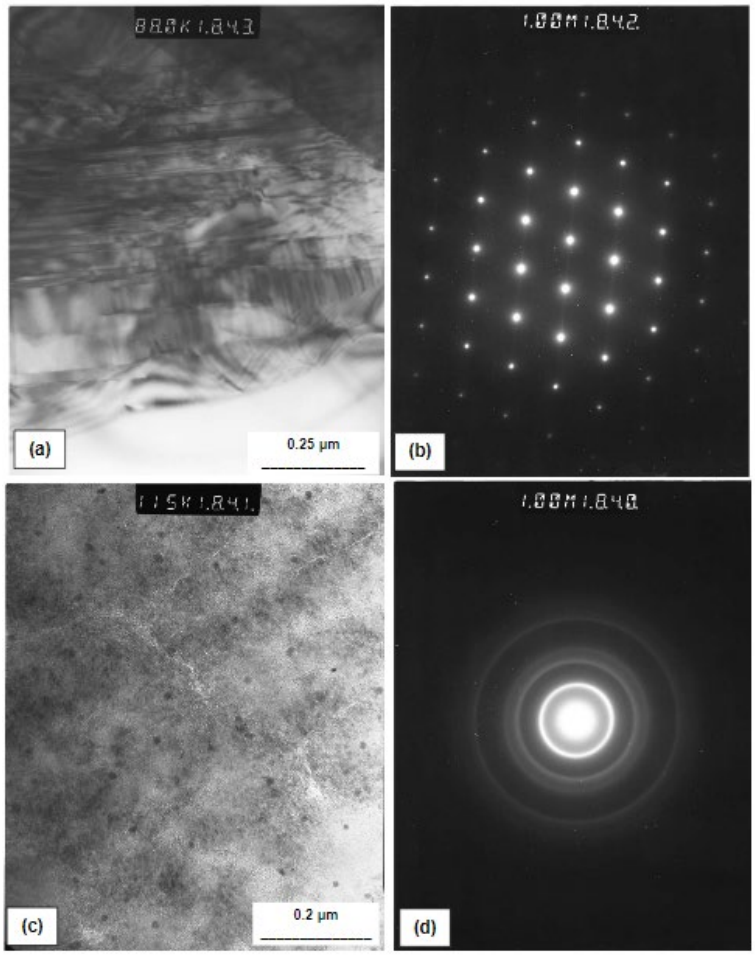

Figure 42. Images of unannealed batch G118's a) unirradiated 3C-SiC layer in bright field mode with b) accompanying diffraction pattern and c) unirradiated IPyC layer in bright field mode with d) accompanying diffraction pattern (Van Rooyen I, 2011).

Diffraction is particularly useful when materials become irradiated. During the study by I. J. van Rooyen, Miller, et al., multiple TRISO particle samples from Compact 6-3-2 were irradiated under varying neutron fluences. When comparing SAD images between unirradiated (van Rooyen I, 2011) and irradiated (I. J. van Rooyen, Miller, et al.) samples, striking changes in the microstructure may become evident. For the SiC layer from CP30, three SAD patterns were analyzed with two of the SAD patterns indicating a cubic SiC phase (3C-SiC, unchanged from unirradiated structure) while one of the SAD patterns indicated a potential hexagonal phase SiC phase (6H-SiC, different from unirradiated structure). For the IPyC layer from CP35, the SAD

pattern analysis revealed that the intensity variations in the diffraction ring pattern for CP35 were more prominent when compared to those of the irradiated IPyC from CP34 and the unirradiated IPyC from the AGR-1 experiment. This implies that irradiation may have increased the anisotropy in the IPyC layer of this sample (van Rooyen et al., 2012). SAD patterns of these irradiated compacts can be seen in Fig. 43.

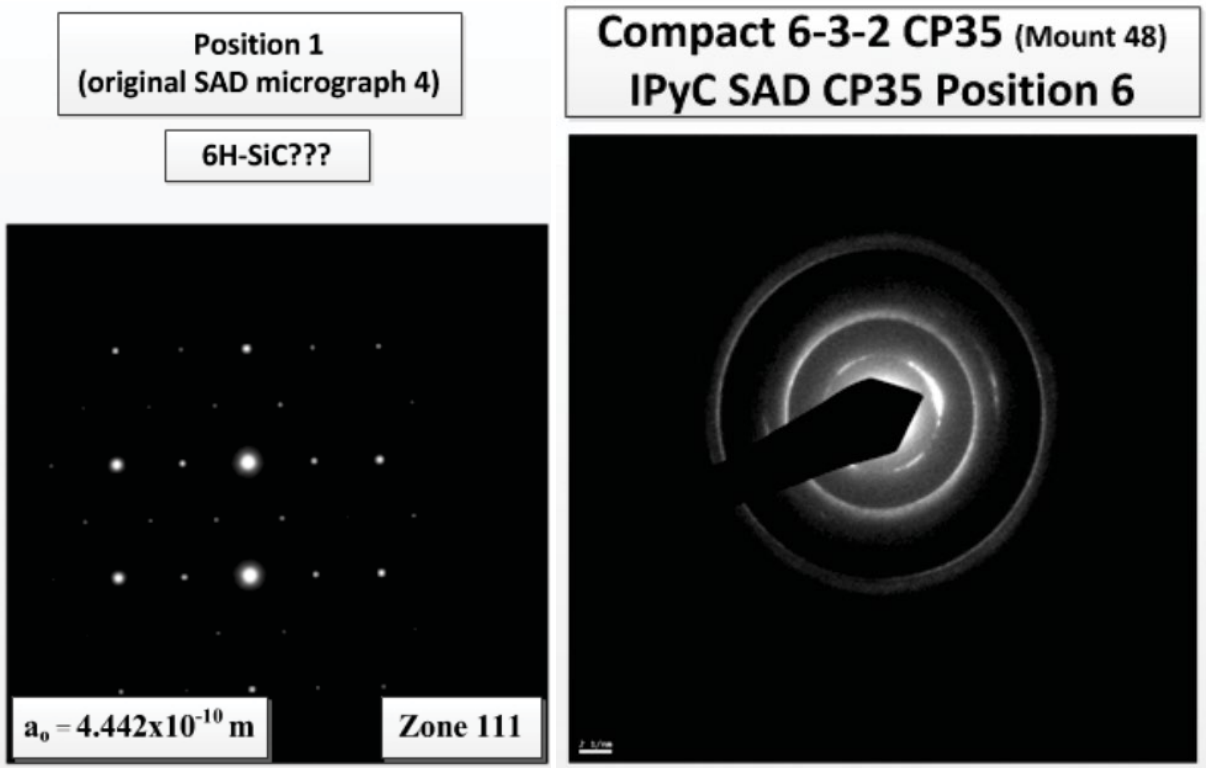

Figure 43. Images of irradiated SiC from Compact 6-3-2 CP30 (left) and irradiated IPyC from Compact 6-3-2 CP35 (right) (van Rooyen et al., 2012).

2.23 EELS and EDS

Electron energy loss spectroscopy (EELS) and energy dispersive spectroscopy (EDS) are both incredibly powerful electron microscopy techniques that can be used to determine the compositional details of a material. EELS is used in the TEM and works by measuring the energy lost by the transmitted electrons due to inelastic scattering events in the sample material. EELS

utilizes the same electrons as the TEM's bright field mode, but rather than forming an image an electron energy spectrum is created instead. EELS has been demonstrated to have a wide variety of analytical applications, such as the determination of dielectric constants, composition, band structure, and chemistry. When EELS is paired with Z contrast imaging techniques (such as HAADF-STEM), detailed information on the composition, chemistry, and structure of materials can be attained with atomic resolution and sensitivity. Additionally, when EELS is applied under multiple scattering analysis, the reference structure can be modified to reproduce the experimental spectrum, leading to a three-dimensional structural determination that is sensitive to single atom vacancies and impurities (Browning et al., 1997). EDS can be used in either the TEM or SEM and is sometimes referred to as energy dispersive X-ray spectroscopy (EDX) due to it being defined as a characteristic X-ray detection method. Characteristic X-rays are formed when outer shell electrons fill a vacancy in the inner shell of an atom, releasing X-rays and in pattern that is characteristic to that element. In the case of EDS, the inner electron shell vacancies are produced through collisions with the primary electron beam from either the TEM or SEM. The energy of the emitted X-rays are then detected and used to create a spectrum that can be used for compositional analysis. Advantages of EDS involve quick elemental analysis, elemental coverage for all but the lightest elements, quantitative elemental data, and large spatial ranges. Disadvantages of EDS include unreliable nitrogen detection for most detectors, only surface level detection, is relatively insensitive with lower detection limits in the percentage range, and only elemental data can be generated (Wolfgong, 2016). The electron-beam mechanics of both EELS and EDS can be seen in Fig. 44.

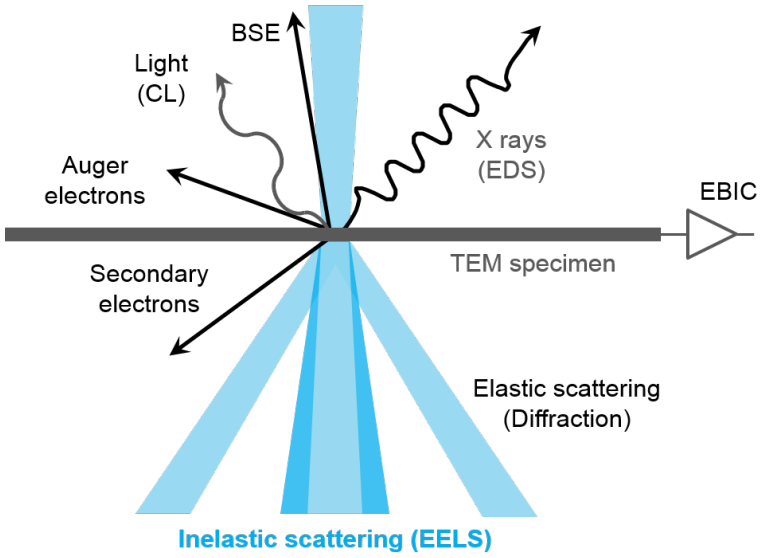

Figure 44. EELS and EDS electron beam mechanics (EELS | Gatan, Inc., n.d.).

According to van Rooyen et al., EELS analysis is important for TRISO research because of the specific resolution of elements of interest. In EELS analysis, chemical sensitivity and size of resolvable features of under 1% and smaller than 1 nano meter can be achieved, respectively. In particular, palladium, silver, and uranium have close but separable edge energies in the EELS spectrum, which suggest that trace amounts of silver should be detectable using EELS techniques. Using the EELS technique, van Rooyen et al. was able to identify the presence of silver in the triple junction of SiC grain boundaries from sample AGR1-632-035 position 6b, as seen in Fig. 45 (van Rooyen et al., 2016).

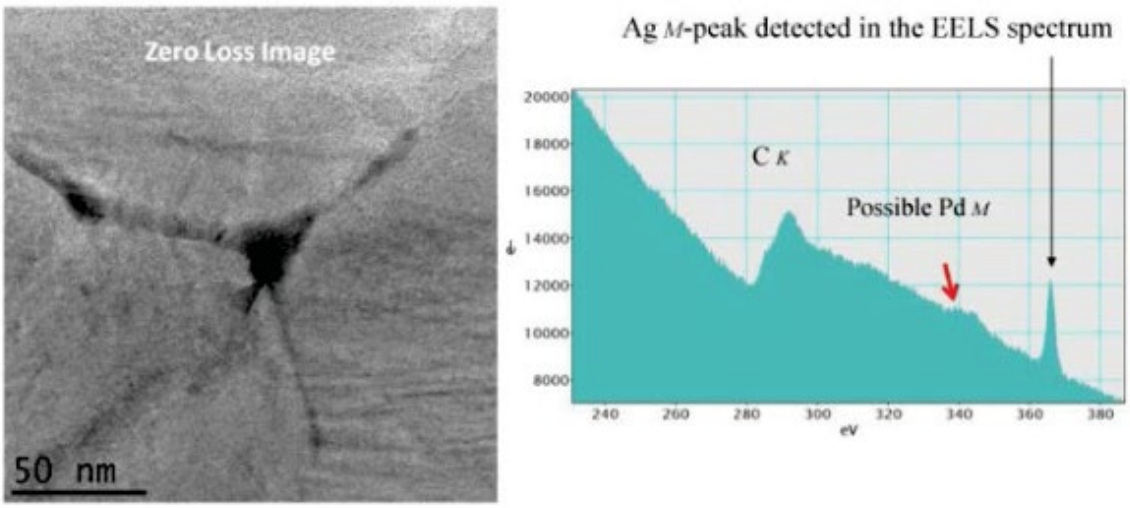

Figure 45. Identification of silver in the triple junction of SiC grain boundaries using EELS (van Rooyen et al., 2016).

In a study done by Leng et al., micron size precipitates with irregular shapes were located along a TRISO particles IPyC-SiC interlayer and were subsequently analyzed using EDS. It was also observed that some of these precipitates were found inside the individual SiC and IPyC layers. The size of these precipitates varied from approximately 100 nano meters up to 2 microns, and the precipitates in the SiC and IPyC layers were smaller than those found in the IPyC-SiC interface. Furthermore, micron sized precipitates in the SiC layer and the IPyC-SiC interlayer had sharp protrusions connecting them to SiC grain boundaries which indicated that their formation may have been associated with the grain boundary transport of fission products. After EDS analysis, it was confirmed that these precipitates were composed mainly of palladium and uranium with trace amounts of other minor fission products such as cesium, europium, and cerium (Leng et al., 2016). An image of the IPyC-SiC interlayer of interest with associated EDS scan can be seen in Fig. 46.

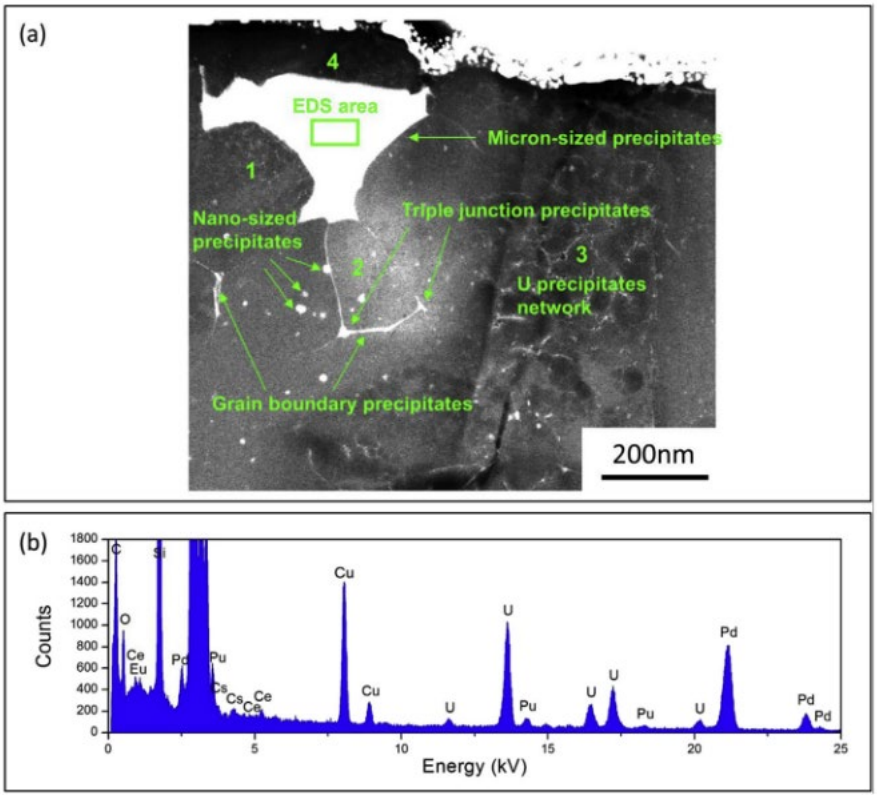

Figure 46. Precipitates found in the IPyC-SiC interlayer (a) with associated EDS scan (b) (Leng et al., 2016).

An important note to mention is that since the SiC layer is meant to be the main fission product barrier, it is expected that most of the fission product deposition will occur in or near this layer. Gerczak et al. conducted a study that found that while U-Pd was a precipitate at the IPyC-SiC interface, other precipitates such as U-Zr migrated to this boundary (see Fig. 47). Additional precipitates such as plutonium and rhodium were also found at the interface (Gerczak et al., 2020).

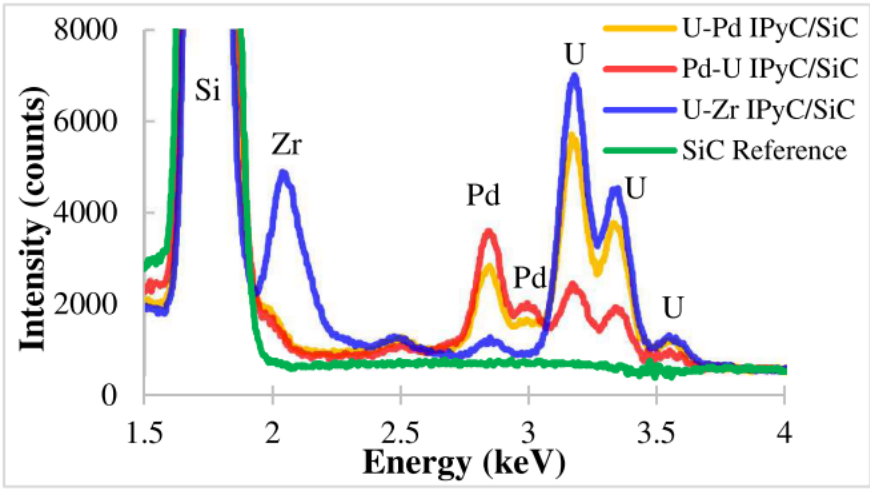

Figure 47. EDS spectra showcasing multiple precipitates at the IPyC-SiC interface (Gerczak et al., 2020).

2.24 EPMA

Electron probe microanalysis (EPMA) involves bombarding a specimen with a focused electron-beam and analyzing the emitted X-rays (typically utilizing both EDS and wavelength dispersive spectroscopy (WDS) analytical techniques) in an instrument known as a microprobe. WDS is very similar to EDS in that it analyzes characteristic X-rays but differs in that it separates emitted X-rays according to their wavelength rather than separating them according to their energies. WDS exhibits far greater spectral resolution than EDS but has a much slower data collection rate. However, when WDS is combined with EDS in EPMA the two techniques complement each other and produce a powerful analytical instrument. EPMA has the ability to identify and analyze all the elements of the periodic table in any solid material except for hydrogen and helium. Since the emission of X-rays is largely restricted to the area of the material exposed to the electron-beam, EPMA can produce quantitative data in highly localized regions of under one micron in diameter. Additionally, EPMA is nondestructive and multiple measurements can be repeated as often as required in the same location. EPMA is commonly used to measure elements at trace levels of 100 parts per million (ppm) and, with optimized settings, can even measure

elements at concentrations down to 10 ppm. In contrast to single EDS instruments typically found on TEM's and SEM's, EPMA's typically possess up to five WDS instruments, each being fitted with different diffraction crystals to reflect specific wavelengths. By pairing multiple WDS instruments together, analysis of spectra with higher spectral resolutions (5–10 eV) than EDS (120-130 eV) is possible (Essential Knowledge Briefings Electron Probe Microanalysis, 2015). An illustration of an EPMA instrument with WDS attached can be seen in Fig. 48.

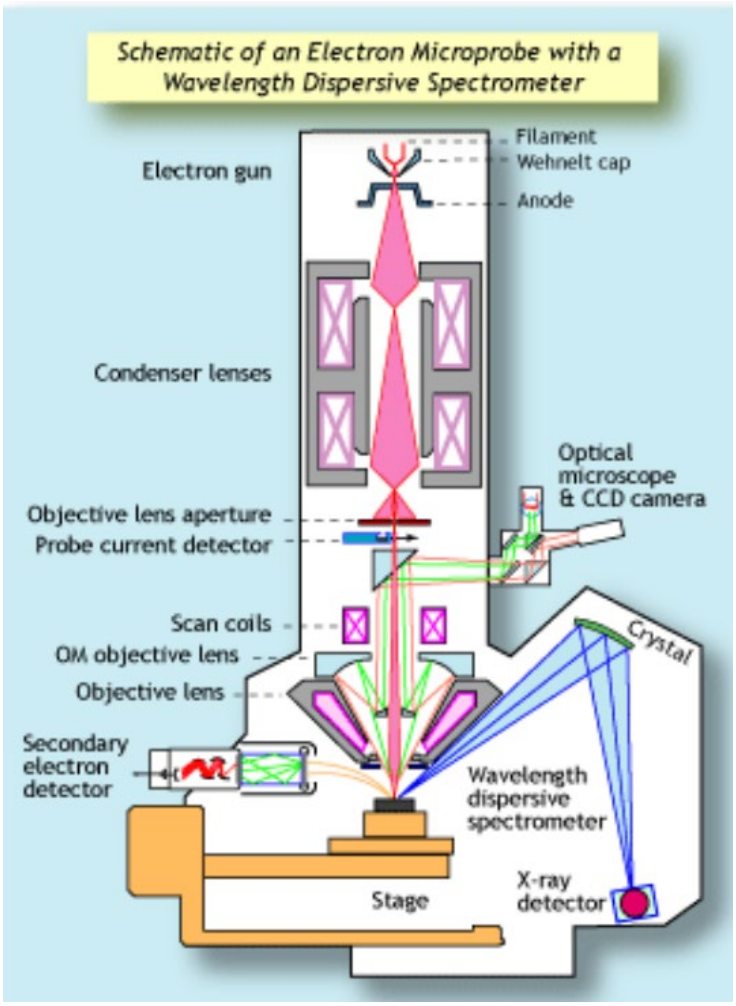

Figure 48. Schematic of an EPMA with attached WDS (McSwiggen & Associates, -Tech Note: WDS vs EDS, n.d.; Wavelength-Dispersive Spectroscopy (WDS), n.d.).

In a series of papers by Wright et al., EPMA was used to analyze the fission product concentrations and distributions throughout every layer of multiple TRISO particles from the AGR-1 and AGR-2 programs. For the two TRISO particles analyzed during the AGR-2 study, fission product concentrations and distributions were obtained and then compared to those predicted from ORIGEN modeling calculations. Data collected from these measurements showed that the fission product masses determined for the two particles were within ± 20% of the calculated masses for the rare earth elements molybdenum, zirconium, cesium, iodine, and palladium. The silver mass measured differed by more than 40% from the calculated mass. It was also observed that lanthanides other than europium remained primarily within the fuel kernel for the as-irradiated particle but were divided approximately equally between the kernel and kernel periphery for the safety-tested particle. In both particles, the majority of strontium and europium accumulated in the carbon rich kernel periphery. A greater mass fraction of mobile elements, such as cesium and iodine, accumulated in the buffer and IPyC regions in the safety-tested particle as compared to the as-irradiated particle. While the EPMA technique used in this study has not been fully developed and tested, it is believed that the mass balance approach used has the potential to provide insight into TRISO particle fuel behavior (Wright et al., 2021, 2022; Wright & van Rooyen, 2016). The EPMA scan path for the AGR-1 particles can be seen in Fig. 49 while the cesium concentrations and distributions and ORIGEN mass calculation comparisons can be seen in Fig. 50.

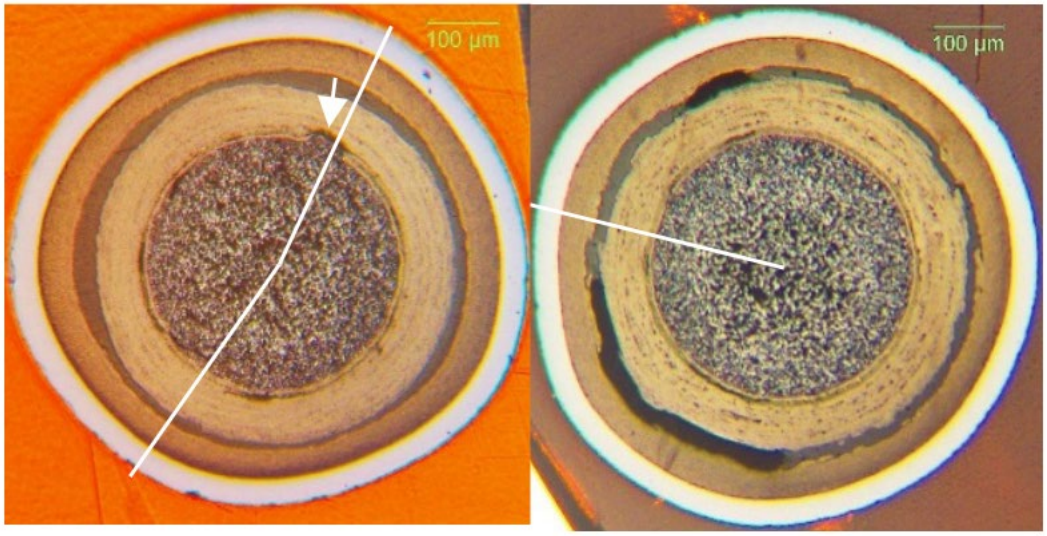

Figure 49. EPMA scan path use for AGR-1 particles (Wright & van Rooyen, 2016).

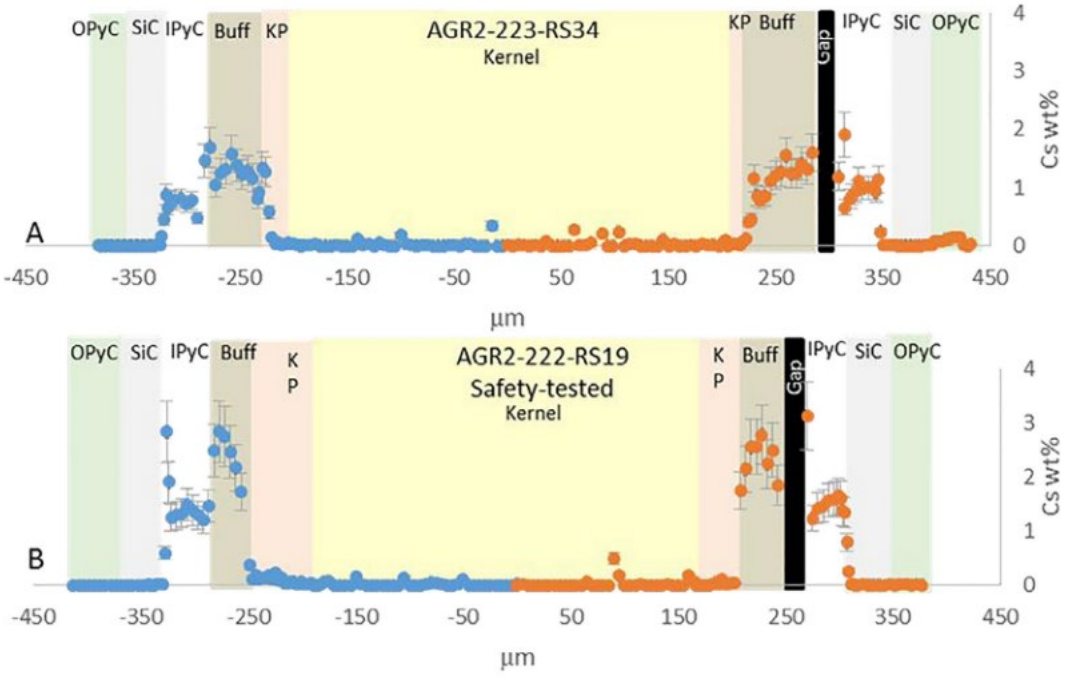

Element, µg/particle	EPMA (AGR2-223-RS34)	Origen (AGR2-223-RS34)	fractional difference	EPMA (AGR2-222-RS19)	Origen (AGR2-222-RS19)	fractional difference
U	381	346	1.10	375	339	1.11
La	1.69	1.57	1.08	2.17	1.82	1.19
Ce	3.34	3.03	1.10	4.13	3.53	1.17
Pr	1.46	1.45	1.01	1.88	1.68	1.12
Nd	5.28	5.24	1.01	7.04	6.12	1.15
Sm	1.08	0.90	1.19	1.30	1.06	1.23
Eu	0.12	0.13	0.91	0.17	0.15	1.08
Mo	4.81	4.21	1.14	5.60	4.91	1.14
Ru	3.13	2.36	1.32	3.22	2.81	1.15
Zr	5.04	4.84	1.04	6.32	5.61	1.13
Xe	0.38	6.57	0.06	0.51	7.77	0.07
Cs	2.50	3.13	0.80	3.29	3.55	0.93
I	0.22	0.23	0.97	0.29	0.27	1.07
Ba	2.21	2.00	1.11	3.76	2.36	1.59
Sr	1.56	1.22	1.28	1.34	1.39	0.96
Te	1.27	0.52	2.45	2.51	0.61	4.13
Pd	0.80	0.99	0.81	1.13	1.29	0.88
Cd	0.01	0.06	0.17	0.02	0.07	0.24
Ag	0.07	0.05	1.41	0.11	0.07	1.62

Figure 50. Cesium fission product concentrations and distributions found in the AGR-2 particles (top) and ORIGEN mass calculation comparisons (Wright et al., 2022).

2.25 APT-TEM Correlation

Atom probe tomography (APT) is an atomic scale microstructural characterization technique that provides three-dimensional compositional mapping with sub-nanometer resolution. APT is highly sensitive and can detect the population of any element in a material down to the parts per million range (see Fig. 51). APT is centered on controlled field ionization and the evaporation of individual atoms from the surface of finely tipped samples. The samples used are sharpened to a point of less than 100 nano meters. To yield information from the sample evaporated ions are accelerated towards a position sensitive multichannel plate detector that records the impact position, and the time-of-flight of the individual atoms. The original position of the atoms inside the specimen can then be derived through quantitatively evaluating the detected positions and the detection sequence of the individual atoms. This reconstruction procedure has been shown to have an accuracy of within a few Ångströms in suitable cases. To determine the chemical identity of

the sample, the time-of-flight of the individual atoms is evaluated. When evaluating time-of-flight, field evaporation is triggered by either short laser pulses or superposed additional electric field pulses. From this, each atom can be assigned a characteristic mass-to-charge-state ratio. By counting the number of ions having a given mass-to-charge-state ratio, a complete compositional analysis of the material can be obtained. The information is presented as a spectrum, with each element being represented by a distinct peak. This is very similar to how each element has its own separate spectral peak in EDS, as seen in Fig. 52. For APT, even different isotopes of the same element can be resolved. This appears as a series of peaks with intensities proportional to the natural isotope abundance (Amouyal & Schmitz, 2016). Unlike EDS or WDS, APT can detect light elements such as carbon, hydrogen, helium, and lithium with ease. This capability allows for unique insights into the composition of lifetime-limiting or performance-enhancing microstructural features. This ability makes APT ideally suited to complement other microstructural characterization techniques, including a multitude of TEM analysis techniques (Gault et al., 2021). The pairing of APT and TEM capabilities is referred to as APT-TEM analysis, where the strengths of both techniques can be applied to the same specimen (see Fig. 53).

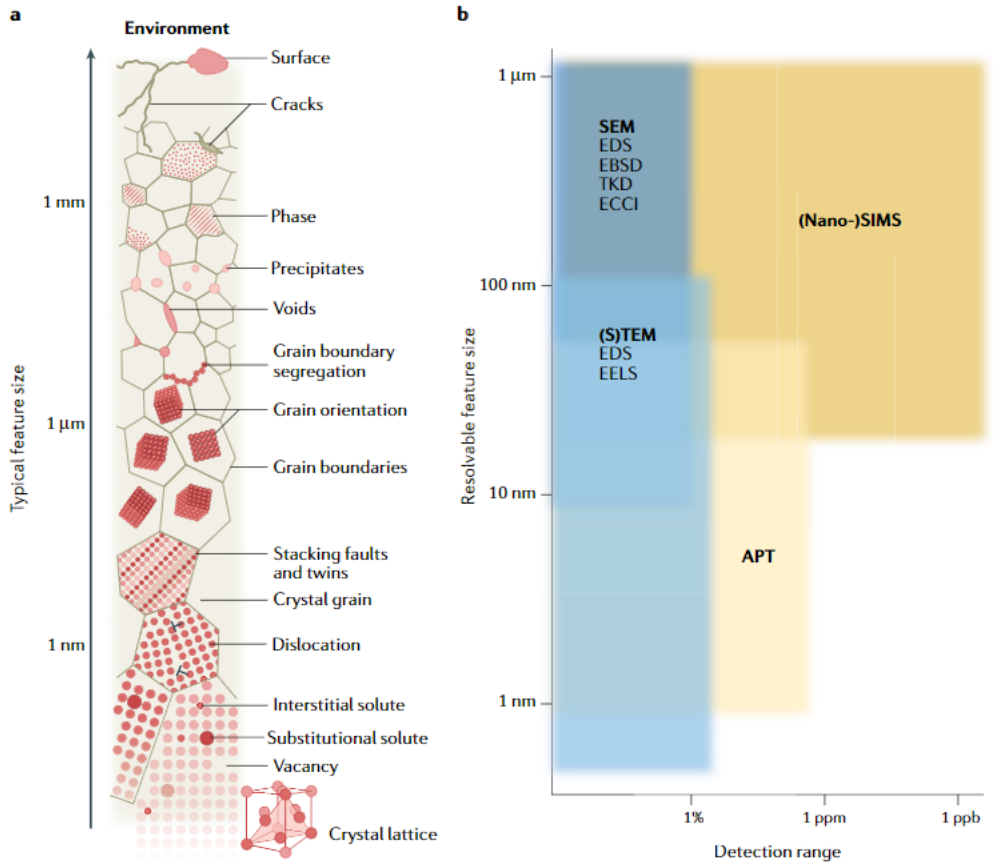

Figure 51. Resolvable features and detection range of APT in comparison to other characterization techniques (Gault et al., 2021).

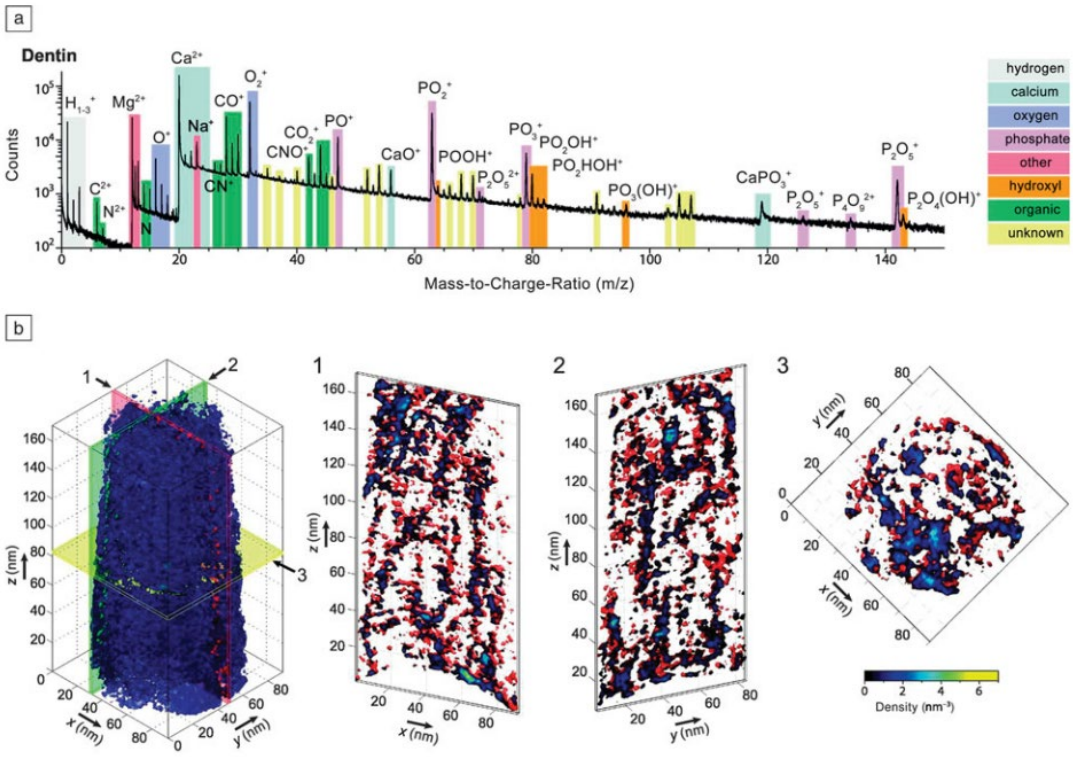

Figure 52. The graph in part a) showcases a mass-to-charge-state ratio spectrum typically seen in APT. Accompanying the graph in part a), the model in part b) exemplifies the three-dimensional compositional mapping commonly seen in APT (Amouyal & Schmitz, 2016).

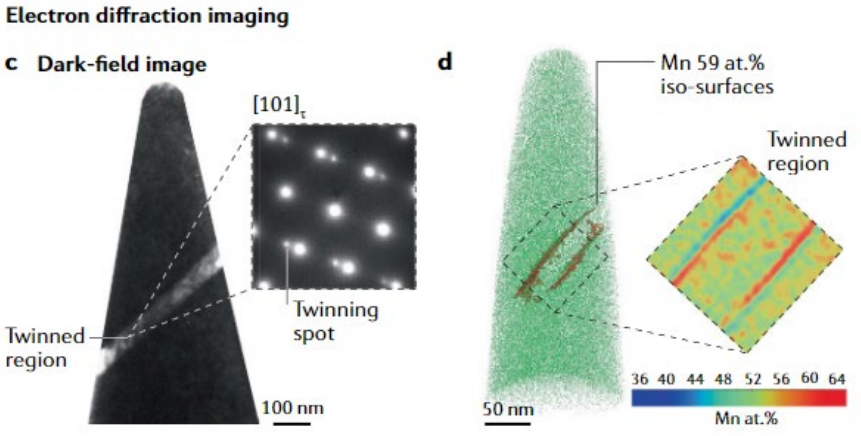

Figure 53. Side by side comparison of TEM analysis (left) and APT analysis (right) applied to the same atom probe sample (Gault et al., 2021).

In several studies conducted by Fu et al. and van Rooyen et al., APT-TEM analysis was used to quantify the fission product distribution in select areas of AGR-1 TRISO particles. In the 2016 study, an unirradiated surrogate TRISO APT sample tip that underwent quantitative analysis indicated that concentrations of carbon and silicon within the atom probe volume were 44.81 at.% (error 0.01 at.%) and 53.96 at.% (error 0.01 at.%), respectively. Further APT analysis of another unirradiated surrogate TRISO particle revealed similar concentrations of carbon and silicon of about 45 at.% and 54 at.%, respectively. The authors believe this may indicate non-stoichiometry of the SiC. For the irradiated TRISO APT tip, a silver–palladium–uranium phase was identified at one side of the reconstructed volume (see Fig. 54). Through quantitative analysis within the silver–palladium–uranium rich phase, the normalized concentrations of palladium, silver, uranium, silicon, and carbon were 12.1 at.% (error 0.3 at.%), 3.5 at.% (error 0.2 at.%), 3.3 at.% (error 0.1 at.%), 60.0 at.% (error 0.3 at.%), and 21.2 at.% (error 0.2 at.%), respectively. For the 2018 study, the APT data revealed segregation of tellurium and silver at the UO-UC interface within the TRISO particles kernel. The UO phase displayed a presence of fission products such as palladium, zirconium, cesium, neodymium, erbium, dysprosium, gadolinium, lanthanum, yttrium, xenon, and samarium while the UC phase displayed higher concentrations or segregation of rhodium, rubidium, zirconium, xenon, cadmium, indium, tin, technetium, and niobium (see Fig. 54). Interestingly, no cesium was detected during this investigation. The 2020 study confirmed the 2018 study when it found that fission products zirconium, niobium, molybdenum, rhodium, rubidium, and technetium preferentially segregated into the UC phase to form metallic precipitates while the lanthanide fission products tended to stay in solution of the UO phase (Fu et al., 2020; van Rooyen et al., 2016, 2018).

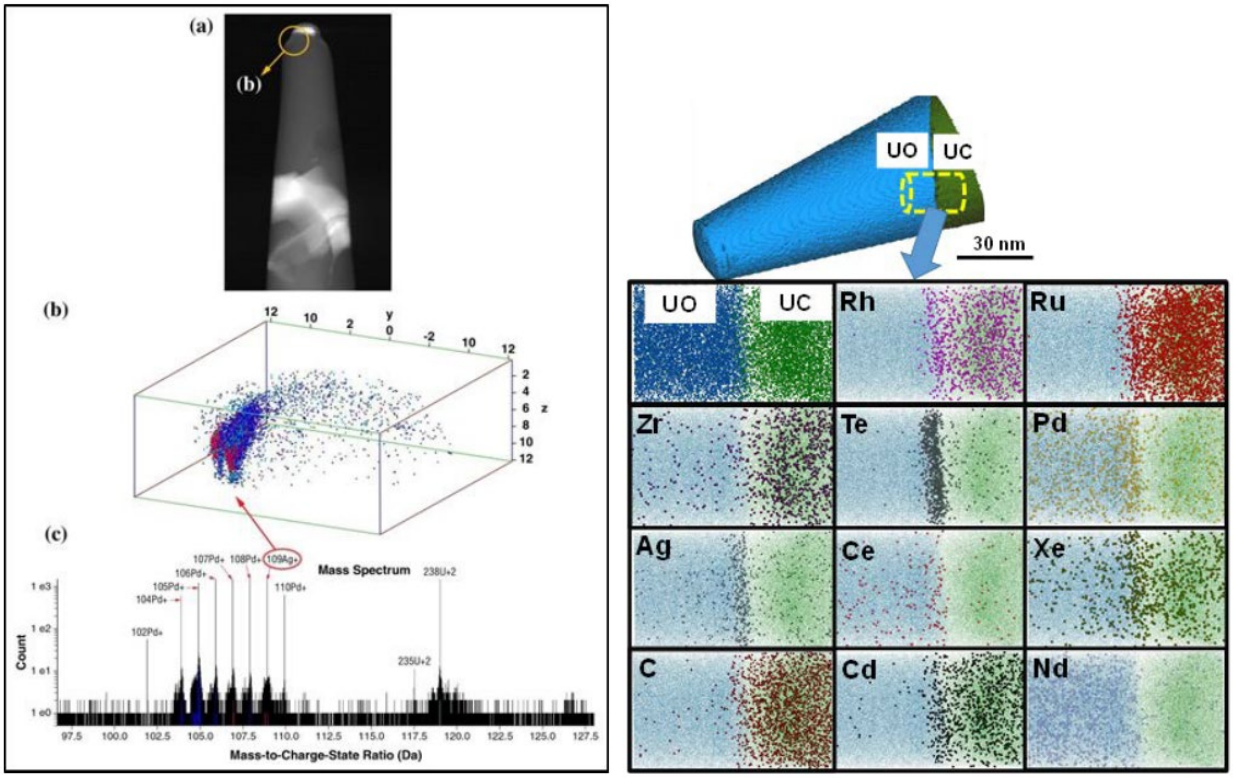

Figure 54. Silver–palladium–uranium phase found in irradiated TRISO APT tip (left) and UO-UC interface fission product distribution (right) (van Rooyen et al., 2016, 2018).

3.0 Methods and Materials

3.1 Instruments

3.11 FEI FIB SEM Dual Beam 835

The instrument used for the fabrication of the baseline samples and one surrogate TRISO micro-tensile sample in this dissertation was a FEI Dual Beam 835 located at the Eames complex on ISU's campus in Pocatello, Idaho. This machine was built in the year 2000 and was originally meant for use in the silicon wafer industry but has since been adapted for use in micro-tensile sample fabrication. The primary working components on this machine used in the tensile sample fabrication process are the gallium focused ion beam (FIB), scanning electron microscope field emission gun (SEM-FEG), tungsten and platinum gas injection systems (GIS), and nano manipulator. Fig. 55 shows the components of the Dual Beam. All samples are loaded through the

front load lock and pass into the vacuum chamber with the help of a loading arm. Once inside the chamber, the sample sits on a stage that can move in the x, y, and z directions, rotate through a full 360°, and tilt beyond 52°. Using the primary working components and the maneuvering capabilities of the stage and nano manipulator, complex lift-out and tensile sample fabrication processes were possible (Mauseth, 2021).

Figure 55. In the top image, one can see the front view of the outside of the Dual Beam 835 with the load lock marked with the gray arrow. In the bottom image, the working components of the Dual Beam are visible with the Magnum FIB column marked with the orange arrow, the platinum GIS marked with the yellow arrow, the tungsten GIS marked with the blue arrow, the SEM column marked with the black arrow, and the Omniprobe nano manipulator marked with the green arrow (Mauseth, 2021).

3.12 Thermo Fisher Scientific Versa 3D FIB SEM Dual Beam

Originally, the instrument planned for the imaging and videoing of the baseline samples and one surrogate TRISO tensile sample tensile tests for this dissertation was a FEI Quanta 200F SEM located at the Eames complex in Pocatello, Idaho. Due to technical difficulties, however, this instrument was unavailable. The instrument used for the imaging and videoing of these tensile tests was a Thermo Fisher Scientific FIB SEM Versa 3D located at Bruker Hysitron's headquarters in Eden Prairie, Minnesota. An image of this machine can be seen in Fig. 56. While this machine has a FIB, an SEM, and a GIS, only the SEM was used for its imaging capabilities. The chamber of this machine is accessed through the front sliding door and allows ample room for loading and unloading of the sample and the sample holder. Videos and still images were taken during the tensile testing (Mauseth, 2021).

Figure 56. Image of a Versa 3D (THERMO FISHER SCIENTIFIC, 2021). The SEM column is marked with the gray arrow and the front of the vacuum chamber is marked with the orange arrow.

3.13 FEI Quanta 3D/650 FIB SEM Dual Beam/FEG-SEM

FEI's Quanta 3D/650 FIB SEM Dual Beam/FEG-SEM model has been utilized in three separate locations throughout the duration of this dissertation work. The three locations are the Microscopy and Characterization Suite (MaCS) at the Center for Advanced Energy Studies (CAES), the Idaho National Lab Research Center (IRC) (only SEM, no dual beam), and the Irradiated Materials Characterization Laboratory (IMCL) at the Materials Fuels Complex (MFC) at the Idaho National Lab (INL). As each of these locations utilize the same model, only the machine at the IMCL will be explained in detail here. According to the IMCL's instrument description, the IMCL FEI Quanta 3D field emission gun (FEG) dual beam instruments consist of a high-resolution field emission scanning electron microscopy (SEM) column optimized for high brightness and high current, and a high-current focused ion beam (FIB) column with a liquid gallium metal ion source. The microscopes are equipped with Omniprobe micromanipulators for in-situ sample lift-out and a gas injector system for platinum and carbon deposition (Materials and Fuels Complex - Shielded FEI Quanta 3D FEG, n.d.).

According to the IMCL's instrument application information, the main uses for these instruments are microstructural and elemental characterization as well as site-specific transmission electron microscopy and atom probe tomography sample preparation from nuclear fuel, cladding and structural materials. These instruments are also used for performing 3-D microstructural and elemental characterization (tomography) (Materials and Fuels Complex - Shielded FEI Quanta 3D FEG, n.d.). An image of the IMCL's FEI Quanta 3D FIB SEM Dual Beam can be seen in Fig. 57, while an illustration of the inner components typically found inside dual beam microscopes can be seen in Fig. 58. Fig. 59 gives specifications of the instrument as seen on the IMCL's website.

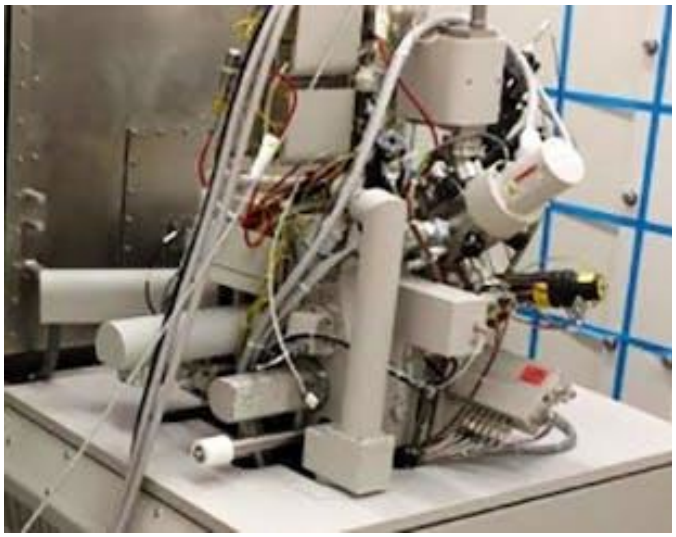

Figure 57. Image of the IMCL's FEI Quanta 3D FIB SEM Dual Beam (Materials and Fuels Complex - Shielded FEI Quanta 3D FEG, n.d.).

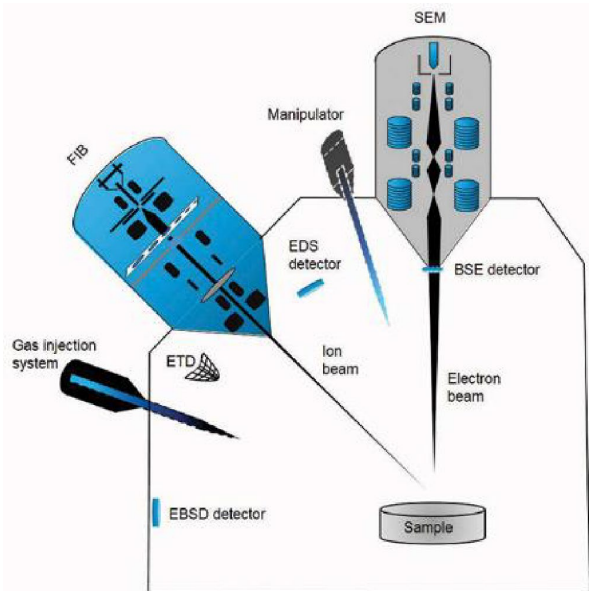

Figure 58. Illustration of the inner components typically found inside dual beam microscopes (Wolff, 2020).

Resolution electron beam: In high-vacuum mode (also capable of low-vacuum mode operation)	1.2 nm at 30 kV 2.9 nm at 1 kV
Resolution ion beam:	7 nm at 30 kV
SEM optics:	High-resolution field emission SEM Acceleration: voltage is adjustable from 200 V to 30 kV Probe current: up to 200 nA, continuously adjustable Magnification: 30 x–1.28 Mx
FIB optics:	High-current ion column with Ga liquid metal ion source Magnification 40 x – 1.28 Mx
Detectors:	Everhardt-Thornley SED (ETD) Secondary electron and secondary ion detector (CDEM) IR camera for viewing sample/column Electron or ion beam current measurement
Stage:	X, Y, Z, R and T 5 axes mechanical stage Eucentric and analytical WD: 10 mm
Gas injector system	Gases: platinum, carbon
Sample manipulator:	Omni Autoprobe 200, no motorized rotation

Figure 59. Instrument specifications for the IMCL's FEI Quanta 3D FIB SEM Dual Beam (Materials and Fuels Complex - Shielded FEI Quanta 3D FEG, n.d.).

3.14 Bruker Hysitron PI 88 SEM PicoIndenter

The instrument used for the direct in-situ micro-tensile test in this dissertation was a Bruker Hysitron PI 88 SEM PicoIndenter. This machine holds the sample mount on an advanced XYZ positioning stage capable of nanometer sized movements. Opposite of the sample the machine hosts a transducer that is vacuum compatible and provides electrostatic actuation and capacitive displacement sensing on the micro-newton scale. The end of the transducer contains a threaded post that allows for screw-on probes. An image of the PI 88 is shown in Fig. 60. After the sample and screw-on probe are attached, the PI 88 is mounted within a SEM or FIB/SEM for imaging of the tests being conducted (Mauseth, 2021).

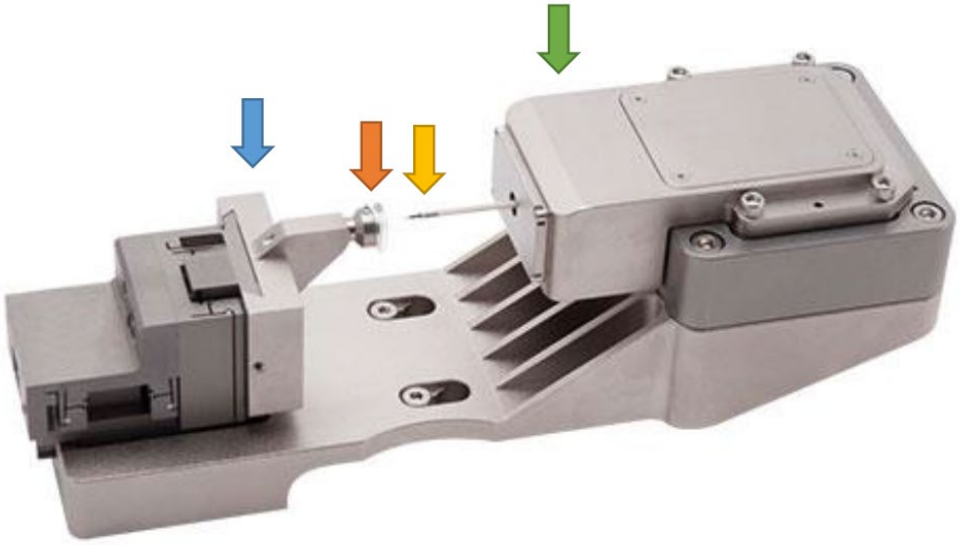

Figure 60. Image of the PI 88 SEM PicoIndenter base system. The positioning stage is marked with the blue arrow, the sample mount is marked with the orange arrow, the threaded post with screw-on probe is marked with a yellow arrow, and the transducer is marked with a green arrow (PI 88 SEM PicoIndenter ®, 2020).

3.2 Sample Fabrication

3.21 Diamond Gripper

A Bruker Hysitron cube cornered diamond indentation probe served as the base material for the fabrication of the diamond grippers used in the micro-tensile test. This probe has a centerline-to-face angle of 35.3° and is designed to be screwed onto the threaded post of the PI 88's transducer. While the cube cornered probe performed well with our micro-tensile samples, it did not perform well with other micro-tensile samples with less clearance around the base. Since our micro-tensile samples were protruding into open space, we did not have a problem with the base running into the bulk of the sample (Mauseth, 2021). Conical shaped indentation probes should be considered for future gripper fabrication because of their high centerline-to-face angle (greater than 35.3°), which will prevent the base of the probe from running into the base of low clearance tensile samples.

The first step in fabricating the diamond gripper is properly aligning the diamond nano indentation probe onto the Ted Pella 45° pin stub holder. This is done by first screwing the probe onto the PI 88's threaded post and marking the top of the probes shaft with a black marker. This helps orient the probe relative to the PI 88. Next, after applying copper tape underneath and above the 45° pin stub holder, very carefully place the probe on top of the 45° pin stub holder with the black mark facing orthogonal to the 45° pin stub holder face and the probe tip facing upwards. Copper tape serves as an adhesive to secure the pin stub holder and to discharge any charge buildup accrued on the samples through using the FIB and SEM. The 45° pin stub holder is then placed on top of the center of the custom-made aluminum sample holder attachment (Mauseth, 2021).

After the diamond probe enters the Dual Beams vacuum chamber, the stage is brought to eucentric height. At eucentric height the sample, ion beam, and electron beam intersect. The eucentric height is important because it allows the ion and electron beams to view the same point on the sample. After the stage is brought to eucentric height, the stage is tilted seven degrees to align the diamond probe with the ion beam. The stage needs to be tilted because the ion beam is angled exactly 52 degrees from the orthogonally positioned electron beam and the pin stub holder is angled at 45 degrees. After alignment, the first cut involved placing two 80-μm wide, 25-μm tall, 40-μm deep parallel trenches separated by a 10-μm gap with the tip of the probe placed in the center of this gap and facing directly towards the ion beam. Because this cut would be considered a large bulk cut the larger aperture (20-nA) was used. The aperture is synonymous with how powerful the ion beam is. A visualization of the alignment and cutting conducted is shown in Fig. 61 (Mauseth, 2021).

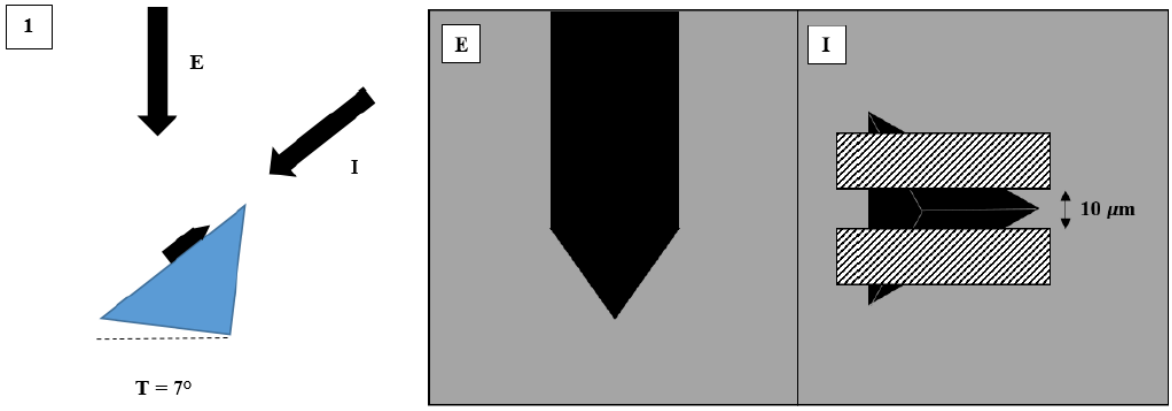

Figure 61. The graphic on the left demonstrates the alignments that were involved in the first step. The graphic on the right displays what each beam saw from this angle. T represents the stage tilt, E the electron beam, I the ion beam, and the textured gradient representing where the FIB cut into the sample (Mauseth, 2021).

After the first cut was finished, the stage was rotated 180° to face the tip perpendicular to the ion beam and expose the trench face. The second cut created a 20-μm wide by 8-μm tall block protruding from the entrenched face of the diamond tip. The five and seven nano amp apertures were used for this cut because they created finer cuts but were still powerful enough to finish the milling in a reasonable amount of time. Illustrations of the exposed block are shown in Fig. 62 (Mauseth, 2021).

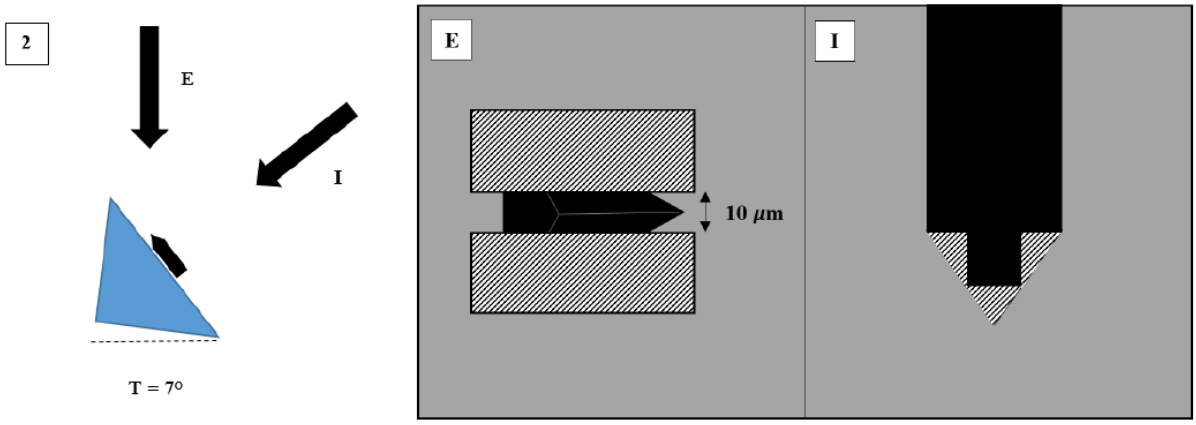

Figure 62. Alignment of the sample for the block exposing step is shown on the left while a side by- side graphic of the electron beam and ion beam perspective during this milling step is shown on the right (Mauseth, 2021).

The third step involved rotating the stage 180° back to its original position facing the ion beam where the protruding block was thinned down from 10-μm thick to 5-μm thick. The smaller (1-5 nA) apertures were used for this step. It should be noted that the further along the fabrication process progresses the smaller and smaller the apertures get. This is because the larger apertures are no longer needed to clear away a lot of material so the sharper, smaller apertures become more desirable for fine details. Fig 63. illustrates the block thinning procedure (Mauseth, 2021).

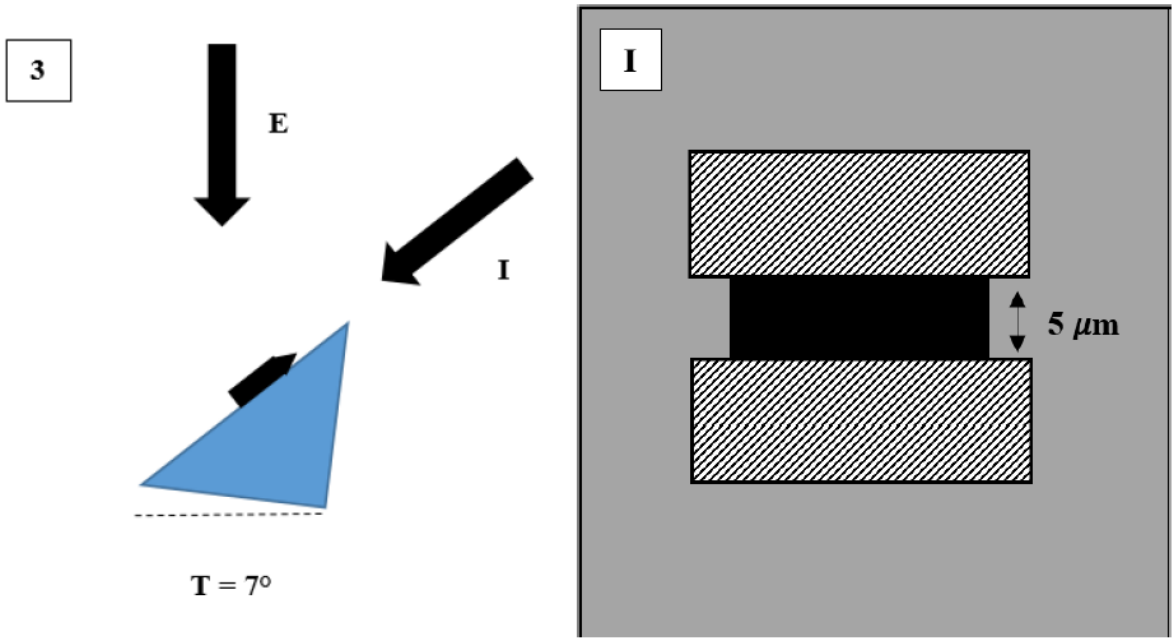

Figure 63. The alignment and visual from the ion beam perspective of the block thinning step for the fabrication of the diamond grippers (Mauseth, 2021).

The fourth and final step involved rotating the stage 180° back to the perpendicular facing position to the ion beam where an 11.3-μm wide by 8-μm tall square hole was extruded from the block. An additional cut was made at the bottom of the square hole to produce a 5.5-μm opening at the bottom of the block. The summation of these cuts produced a diamond gripper with gripping prongs 3.1-μm wide and 2.8-μm thick and an internal cavity 11.3-μm wide by 8-μm tall. All these final cuts were done using the one nano-meter aperture. Fig. 64 and 65 illustrate the final alignments and display the final diamond grippers used for all micro-tensile tests conducted during this dissertation (Mauseth, 2021).

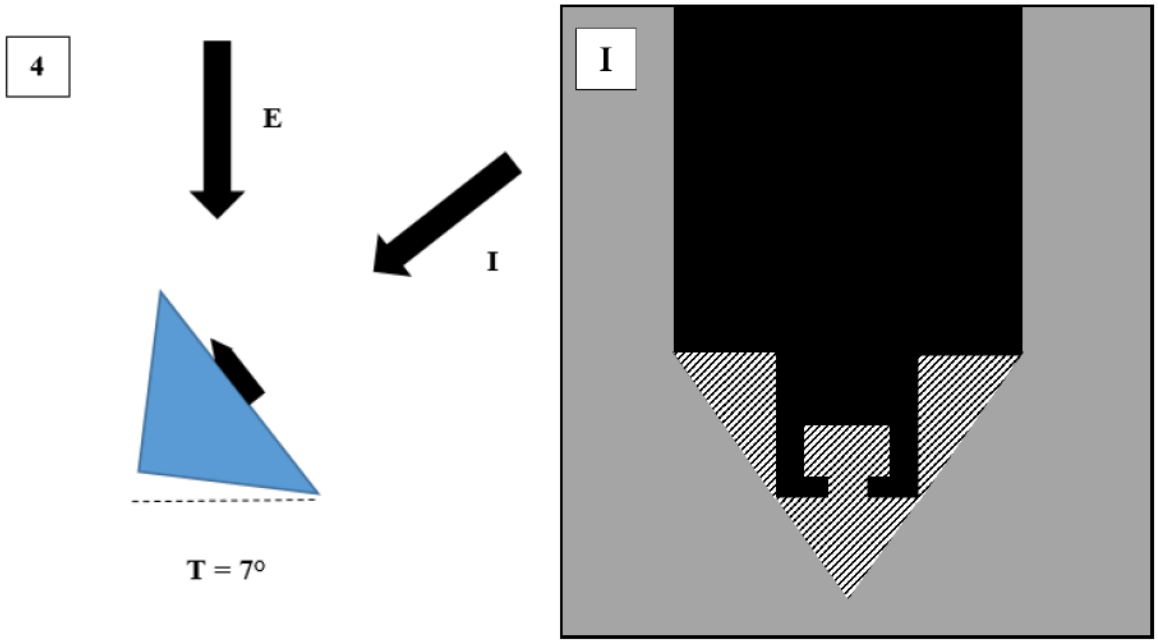

Figure 64. The final cuts and alignments involved in fabricating the diamond grippers (Mauseth, 2021).

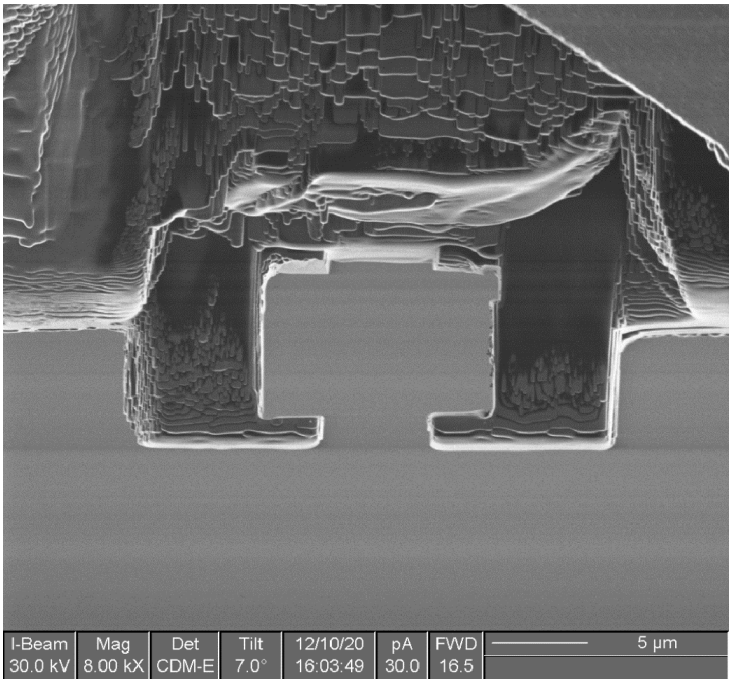

Figure 65. The completed diamond grippers used in every single micro-tensile test during this dissertation (Mauseth, 2021).

3.22 Baseline Material Micro-tensile Samples

Before any micro-tensile samples could be fabricated, pin mounts and stub holders needed to be acquired onto which the samples would be placed. A Ted Pella 45° pin stub holder and a Ted Pella low profile 90° FIB pin mount were used to serve this purpose. Fig. 66 shows images of these holders.

Figure 66. From left to right: Ted Pella low profile 90° FIB pin mount, Ted Pella 45° pin stub holder, and pin mount in stub holder (Mauseth, 2021).

For the fabrication of the copper, molybdenum, and silicon micro-tensile samples copper and molybdenum Omniprobe lift-out grids and silicon PELCO lift-out grids from Ted Pella were used as the base materials. The copper and molybdenum lift-out grids each have five posts and typically have a thickness of 25-30μm and a diameter of 3-mm. The silicon lift-out grids each have four posts, and are 80-μm wide, 100-μm thick, and 190-μm high. Images of each half-grid are shown in Fig. 67 (Mauseth, 2021).

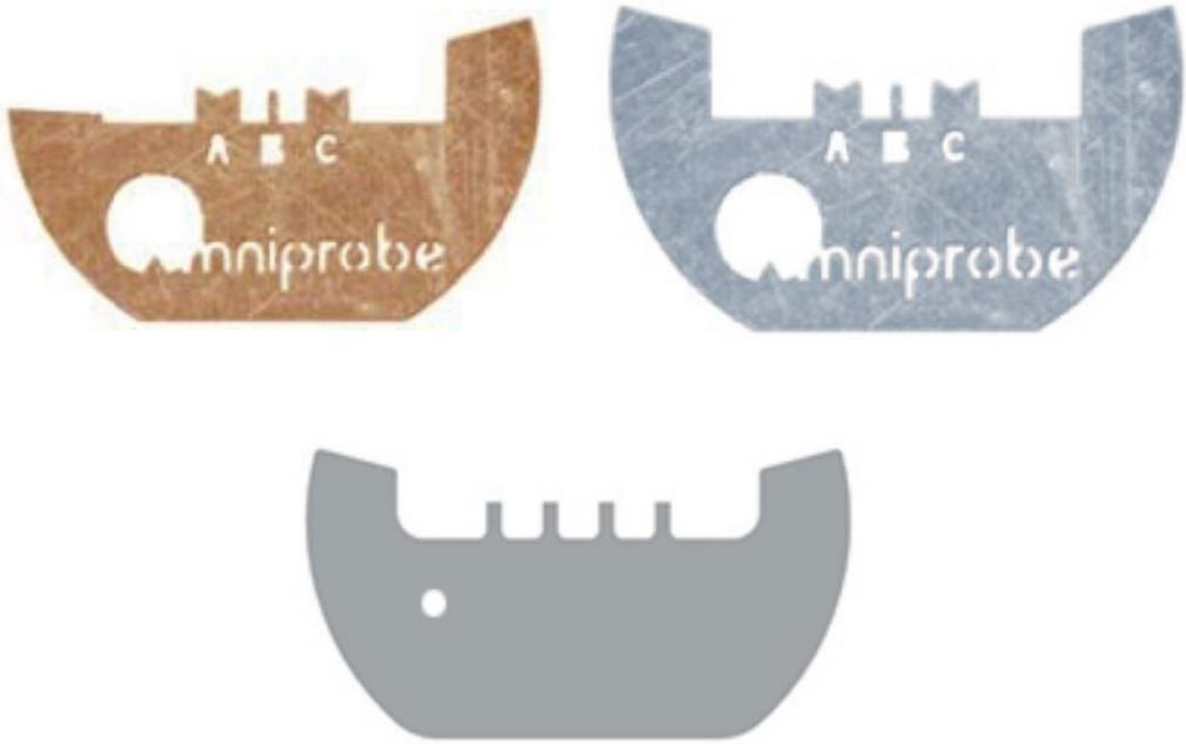

Figure 67. Images of the FIB lift-out grids. The upper left grid is copper, upper right grid is molybdenum, and bottom grid is silicon (Ted Pella, 2020).

The copper, molybdenum, and silicon dog bone shaped tensile samples were all fashioned in a similar manner, with the only differences being variance between the material hardness of the different materials (affecting mill time) and the varying thickness of the FIB lift-out grids. The samples were mounted to a 90º pin stub using copper tape and braced against a plastic box for keeping the stub steady. Two lift-out grids of each material were attached to each material's respective pin stub. The 90° pin stub was then attached to the 45° stub holder with the help of copper tape. This micro-tensile sample pin set-up was then attached on top of the center of the custom-made aluminum sample holder attachment using copper tape (Mauseth, 2021).

After the micro-tensile sample pin stub set-up entered the Dual Beams vacuum chamber, the stage was brought to eucentric height and tilted seven degrees to align the micro-tensile sample pin stub set-up with the ion beam for the same reason as described for the diamond probe. The first step in milling the dog bones was exposing a 16-μm wide, 8-μm tall, and 20-μm deep cross-section block from the grid post tip that faces the ion beam. This was typically done with the 20 nano-amp aperture. After exposing this block the stage was rotated 180° to the perpendicular facing position where the exposed block was then refined into an 8-μm wide by 15-μm tall block. The five or seven nano-amp aperture was used for this second step. An image of the copper post and an illustration demonstrating this first step are shown in Fig. 68 (Mauseth, 2021).

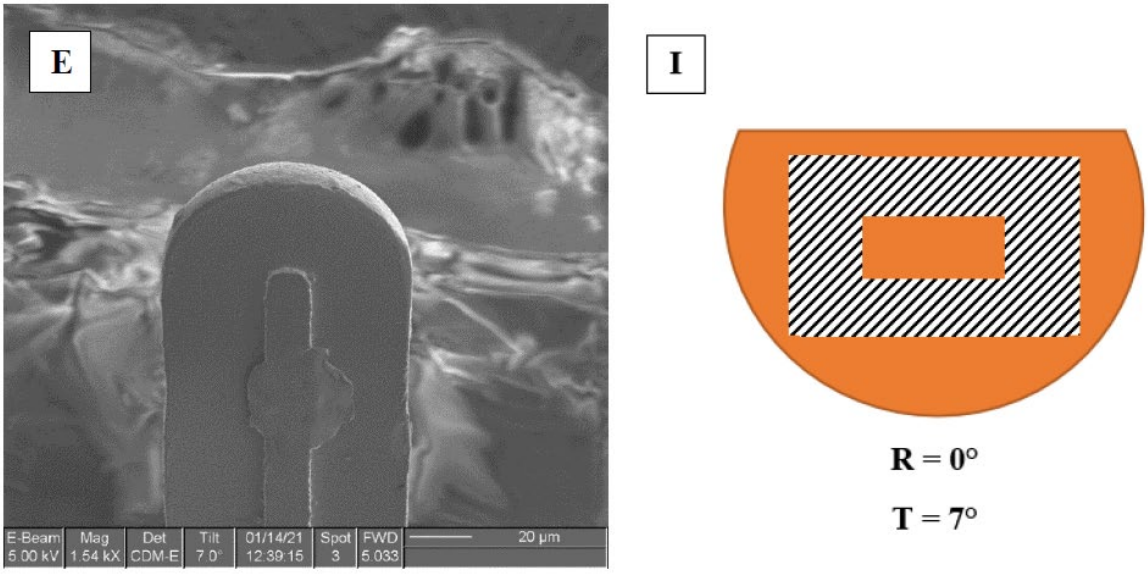

Figure 68. Image of an untouched copper lift-out grid post from the perspective of the electron beam and an illustration from the perspective of the ion beam helping to visualize where the first cuts were placed when the fabrication process began on the half-grids. The value R represents the rotation angle of the stage at the first step, T the stage tilt, and the textured gradient representing where the FIB cut into the sample (Mauseth, 2021).

After the block was uncovered, the stage was rotated 180° to face the ion beam and the protruding block was thinned from 8-μm to 2-μm. The three nano-amp aperture was used for this

third step. The final step involved the stage being rotated 180° back to the perpendicular facing position where two 3-μm wide by 6-μm tall cuts were placed parallel to each other to create the dog bone shape. An illustration of this can be seen in Fig. 69. It should be noted that the stage remained at a seven degree tilt throughout the entire milling process to maintain proper alignment with the ion beam. Every dog bone was designed to be 15-μm tall, 8-μm wide, and 2-μm thick with a tensile gauge section 6-μm tall by 2-μm wide and a bottom portion (head section) 4-μm tall. An image of one of the final dog bones and a panoramic view of one of the completed molybdenum lift-out grids is shown in Fig. 70. While the molybdenum FIB lift-out grid consisted of harder material than the copper FIB lift-out grid, it took less time to mill the dog bones because it has significantly thinner posts (25-μm vs 50-μm) tips that tapered almost to a point. The silicon FIB lift-out grid took by far the longest time, as it was the hardest material and had 100-μm thick posts. In total, 10 copper, 10 molybdenum, and 8 silicon dog bones were created (Mauseth, 2021).

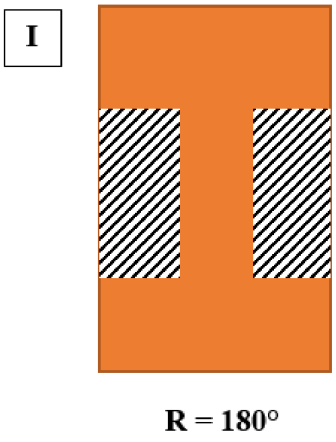

Figure 69. Illustration of the dog bone milling step, with R signifying the rotation of the stage, I demonstrating that this is from the perspective of the ion beam, and the textured gradient representing where the FIB cut into the sample (Mauseth, 2021).

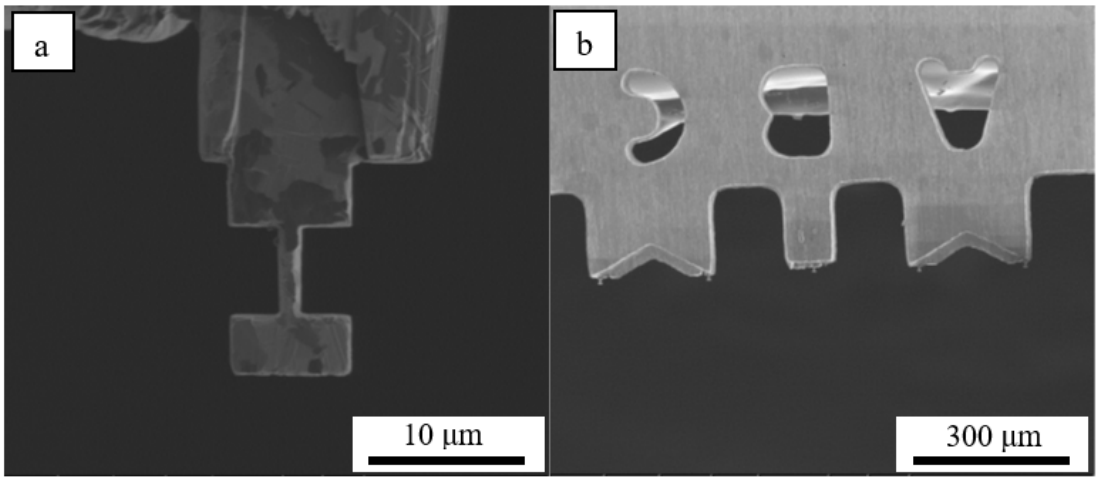

Figure 70. The image on the left is an example of a completed copper dog bone tensile sample while the image on the right displays an entire lift-out grids' worth of molybdenum dog bone tensile samples (Mauseth, 2021).

3.23 TRISO Particle Preparation

The surrogate micro-tensile samples for this dissertation were prepared from the coating layers of experimental fuel surrogate (ZrO_2) TRISO coated particles (Batch D) fabricated in the 5kg load capacity Advanced Coating Facility (ACF) of the PBMR Fuel Development Laboratories at NECSA in South Africa. The Batch D TRISO particles were produced using SiC layer deposition temperatures of 1450 ºC, with a deposition rate of 0.23 µm/minute resulting in a 39 µm thickness. The buffer layer for these particles is approximately 90 to 100 µm thick with a 50% void volume fraction. The IPyC layer for these particles is approximately 72 µm thick with a specific density of 1.67 g/cm^3 (Mae, 2014; Van Rooyen et al., 2010). When coated particle (CP) layer deposition is complete for these particles, a high temperature purification sintering process at approximately 1950°C for 1 hour is generally necessary for the completion of the fuel compact fabrication process. As this set of batch D particles was not yet consolidated in the fuel compaction process, this set of batch D particles was annealed after CP fabrication in a resistance-heated Webb 89 vacuum furnace at the Nelson Mandela Metropolitan University at 2000℃ for 30 minutes under

an argon atmosphere. The samples were loaded in graphite or ceramic holders at room temperature and heated to the required temperature at a rate of 25°C per minute and were furnace-cooled to room temperature (Mauseth et al., 2023; Van Rooyen I, 2011).

The surrogate TRISO particles were provided in an epoxy resin compact that was polished down to expose the ZrO_2 kernels. The surrogate TRISO particles were mechanically thinned to approach a hemispherical shape using a Buehler Beta grinder polisher (exposing the various layers of coating) and polished using a 0.05 μm colloidal silica suspension. Upon further inspection one may notice that the surrogate TRISO particles display some dimensional anisotropy. The surrogate TRISO particles do, however, demonstrate a high degree of symmetry. Additionally, a variation in the diameter of the surrogate TRISO particles can be observed. This variation is due to the particles being suspended at a non-uniform level in the epoxy resin. As a consequence, not all surrogate TRISO particles were polished to the same depth (Mae, 2014). It should be noted that because the IPyC layer of the surrogate TRISO particle in this study is composed of medium texture carbon material, anisotropic mechanical effects may be present (Kabel et al., 2021; Reznik & Hüttinger, 2002). However, because the samples were taken from the same parent surrogate TRISO particle, any directional variations remain consistent from one sample to another. By visual inspection, the layers appear to be close in scale to what would be expected at midplane for the surrogate TRISO particle with craters illustrated in Fig. 73b, making any such variations from midplane minor. As such, it should be acknowledged that since only one surrogate TRISO particle was measured and the layers have some degree of variation from midplane, the tensile data may be precise for this single surrogate TRISO particle sample but not accurate for TRISO coated particle fuel in general. This inaccuracy is primarily due to the unavoidable variations between individual particles and geometric variations due to the layers not being polished to directly at

midplane. As the pore shape and structure of the layers align with the radial growth direction of the TRISO particle (zero degrees from midplane), any deviation from midplane results in tensile properties being measured at an angle diverging from the growth direction (Griesbach et al., 2023). This divergence can lead to a variation in the observed tensile response, lending the tensile results inaccurate (Mauseth et al., 2023). Images of two epoxy pucks containing surrogate TRISO particles from South Africa can be seen in Fig. 71.

Figure 71. Images of the two epoxy pucks containing surrogate TRISO particles from South Africa (Mauseth, 2021).

The unirradiated micro-tensile samples for this dissertation were prepared from the coating layers of UCO fueled TRISO particle LEU09 from AGR-2 Batch G73J-14-93073A. The AGR-2 fuel fabrication conditions and properties are well documented. As quoted from the AGR-2 TRISO Fuel Post-Irradiation Examination Final Report,

"The AGR-2 kernels and TRISO coated particles were fabricated at BWX Technologies Nuclear Operations Group (BWXT NOG) in Lynchburg, Virginia and evaluated according to the AGR-2 Fuel Product Specification (Barnes 2009). The UCO fuel kernels were nominally 425 µm

in diameter and comprised of low-enriched uranium (LEU) that was 14.0 wt.% ^{235}U. The UO_2 fuel kernels were fabricated to enrichments and dimensions comparable to German and South African pebble-bed HTGR designs: nominally 500 μm in diameter and 9.6 wt.% 235U. Multiple kernel production batches were combined into the two composite lots used in the AGR-2 irradiation test (BWXT 2008a, 2008b). Lot G73I-14-69307 consisted of five batches of UCO fuel kernels, and Lot G73AA-10-69308 consisted of seven batches of UO_2 fuel kernels. TRISO coatings were applied to these kernels in multiple production batches using a fluidized-bed chemical-vapor-deposition system with an internal chamber diameter of 150 mm (Barnes and Marshall 2009). Two of these batches were selected for inclusion in the AGR-2 irradiation test after upgrading the size distribution of the particles via sieving at BWXT and additional roller micrometer sorting at Oak Ridge National Laboratory (ORNL), in which the latter was primarily performed to help reduce the defect fraction in the TRISO-coated particle batches prior to compacting (Appendix C in Hunn, Montgomery, and Pappano 2010a, 2010b). Batch G73J-14-93073A was the source of the particles used to produce the AGR-2 UCO compacts, and Batch G73H-10-93085B was the source of the particles in the AGR-2 UO_2 compacts." (Stempien et al., 2021).

In addition to the initial TRISO particle fabrication conditions, the compact fabrication conditions are also documented. As quoted from the AGR-2 TRISO Fuel Post-Irradiation Examination Final Report,

"The fuel particles were overcoated with a blend of 64 wt.% natural and 16 wt.% synthetic graphite flake that had been resinated with 20 wt.% of a phenolic thermoplastic resin and then pressed into cylindrical compacts (Pappano et al. 2008; Hunn, Montgomery, and Pappano 2010a, 2010b; Hunn 2010b). Based on the difference in the average diameter of the TRISO and overcoated particles, overcoat thickness was approximately 215 μm for production of the AGR-2 UCO fuel

and 390 μm for production of the AGR-2 UO_2 fuel, in which the required amount of resinated graphite overcoat was calculated to achieve the target uranium loading and matrix density. The presence of an applied overcoat promoted more-uniform fuel dispersion and minimized particle-to-particle contact compared to non-overcoating methods. The overcoated particles were uniaxially compacted in a heated double-acting die (65°C for UCO fuel and 75°C for UO_2 fuel). Prior to pressing each compact, additional resinated graphite was added to both ends of the die to form fuel-free end caps of graphitic matrix material with a typical thickness of less than 0.5 mm. These end caps provided smooth, protected surfaces to further minimize the chance of TRISO particle damage during handling. To carbonize the resin, the as-pressed compacts were gradually heated in flowing He at 350°C/h to 950°C and held there for 1 h. This was followed with a heat treatment at a peak temperature of 1800°C, which was primarily performed to help drive off possible impurities. The final UCO fuel compact lot (LEU09-OP2-Z) had an average volumetric packing fraction of 36.8% TRISO particles and 63.2% matrix. The matrix consisted of graphite flake dispersed in carbonized resin, with some preferential orientation of the graphite flake that was related to overcoating and pressing (Gerczak et al. 2021). The final UO_2 compact lot (LEU11-OP2-Z) had an average volumetric packing fraction of 23.5% TRISO particles and 76.5% matrix." (Stempien et al., 2021).

Of particular interest are the documented properties of the AGR-2 TRISO coating layers, as seen in Fig. 72. The irradiated micro-tensile samples for this dissertation were prepared from the coating layers of UCO fueled TRISO particle D42 housed at the IMCL at INL. The origin of TRISO particle D42 is unclear, but its fabrication conditions are assumed to be either similar or identical to the AGR-2 TRISO particles.

Table 1. Average kernel and TRISO coating properties for AGR-2 test fuel.

Property [a]	Specified Range for Mean Value	Measured Mean ± One Standard Deviation	
		AGR-2 UCO	AGR-2 UO_2
Kernel diameter before coating (μm)	415–435 (UCO) 490–510 (UO_2)	426.7 ± 8.8 (425.2–428.2)	507.7 ± 11.9 (505.7–509.7)
Buffer thickness (μm)	85–115	98.9 ± 8.4 (96.9–100.8)	97.7 ± 9.9 (94.8–100.5)
IPyC thickness (μm)	36–44	40.4 ± 2.5 (39.8–41.0)	41.9 ± 3.2 (41.0–42.8)
SiC thickness (μm)	32–38	35.2 ± 1.2 (34.9–35.5)	37.5 ± 1.2 (37.2–37.9)
OPyC thickness (μm)	36–44	43.4 ± 2.9 (42.8–44.1)	45.6 ± 2.4 (44.9–46.3)
Particle diameter [b] (μm)	not specified	873.2 ± 23 (872.3–874.0)	953.0 ± 28.5 (951.7–954.2)
Particle volume [b] (cm^3)	not specified	3.43E-4 [c]	4.45E-4 [c]
Kernel envelope density (Mg/m^3)	≥10.4	10.966 ± 0.033 [d] (10.944–10.988)	10.858 ± 0.082 [d] (10.80–10.91)
Buffer envelope density (Mg/m^3)	0.95–1.15	— [e]	0.99 [c]
IPyC sink/float density (Mg/m^3)	1.85–1.95	1.890 ± 0.014 (1.887–1.893)	— [e]
SiC sink/float density (Mg/m^3)	≥3.19	3.197 ± 0.002 (3.196–3.198)	3.200 ± 0.002 (3.199–3.201)
OPyC sink/float density (Mg/m^3)	1.85–1.95	1.907 ± 0.006 (1.905–1.909)	1.884 ± 0.005 (1.883–1.885)
IPyC anisotropy [b] (diattenuation)	≤0.0150	0.0116 ± 0.0004 [f] (0.0114–0.0119)	0.0111 ± 0.0009 [f] (0.0106–0.0117)
OPyC anisotropy [b] diattenuation)	≤0.0117	0.0088 ± 0.0004 [f] (0.0085–0.0090)	0.0073 ± 0.0004 [f] (0.0071–0.0075)

Values in parentheses are 95% confidence intervals for the mean and were calculated from the measured data using a Student's t-distribution and one-tail t-values.
a. Measurements performed at BWXT (BWXT 2008a, 2008b, 2008c, 2009), except where noted.
b. Measurements performed at ORNL (Hunn 2008, 2010a; Hunn, Montgomery and Pappano 2010a, 2010b; Hunn, Savage, and Silva 2010).
c. Average value was only measured on a single bulk sample, so no standard deviation or confidence interval can be determined.
d. Kernel density was measured on eight bulk samples, so standard deviation does not represent kernel-to-kernel variability.
e. Omitted density data were not available because hot sampling during each BWXT coating run only includes either buffer or IPyC.
f. Anisotropy is shown for as-fabricated TRISO particles; value increased 34–67% after compacting (Hunn, Savage, and Silva 2010).

Figure 72. Table of average kernel and TRISO coating properties for AGR-2 test fuel (Stempien et al., 2021).

3.24 TRISO Particle Micro-tensile Samples

The same pin stub and pin stub holder used for the baseline material micro-tensile fabrication process were employed for TRISO particle micro-tensile fabrication, with the addition of the TRISO particle epoxy resin compact being placed opposite of the pin stub set up. Molybdenum lift out grids were used because molybdenum is less ductile than copper and the grid posts are thinner than the silicon lift out grid posts. These two features allowed a firm base for

tensile testing and ease of fabrication and handling. The polished TRISO epoxy resin compact was placed at a height sufficient as to not have the pin stub set up crash into the SEM cone during tilting about eucentric height. This height is typically where the polished surface of the TRISO epoxy resin compact is near the highest point of the 45° pin stub holder. As this particular epoxy resin compact was nonconductive (no gold coating), copper tape was required to discharge any charge buildup accrued inside the vacuum chamber (Mauseth, 2021). An illustration of the pin stub and TRISO particle epoxy resin compact configuration, along with a wide view of the TRISO particles under an electron microscope, can be seen in Fig. 73.

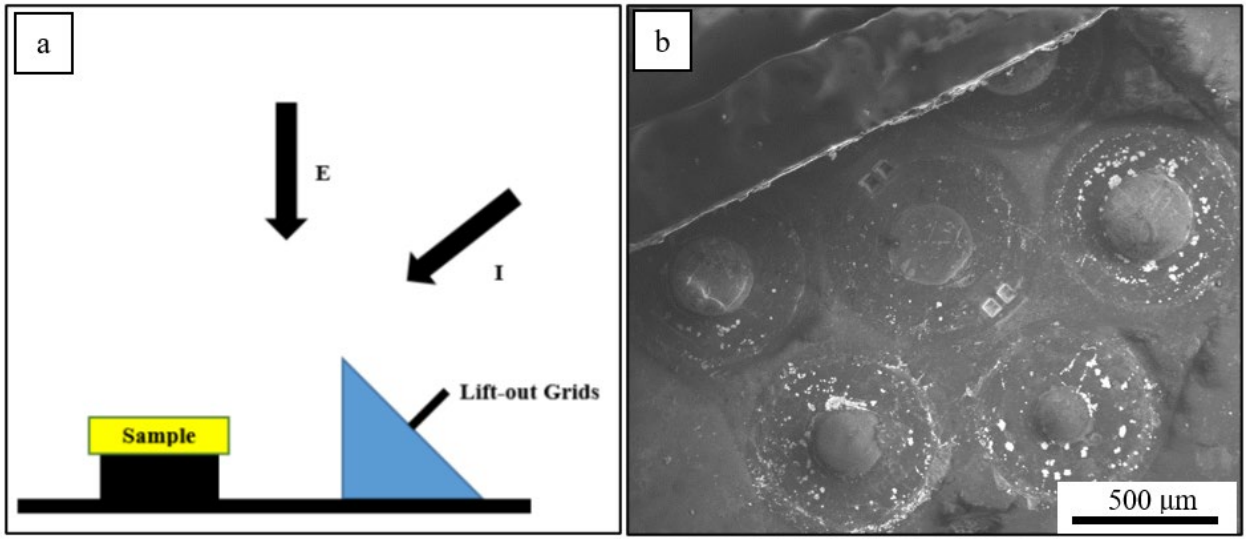

Figure 73. Image a) is an illustration of the TRISO micro-tensile fabrication configuration, where E represents the electron beam and I represents the ion beam. Image b) shows the TRISO particles at a low magnification (Mauseth, 2021).

Upon beginning micro-tensile fabrication inside the FIB dual beam chamber, the stage was brought to eucentric height and tilted to 52° to orthogonally aim the ion beam at the chosen location on the flat (0°), exposed TRISO particle cross section. From here, the first step in the milling process involved milling four trenches into the sample face to expose a 50 μm wide by 30 μm tall by 20 μm deep block, as can be seen in Fig. 74. As this was a rather large lift out block, a single

10 μm wide bridge was left in between the trenches to help support the block during the lift out process. To help expedite the trenching process, regular cross section patterns were used at the highest currents available (20 nA at Eames and 65 nA at CAES) (Mauseth et al., 2023).

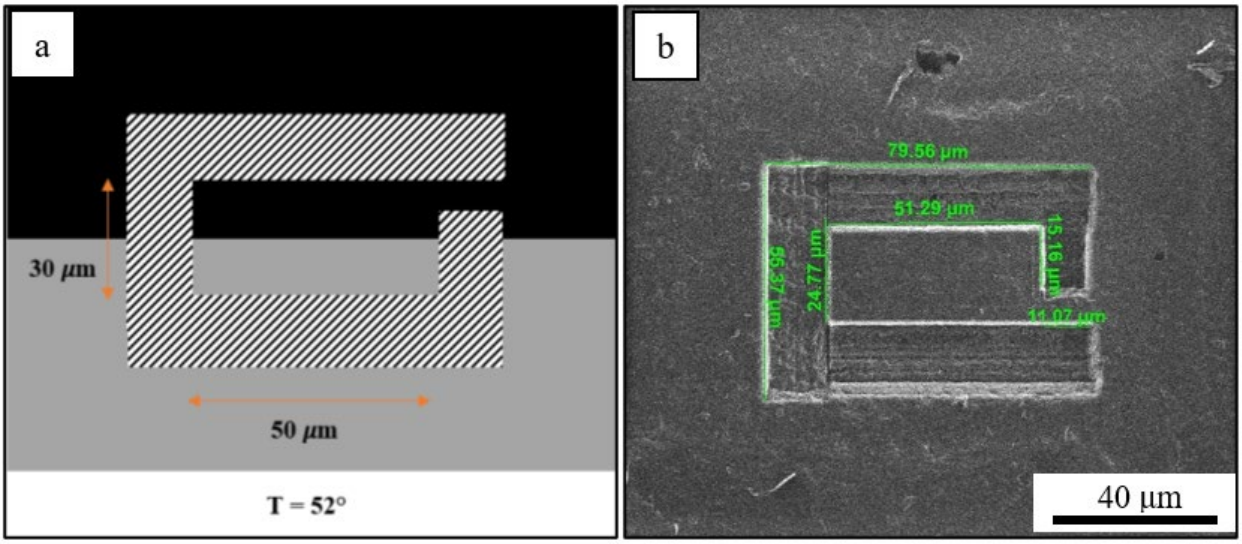

Figure 74. The illustration on top displays the dimensions of the exposed TRISO particle block and the four trench cuts from the perspective of the ion beam. The black background represents the IPyC layer and the gray background represents the buffer layer (Mauseth et al., 2023).

In the second step the stage was tilted to 0°, the ion beam was aimed at the bottom of the exposed block, and a 2 to 5 μm thick cut was milled all the way across and all the way through the bottom of the exposed block using the 15 nA aperture (if available) , as can be seen in Fig. 75. With one side of the block thoroughly milled, the stage was rotated 180° and the other side of the block was thoroughly milled (Mauseth, 2021).

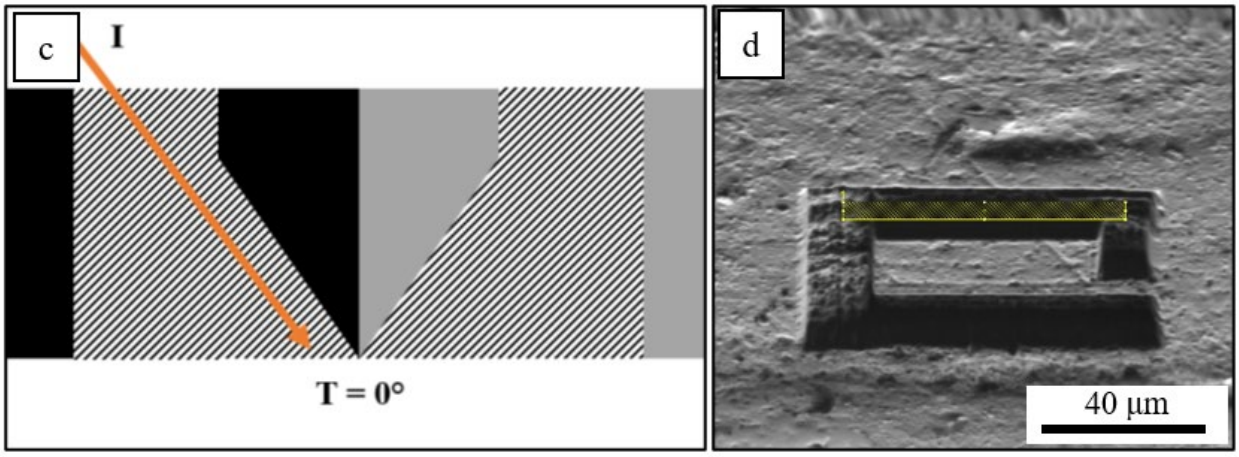

Figure 75. The illustration on bottom displays the side view perspective of the TRISO particle block undercuts. The black background represents the IPyC layer, the gray background represents the buffer layer, and the orange arrow represents the ion beam (Mauseth et al., 2023).

When the underside of the block was completely removed from the bulk sample (other than the bridge), the third milling step involved tilting the stage to 45° (to match the lift out grids), inserting the nano manipulator needle and GIS, and platinum welding the needle to the side of the block, as can be seen in Fig. 76. The bridge was cut, and the block lifted out of the bulk sample. After the block was lifted out and the GIS and nano manipulator needle were retracted, the stage was tilted back to 0°, rotated 180°, and aligned with the lift out grids on the pin stub assembly (Mauseth, 2021).

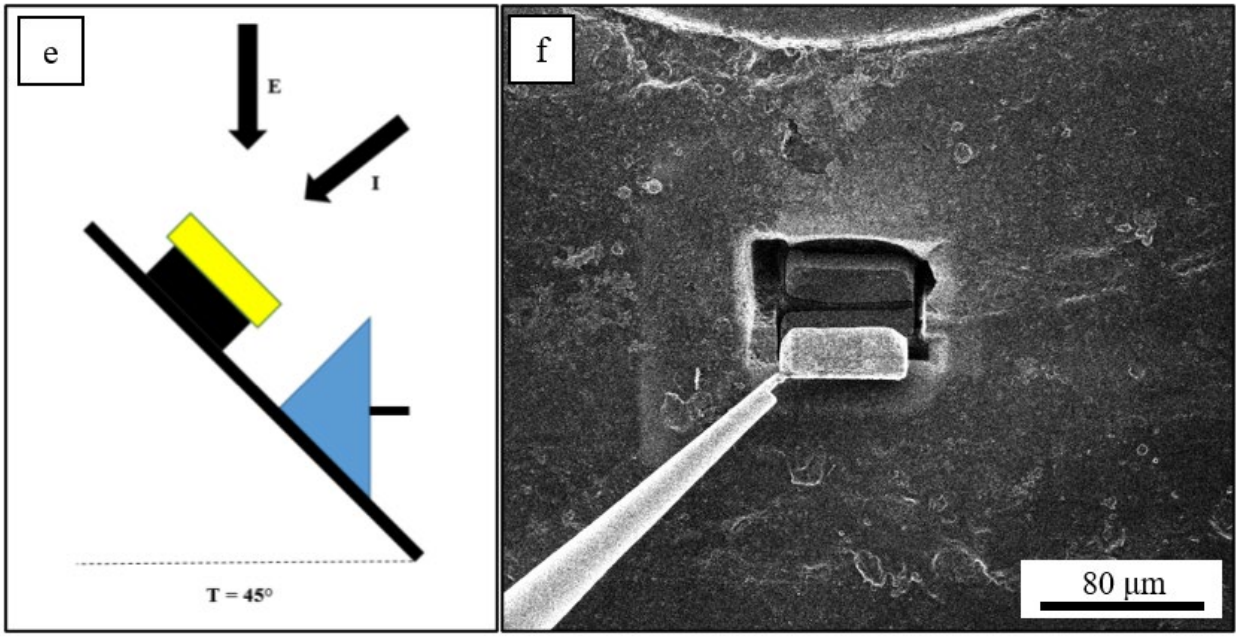

Figure 76. An illustration of the stage at 45 degrees in relation to the electron ion beams and an image of the TRISO particle block during step three. The nano-manipulator needle is marked with the blue arrow, platinum weld marked with the black arrow, and cut bridge marked with the yellow arrow (Mauseth et al., 2023).

The fourth step involved the nano manipulator needle with TRISO particle block attached and GIS being reinserted and used to carefully align and weld the lift out block onto the side of the molybdenum lift out grid posts, as can be seen in Fig. 77. After mounting, the nano manipulator needle was cut from the lift out block and the GIS and nano manipulator were retracted (Mauseth, 2021).

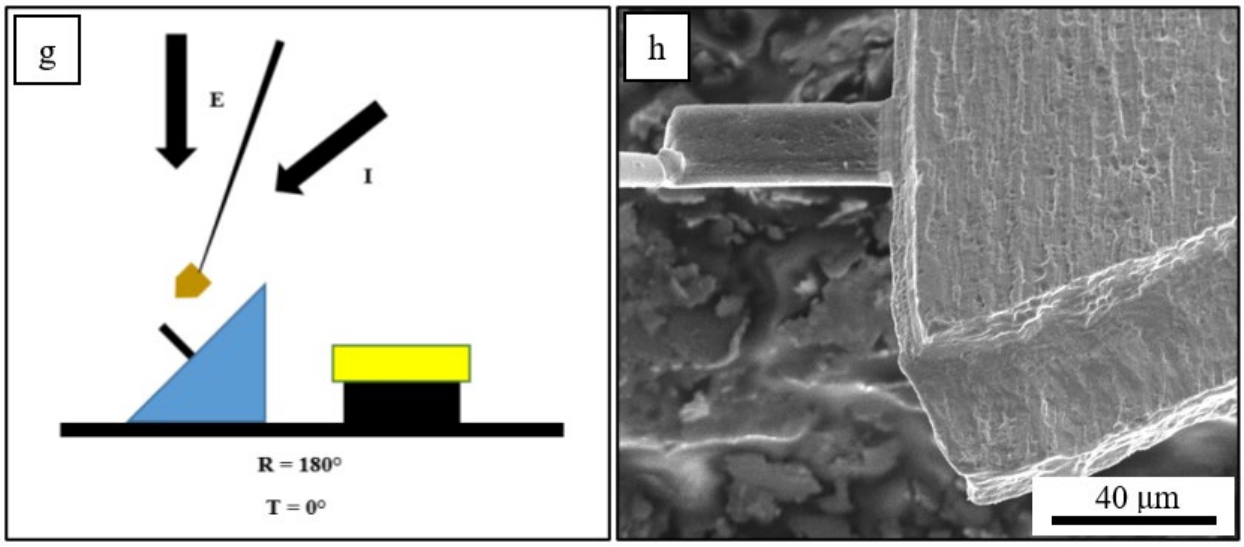

Figure 77. Illustrations and images of step five TRISO particle block mounting process. The nanomanipulator needle is marked by the blue arrows, the TRISO particle block marked by the orange arrows, the molybdenum lift-out grid marked by the green arrows, and the platinum weld marked by the white arrow (Mauseth et al., 2023).

In the fifth step of the milling process, the stage was rotated 180° and tilted 7° to align the side of the lift out block with the ion beam. The lift out block was thinned to 2 µm thick using a cleaning cross section at 15 nA, as can be seen in Fig. 78. After the thinning process, the stage was rotated 180° and the nano manipulator and GIS were reinserted (Mauseth, 2021).

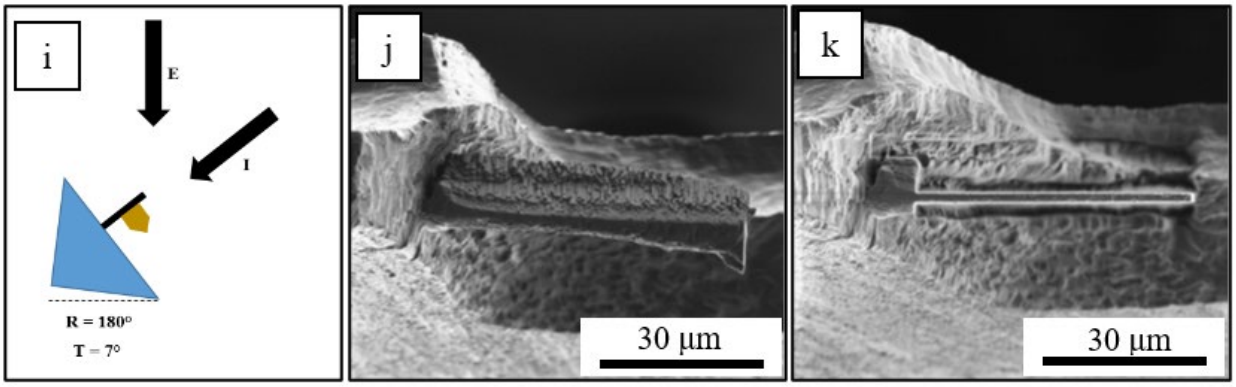

Figure 78. Illustrations and images of the step six TRISO particle block thinning process, with an illustration of the stage relative to the electron and ion beam shown on top, TRISO particle block shown on the left, and the thinned TRISO particle lamella shown on the right (Mauseth et al., 2023).

The sixth step in the TRISO micro-tensile fabrication process involved extracting individual lamella from the thinned lift out block. This was accomplished by welding the nano manipulator needle to the outside of the lift out block and milling 8 µm wide lamella from the block using the 1 nA aperture, as can be seen in Fig. 79. These lamellae were maneuvered to the tips of the molybdenum lift out grid posts and welded into premade notches. The lift out block was 50 µm wide and could accommodate up to five TRISO particle lamella pieces per lift out (Mauseth, 2021).

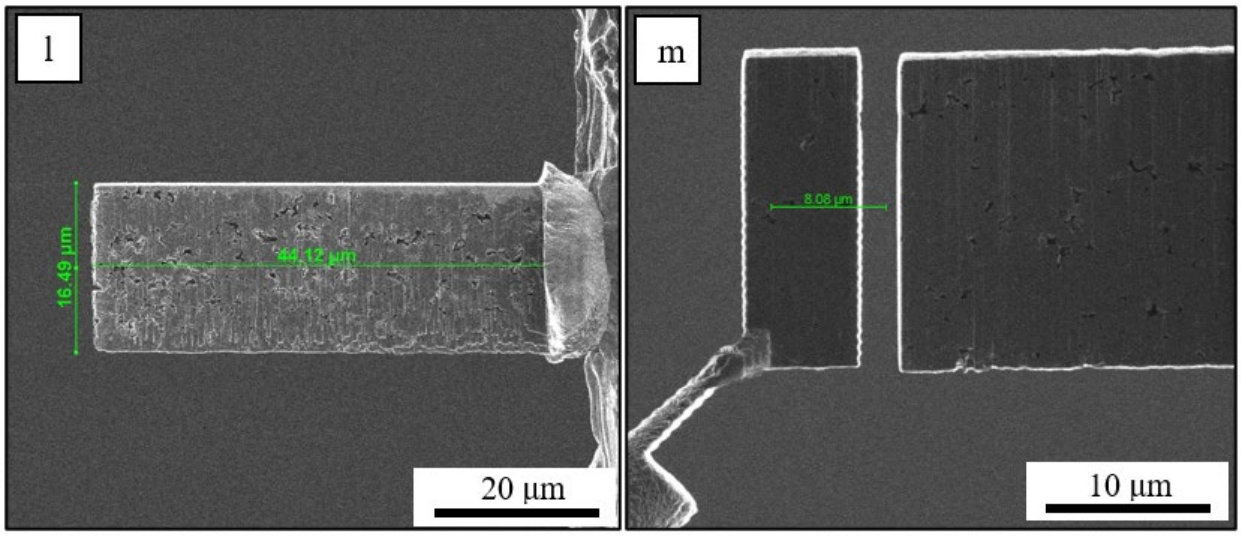

Figure 79. Images of the perpendicular view of the TRISO particle lamella and the notch used as a TRISO dog bone foothold, with the TRISO particle lamella on the left and the notch on the right. Image on the left displays the TRISO particle lamella piece being removed from the bulk TRISO particle lamella and the image on the right shows the TRISO particle lamella piece being the maneuvered over the molybdenum lift-out grid notch (Mauseth et al., 2023).

The seventh and final step in the TRISO particle micro-tensile fabrication process was forming the final tensile bar shape and applying an extra layer of platinum to the base of the micro-tensile samples for added security, as can be seen in Fig. 80. The tensile bar shape was formed by milling two parallel 3 μm wide by 6 μm tall cuts into the face of the mounted lamella using either 1 or 3 nA apertures. The final TRISO particle tensile bars were 15 μm tall, 8 μm wide, and 2 μm thick, with a tensile gauge section 6 μm tall by 2 μm wide and a bottom portion (head section) 4 μm tall. The true, as seen dimensions of the TRISO micro-tensile samples' gauge sections are listed in the results section (Mauseth, 2021).

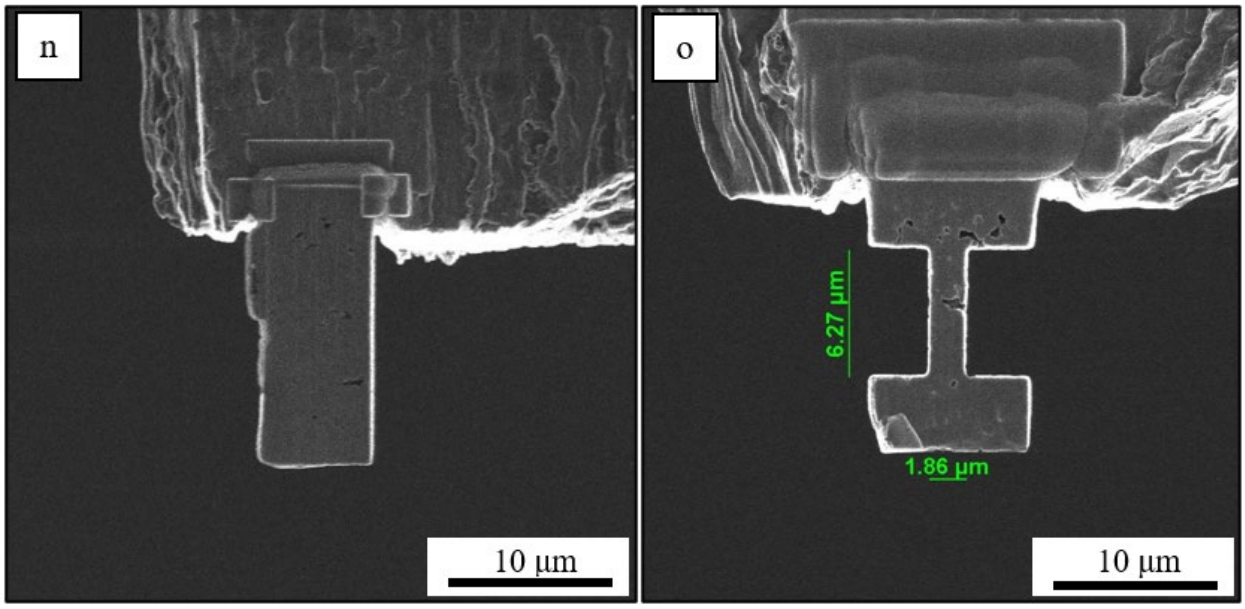

Figure 80. Image on left is the TRISO particle lamella piece platinum welded to the molybdenum lift-out grid post and the image on the right is of the completed TRISO particle dog bone (Mauseth et al., 2023).

The buffer and IPyC lift out blocks were extracted tangentially to each layer's respective centerline and the buffer-IPyC interlayer samples were extracted tangentially directly over the interlayer region, resulting in the layer interface line running orthogonally through the center of the gauge section of the micro-tensile samples. All final micro-tensile samples were extracted from approximately 10 µm deep into the surface of the TRISO particle due to the FIB polishing process in step five. Between the extraction depth, FIB polishing process, and mechanical polishing process used, it is believed no polishing damage was imparted to the samples (Mauseth et al., 2023). Increase in sample porosity due to milling was reduced by limiting ion beam exposure to the samples. When live imaging was required to position the Omniprobe nano manipulator for mounting and lift-outs, only the low energy aperture (30 pA) was used. When any other high energy aperture was used for positioning the ion image, only single snap shots were taken to ensure

limited exposure. Otherwise, the ion beams were only imparted onto the area that was being milled away (Giannuzzi Lucille A. and Prenitzer, 2005; Sakata et al., 1999).

3.3 Testing and Data Acquisition

3.31 Micro-tensile Testing

Tensile testing was conducted in a SEM using a PI 88 Picoindenter, which was programmed to pull, instead of push, to put the samples under tension. Tensile strength and strain were determined. To conduct the tests, the diamond gripper probe was attached to the transducer's threaded posts, ensuring that the black mark originally placed was still aligned properly. The 90° pin stubs containing the micro-tensile samples were then secured to the PI 88's sample mount. For added stability during the tensile tests, silver paint was added to the back of the lift out grids to connect them to the back stop of the 90° pin stub. With the PI 88 assembly inside the SEM chamber, the diamond gripper and the micro-tensile bars were aligned. As the transducer's threaded post had limited mobility, the PI 88's stage was primarily responsible for alignment. The micro-tensile samples were aligned with the inner cavity of the diamond gripper first by ensuring that the micro-tensile bars and diamond gripper were at different positions on the z axis. Having each constituent at different positions on the z axis ensured that the diamond gripper would not accidentally crash into the micro-tensile samples while maneuvering and enabled the user to tell whether the diamond gripper was above or below the micro-tensile samples. When the diamond gripper was aligned at a safe position on the z axis, the head of the micro-tensile samples were aligned with the inner cavity region of the diamond gripper in the xy plane. At that point, the diamond gripper could be raised or lowered to match its z position with that of the micro-tensile samples while simultaneously ensuring that it maintained proper xy plane alignment. A good indicator of close alignment between the diamond gripper and the micro-tensile samples was the

appearance of an electron shadow on the stationary component. Before initiating the test, an additional touch test was performed by very lightly (1 to 2 μN) pulling on the head of the micro-tensile samples in the y direction with the diamond gripper to ensure that the two constituents would be in contact during the tensile test. If there was no change in force reading during the touch test, the alignment needed to be adjusted. The tensile test was conducted with the initiation of a predesigned inverse load function created in the TriboScan software. The PI 88 was primarily designed to do indentation tests, so conducting tensile tests required switching the PI 88 into tensile mode in the TriboScan software to reverse the load function/create an inverse load function. The transducer was programmed to move the diamond gripper at 12 nm per second until fracture, at which point the load terminated. The 12 nm per second strain rate was derived by multiplying the as intended micro-tensile sample gauge height dimension of 6 μm by 0.002, following common practice (Kiener & Minor, 2011). Parts a) and b) of Fig. 81 the diamond gripper closing the distance on the micro-tensile samples whereas parts c) and d) show examples of micro-tensile samples after fracture (Mauseth, 2021).

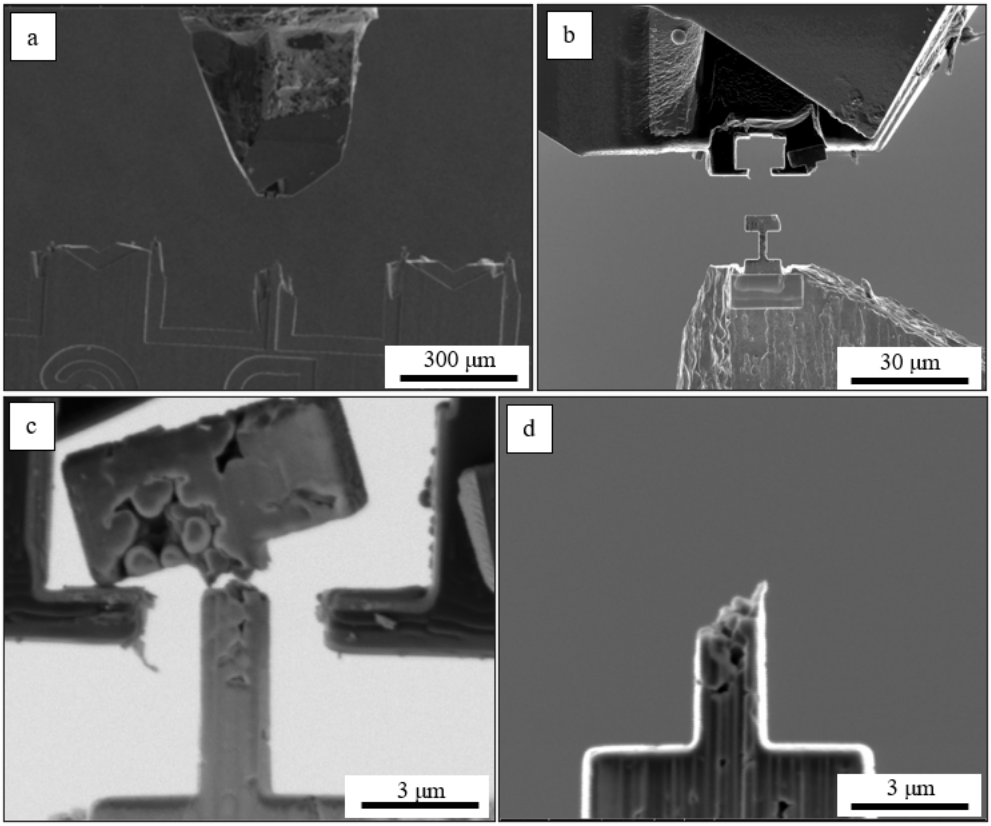

Figure 81. Image a) is a zoomed out view of a diamond gripper micro-tensile sample assembly, image b) is a closer view of a diamond gripper micro-tensile sample assembly, image c) displays a micro-tensile sample post fracture but with parts near diamond gripper, and image d) is of a micro-tensile sample post fracture where parts have disappeared (Mauseth et al., 2023).

4.0 Theory

4.1 Tensile Characteristics

While many mechanical characteristics of a material can be determined through tensile strength testing, for this dissertation we are primarily concerned with elastic deformation, uniform strain, total strain, yield strength, and ultimate tensile strength, with ultimate tensile strength being the most important. The ultimate tensile strength tells us how much force the specified regions can endure before failure/breaking (Dieter, 1961). In this specific case, the ultimate tensile strength of the buffer-IPyC interlayer region tells us the force required to initiate internal buffer tearing. This information can then be used for modeling the failure probability of TRISO particles layers. Values

for the properties of interest are obtained through knowing the engineering strain, engineering stress, true strain, and true stress quantities of the material. These quantities are found by obtaining the primary values of depth, load, cross sectional area, and height of the micro-tensile sample gauge section. Depth is the total elongation experienced by the gauge section during the tensile test and is paired with the starting height of the micro-tensile gauge section to determine strain. Load is the force detected by the PI 88 during the tensile test and is paired with the cross sectional area of the gauge section to determine stress parameters. The cross sectional area for all the micro-tensile samples was determined by multiplying values of width by the depth of the gauge section. To ensure the highest accuracy, SEM was used to capture images of both the face and underside of the finished micro-tensile samples. These images were analyzed with ImageJ software to determine the gauge dimensions (Mauseth et al., 2023). Using these parameters, engineering strain, engineering stress, true strain, and true stress can be defined. Engineering strain is defined as:

Equation 1. Engineering Strain

$$\boldsymbol{\varepsilon_{eng}} = \frac{\boldsymbol{\Delta L}}{\boldsymbol{L_0}} \quad [1]$$

with ΔL being the depth (current position minus original position) and L_0 being the original height of the tensile gauge section. Strain is unitless and is often expressed as a percentage. Strain is useful in that it determines how much a material has deformed and can be used to quantify ductile properties. Engineering stress is defined as:

Equation 2. Engineering Stress

$$\boldsymbol{\sigma_{eng}} = \frac{\boldsymbol{P}}{\boldsymbol{A_0}} \quad [2]$$

with P being the load and A_0 being the original cross sectional area. When using metric units, engineering stress is expressed as newtons per square meter, or pascals. True strain is defined as:

Equation 3. True Strain One

$$\boldsymbol{\varepsilon_{true} = ln\left(\frac{L}{L_0}\right)} \quad [3]$$

or

Equation 4. True Strain Two

$$\boldsymbol{\varepsilon_{true} = ln(1 + \varepsilon_{eng})} \quad [4]$$

with L being the present height of the tensile gauge section, L_0 being the original height of the tensile gauge section, and $\boldsymbol{\varepsilon}_{eng}$ being the engineering strain. True strain is meant to depict a more accurate measure of strain than engineering strain as it takes material deformation into account. While Equation 3 is the most direct way to calculate true strain, it requires specialized software to determine the variable L. Equation 4 predicts true strain using the already known engineering strain and can be used as a simpler alternative. True stress is defined as:

Equation 5. True Stress One

$$\boldsymbol{\sigma_{true} = \frac{P}{A}} \quad [5]$$

or

Equation 6. True Stress Two

$$\boldsymbol{\sigma_{true} = \sigma_{eng}(1 + \varepsilon_{eng})} \quad [6]$$

with P being the load, A being the present cross sectional area, $\boldsymbol{\sigma}_{eng}$ being the engineering stress, and $\boldsymbol{\varepsilon}_{eng}$ being the engineering strain. True stress is meant to depict a more accurate measure of stress than engineering stress because it measures the stress as the material is deforming and the cross sectional area is changing. While Equation 5 is the most direct way to calculate true stress, it is only useful if the changing cross sectional area can be measured during tensile testing. As this is incredibly difficult to measure, Equation 6 is a much more viable option. Equation 6 predicts true stress using the relationship between the already known engineering stress and engineering strain and is the method used in this dissertation. As the buffer layer material is porous, it should be mentioned that high porosity reduces the internal cross-sectional area of the stressed material. This leads to areas of higher stress concentrations (particularly around the pores) within the porous material in comparison to an equivalent bulk homogenous material. This ultimately results in lower engineering and true stresses observed in porous materials with the same gauge dimensions of bulk materials. The governing equations assume the external gauge dimensions are consistent between the porous and non-porous materials. By keeping the gauge dimensions consistent, the ultimate tensile strength can be determined for the different materials under the same external conditions (HASSELMAN, 1969; Mauseth et al., 2023).

From the derived engineering strain, engineering stress, true strain, and true stress quantities stress strain curves can be produced. Stress strain curves can be used to find the tensile characteristics of elastic deformation, uniform strain, total strain, yield strength, and ultimate tensile strength. Elastic deformation and yield strength are intrinsically intertwined, both being found by locating the intercept between the stress strain curve and a linear line with the same slope as the stress strain curve in the elastic region of the material. This linear line is typically offset by 0.002 or 0.2% of the strain. Elastic deformation and yield strength are important as they represent

the most extreme conditions a ductile material can withstand before permanent plastic deformation occurs. Uniform strain and ultimate tensile strength are also intrinsically intertwined, with ultimate tensile strength being the highest stress value experienced during the tensile test and uniform strain being its accompanying strain value. Ultimate tensile strength is the maximum stress a material can withstand. Total strain is defined as the strain measured at fracture. Uniform strain and total strain will differ in ductile materials due to the shape of the stress strain curve. However, for brittle materials (such as buffer and IPyC), total strain and uniform strain are synonymous due to abrupt fracture in brittle materials. For this reason, total strain and ultimate tensile strength are paired together in the results section for the TRISO particles. Parts a) and b) of Fig. 82 illustrate the characteristics and trends typically seen in stress strain curves (Mauseth, 2021).

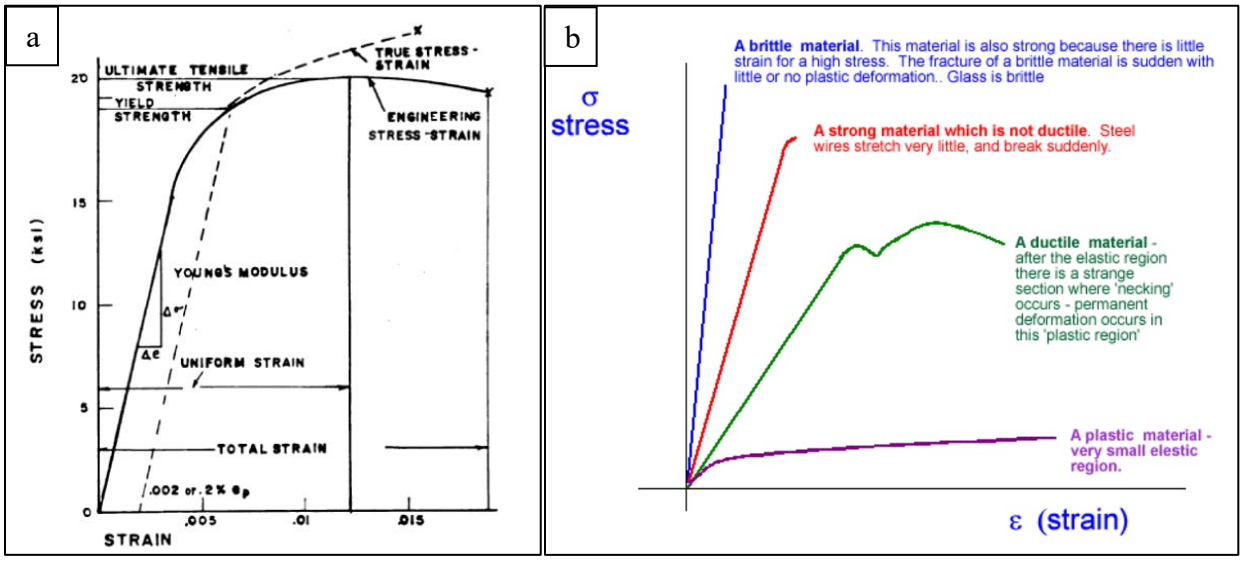

Figure 82. Image a) illustrates the individual tensile characteristics on a stress strain curve (Dieter, 1961) while image b) illustrates the differences between ductile and brittle materials on a stress strain graph (ÇAPAR, 2021).

As the materials tested during this dissertation were brittle and held varying levels of porosity, a mention on fracture mechanics is appropriate. It was postulated by Griffith that crack extension in brittle materials occurs when there is sufficient elastic strain energy in the vicinity of

a growing crack to form two new surfaces (Griffith, 1921). Irwin expanded on Griffith's work to show that crack extension is associated with an "energy release rate" (Irwin, 1956). This led to the development of fracture toughness, or resistance to crack growth. This approach enabled strength predictions based on fracture toughness that relate crack extension to the sizes of preexisting cracks or "flaws" within a material (Anderson, 1995). Fracture stress then can be defined as:

Equation 7. Fracture Stress

$$\boldsymbol{\sigma_F = \frac{K_{Ic}}{Y\sqrt{c}}} \quad [7]$$

where K_{Ic} is the fracture toughness, Y is the stress intensity shape factor (dimensionless, material-independent constant, related to the flaw shape, location, and stress configuration), and c is the flaw size. No material is perfectly homogenous, and all contain flaws on some scale. These flaws may be pores, distributed microcracks associated with grain boundaries or phase changes during processing, inclusions, regions of dislocations, or other possible variants and combinations (Quinn & Quinn, 2010). As can be seen in Equation 7, the larger the flaw size the lower the strength of the material. In relation to this dissertation, this means as the pore size of the layer or interlayer material increases, the strength of that layer or interlayer material decreases.

4.2 Digital Image Correlation (DIC)

Digital Image Correlation software, Shift DIC, was used to determine the accurate strain value for each of the micro-tensile samples. This software enables frame by frame tracking of individual points on the micro-tensile sample's SEM image during the tensile tests. Using the depth measurement from the PI 88's diamond gripper to calculate strain could lead to inaccuracies that were negated by using the software. For the tensile tests presented in this dissertation, the first step

in using DIC was determining in which frame the sample fractured. This determination allowed cropping of data after the point of fracture, the inclusion of which would negatively impact the accuracy of the stress strain curve. The next step was determining appropriate points to track on the micro-tensile samples. For accurate tracking, high contrast regions are desired. In this dissertation, the upper and lower corners between the gauge section and the head/base were chosen as the tracking points (two points total). These points were connected using the software and a raw engineering strain readout vs time was displayed. The raw DIC strain value at the point of fracture was used as the engineering total strain value seen in the TRISO particles' results section. While the raw DIC strain value is incredibly accurate at determining the total strain, it is not smooth and is insufficient for determining the shape of stress strain curves. The software provided multiple curve smoothing packages that could be applied to the raw strain time curve. For this dissertation, a Barlett curve with smoothing between 20% and 40% was chosen and applied to each of the micro-tensile sample's strain time curves to determine shape trends. It should be noted that the total strains derived from these smoothing curves should not be used as final total strain data as they are different from the raw total strain determined by DIC. Parts a) and b) of Fig. 83 show the tracking points connected before testing (black, no change) and immediately before fracture (blue, elongation) as seen in the Shift DIC software. Parts c) and d) show the dramatic difference between raw and smoothed strain time curves in Shift DIC software (Mauseth et al., 2023).

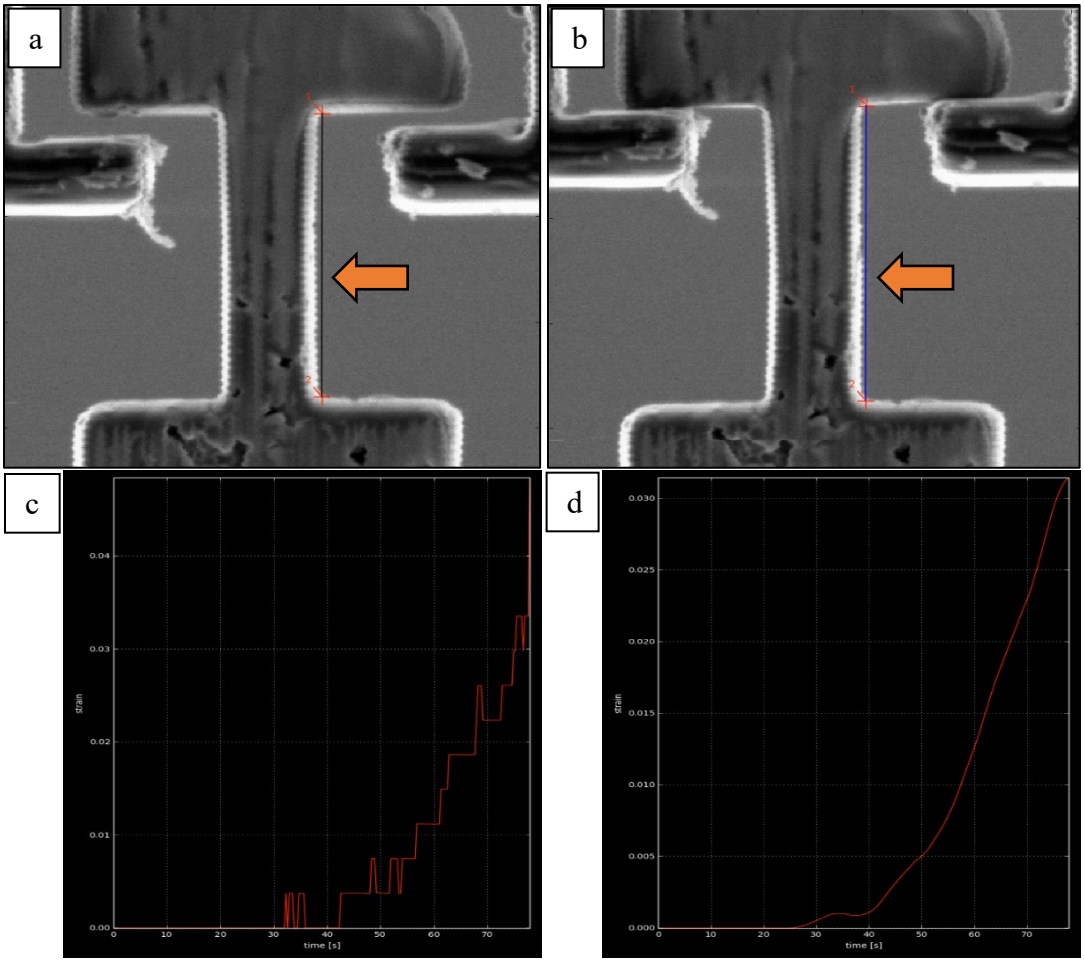

Figure 83. Images a) and b) demonstrate the difference in strain of a micro-tensile sample at different points during tensile testing, while images c) and d) demonstrate the difference between unsmoothed and smoothed strain time curves (Mauseth et al., 2023).

4.3 Statistics

4.31 Standard Statistics

While the number of samples tested in this dissertation were limited due to the time and cost of preparation and testing, statistics can and should still be applied. For normal/standard statistics, the standard mean, standard deviation, coefficient of variation, standard error, and confidence interval of the standard error of the mean (SEM) were used (Mauseth et al., 2023; Mohr et al., 2021). Standard mean is defined as:

Equation 8. Standard Mean

$$\bar{\bar{x}} = \frac{\sum x_i}{n} \quad [8]$$

where $\sum x_i$ is the sum of desired values and n is the number of values. While the mean is a very common and useful statistic in quantifying the properties of a sample group, it has limitations. In the case of small sample sizes, other standard statistics become important. Standard deviation is defined as:

Equation 9. Standard Deviation

$$\sigma = \sqrt{\frac{\sum(x_i - \bar{x})^2}{n}} \quad [9]$$

where x_i is the desired values, $\bar{x}$ is the standard mean, and n is the total number of values. The standard deviation indicates the spread of data relative to the mean. A high or low standard deviation is not necessarily bad but should be noted. The coefficient of variation is defined as:

Equation 10. Coefficient of Variation

$$CV = \frac{\sigma}{\bar{\bar{x}}} \quad [10]$$

where σ is the standard deviation and $\bar{x}$ the mean. The coefficient of variation is simply the ratio of the standard deviation to the mean and is another metric in assessing the variation in the sample group. Standard error is defined as:

Equation 11. Standard Error

$$SE = \frac{\sigma}{\sqrt{n}} \quad [11]$$

where σ is the standard deviation and n is the total number of values. The standard error is an indicator of the difference between population mean and sample mean. As the sample groups in this dissertation are small, standard error is important in the data analysis. The confidence interval SEM is defined as:

Equation 12. Confidence Interval SEM

$$\boldsymbol{CI = \bar{x} \pm z\frac{\sigma}{\sqrt{n}}} \quad [12]$$

where $\bar{x}$ is the standard mean, z is the confidence level value, and $\frac{\sigma}{\sqrt{n}}$ is the standard error. Assuming a normal distribution with a confidence of 95% (z value of 1.96), the population mean has a 95% chance of lying within 1.96 standard errors of the sample mean.

4.32 Weibull Statistics

Weibull statistics are powerful in that they can model many different types of distributions with a high level of accuracy, particularly skewed normal/Gaussian and Rayleigh distributions. The main reasons for applying Weibull statistics to the TRISO particles data are to determine the type and breadth of distributions for each material and to create the beginning of failure probability estimates. While the sample size of the TRISO particle micro-tensile samples is limited, it is still useful to apply Weibull statistics to reveal trends. For the TRISO particle data in this dissertation, a two parameter Weibull distribution through linear regression was created. The two parameters determined through linear regression were the Weibull modulus/shape and scale parameters. These two parameters were used to determine a host of other Weibull statistics, such as the Weibull mean, Weibull mode, Weibull median, Weibull variance, values for the Weibull probability density function (pdf), and values for the Weibull cumulative distribution function (cdf) and survival function (Rinne, 2008). The linear regression of our TRISO micro-tensile samples began by

assigning failure probability (F) values to each of the material's ultimate tensile strength values in ascending order (Mauseth et al., 2023). The F value can be defined as:

Equation 13. F Value

$$\boldsymbol{F = \frac{n_i - 0.5}{n}} \quad [13]$$

where n_i is the assigned number, n is the total number of samples, and 0.5 is used to center the data points among the data population and improve the failure probability analysis for small sample sizes. X and Y values that linearize the cumulative distribution function so that linear regression can reveal the shape and scale parameters were obtained. For the linear regression used in this dissertation, X could be defined as:

Equation 14. Linear Regression X

$$\boldsymbol{X = ln(x_i)} \quad [14]$$

where x_i is the ultimate tensile strength at a particular assigned number. Y could be defined as:

Equation 15. Linear Regression Y

$$\boldsymbol{Y = ln\left(ln\left(\frac{1}{1 - F_i}\right)\right)} \quad [15]$$

where F_i is the F value at a particular assigned number. The shape parameter, β, is defined as the slope of the linear regression line of the X and Y values and the intercept, b, is the y intercept. The scale parameter is defined as:

Equation 16. Scale Parameter

$$\boldsymbol{\eta = \exp\left(\frac{-b}{\beta}\right)} \quad [16]$$

To verify the accuracy of the linear regression, R^2, standard error of regression, and P Value tests were applied using their respective Microsoft Excel functions (RSQ, STEYX, and T.TEST) (see the results section.) The shape and scale parameters were used to determine the remainder of Weibull statistics. The Weibull probability density function (pdf) is defined as:

Equation 17. Weibull Probability Density Function

$$\boldsymbol{f(x) = \frac{\beta}{\eta}\left(\frac{x}{\eta}\right)^{\beta-1} \exp\left(-\left(\frac{x}{\eta}\right)^{\beta}\right)} \quad [17]$$

The Weibull probability density function is driven by the shape and scale parameters and assigns a probability to every ultimate tensile strength value seen on the Weibull distribution. The Weibull mean is defined as:

Equation 18. Weibull Mean

$$\boldsymbol{\overline{T} = \eta * \Gamma\left(\frac{1}{\beta} + 1\right)} \quad [18]$$

The Weibull mean can be compared with the standard mean and is another indicator of the accuracy of the Weibull distribution. The Weibull variance is defined as:

Equation 19. Weibull Variance

$$\boldsymbol{\sigma_T = \eta\sqrt{\Gamma\left(\frac{2}{\beta} + 1\right) - \Gamma\left(\frac{1}{\beta} + 1\right)^2}} \quad [19]$$

The Weibull variance is synonymous with the standard deviation of the Weibull distribution and can be compared to the standard deviation obtained through standard statistics. The Weibull mode is defined as:

Equation 20. Weibull Mode

$$\widetilde{\boldsymbol{T}} = \boldsymbol{\eta}\left(\mathbf{1} - \frac{\mathbf{1}}{\boldsymbol{\beta}}\right)^{\frac{\mathbf{1}}{\boldsymbol{\beta}}} \quad [20]$$

The Weibull mode is the ultimate tensile strength value with the highest probability in the Weibull probability density function and is displayed visually as the peak of the Weibull distribution. The Weibull cumulative distribution function (cdf) is defined as:

Equation 21. Weibull Cumulative Distribution Function

$$\boldsymbol{F(x)} = \mathbf{1} - \mathbf{exp}\left(-\left(\frac{\boldsymbol{x}}{\boldsymbol{\eta}}\right)^{\boldsymbol{\beta}}\right) \quad [21]$$

The Weibull cumulative distribution function defines the percentage of the population that likely would have failed at a given ultimate tensile stress value. The Weibull survival function (i.e. reliability function) is defined as:

Equation 22. Weibull Survival Function

$$\boldsymbol{S(x)} = \mathbf{1} - \boldsymbol{F(x)} \quad [22]$$

The Weibull survival function is the opposite of the Weibull cumulative distribution function as it defines the percentage of the population that likely would have "survived" to a given ultimate tensile stress and is one of the metrics graphed in the results section of this dissertation. The Weibull median is defined as:

Equation 23. Weibull Median

$$\breve{T} = \eta\left(ln(2)\right)^{\frac{1}{\beta}} \quad [23]$$

The Weibull median marks the ultimate tensile stress at which 50% of the population has failed/survived according to the cumulative distribution and survival functions.

An important attribute of Weibull statistics is how the Weibull modulus/shape parameter β is influential in the Weibull probability distribution function's ability to model many different types of distributions with a high level of accuracy and the affect it has on the relationship between the mean, median, and mode of the distribution. Three types of distributions are of particular interest for this dissertation: the positively/right skewed distribution, symmetric/normal distribution, and negatively/left skewed distribution. When the Weibull modulus/shape parameter β is between 1 and 2.6, a positively/right skewed distribution is formed. The Rayleigh or Chi-square distribution lies within this range and is defined as when the Weibull modulus/shape parameter β is 2. Positively/right skewed distributions tend to arise when there is a lower bound, and most values are relatively close to the lower bound. Values cannot be less than this bound but can appear far from the peak on the high end, causing the distribution to skew positively (Rinne, 2008). For this dissertation, the lower bound is zero since the ultimate tensile strength cannot be lower than zero MPa. When the Weibull modulus/shape parameter β is near 3, a symmetric/normal distribution is approximated. Symmetric/normal distributions contain values that are far away from any bounds present and extreme values appear in equal amounts on either side of the distribution peak. Standard statistics are based off of an assumed normal distribution, hence why Weibull statistics are needed in this dissertation to evaluate the distributions varying away from a normal distribution. When the Weibull modulus/shape parameter β is above 3.7, a negatively/left skewed

distribution is formed. Negatively/left skewed distributions tend to arise when there is an upper bound, and most values are relatively close to the upper bound. Values cannot exceed this bound but can appear far from the peak on the low end, causing the distribution to skew negatively (Rinne, 2008). For this dissertation, the upper bound is the theoretical maximum ultimate tensile strength of the material, which for reference PyC material should be ~1.60 ± 0.55 GPa (X. Zhang et al., 2019). Furthermore, the higher the Weibull modulus/shape parameter β is the narrower the probability curve of the strength distribution is near the upper strength bound. This is indicative that the material is more consistent (homogeneous) with more uniform defects more evenly distributed throughout the material (Rinne, 2008). The shape of the distribution directly affects the relationship between the mean, median, and mode of the distribution. For symmetric/normal distributions, the mean, median, and mode are equal (Fig. 84a). However, for positively/right skewed distributions the mean is greater than the median and overestimates the most common values while for negatively/left skewed distributions the mean is less than the median and underestimates the most common values (Fig. 84b and 84c). Due to the mean over and underestimating the most frequently occurring values in asymmetric distributions, the mean should be used with caution during analysis. Instead, the median should be the primary metric for ultimate tensile strength as the median is a more robust statistic in the presence of extreme values (Rinne, 2008).

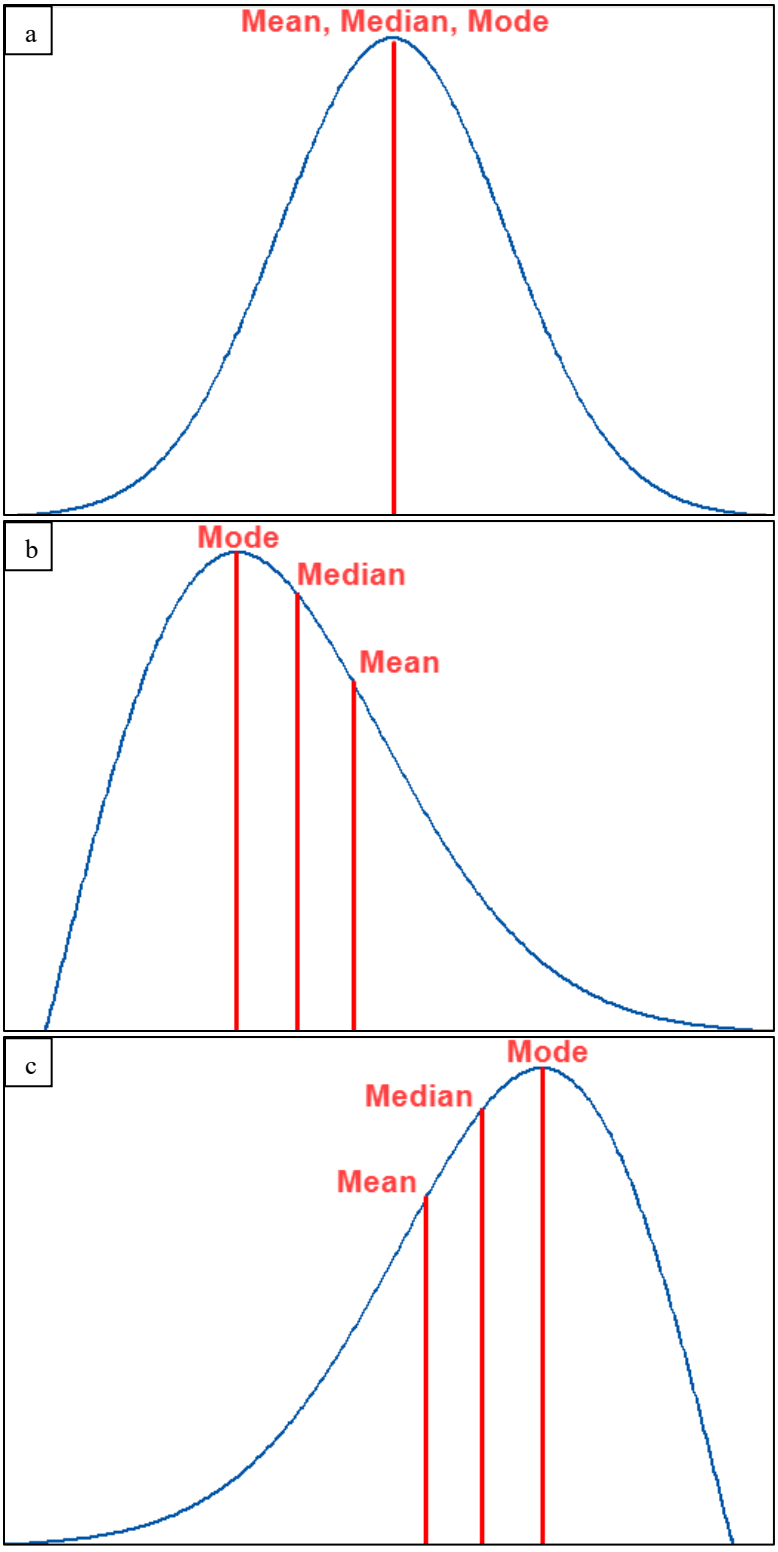

Figure 84. Graphs depicting the relative positions between the mean, median, and mode for a a) symmetric/normal distribution, b) positively/right skewed distribution, and c) negatively/left skewed distribution (Skewed Distribution: Definition & Examples - Statistics By Jim, n.d.).

5.0 Results

5.1 Baseline Material Micro-tensile Characteristics

Copper, molybdenum, and silicon micro-tensile samples were used as the baseline materials for establishing the viability of the sample preparation and testing techniques. Copper represents a ductile material, molybdenum a stronger material, and silicon a brittle material. The baseline materials were meant to be a proof of concept of the testing technique on materials readily found in the literature. If experimental results were comparable to those reported in the literature then confidence in the testing technique could carry over to the untested TRISO particles. Of the ten copper micro-tensile samples made, seven produced viable stress strain curves, with viable samples referring to samples that underwent testing without significant errors. These errors include bent/damaged samples, plasticity without fracture, fracture far outside the gauge section, etc. Of the ten molybdenum micro-tensile samples made, only two survived with the rest being damaged during handling. Of those two samples, only one produced a viable stress strain curve. Of the eight silicon micro-tensile samples made, five produced viable stress strain curves. With limited literature on Molybdenum's micro-tensile strength and this dissertation not producing a large enough silicon sample size to make a useful comparison, copper was chosen as the comparison material because sufficient samples were produced to make an appropriate comparison to literature. Fig. 85 displays select stress strain curves from the copper, molybdenum, and silicon micro-tensile samples (Mauseth, 2021; Mauseth et al., 2023).

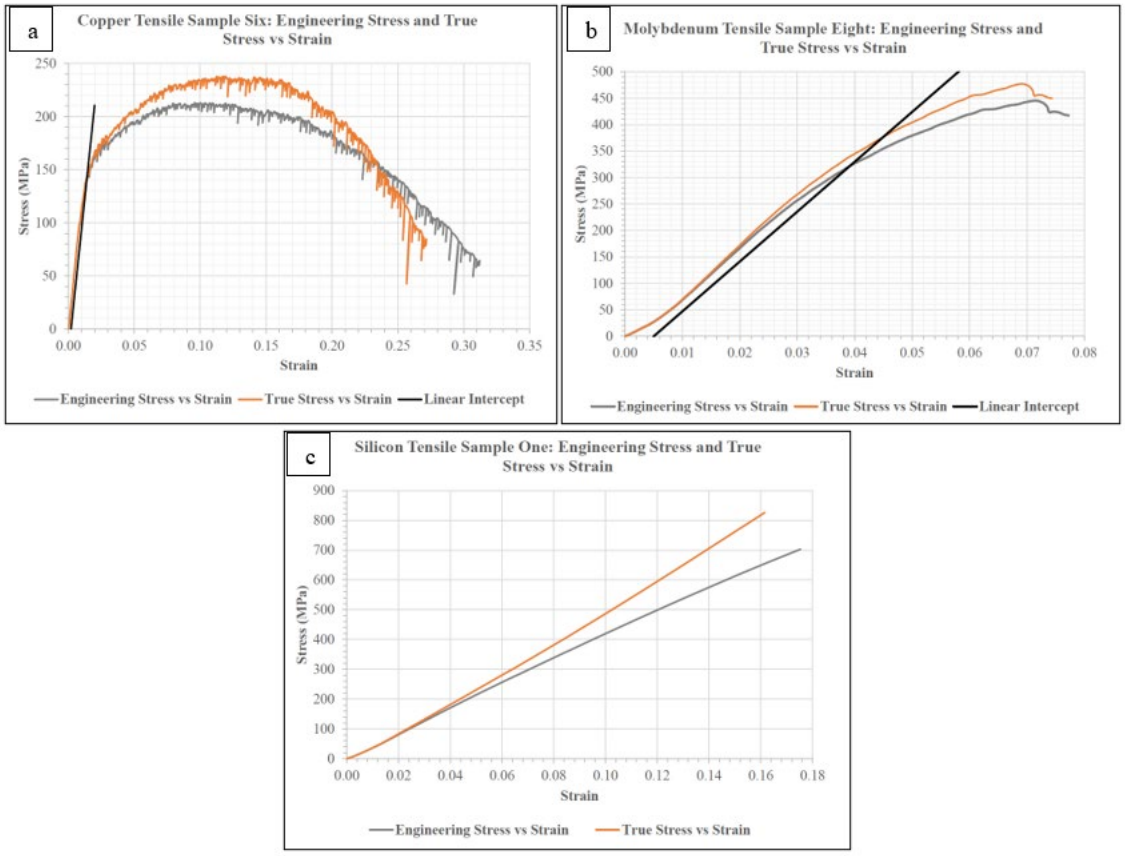

Figure 85. Graphs a) stress strain curve of copper tensile sample six with associated linear intercept line, b) stress strain curve of molybdenum tensile sample eight with associated linear intercept line, and c) stress strain curve of silicon tensile sample one (Mauseth, 2021). Notice the ductile material, strong material, and brittle material stress strain curve shapes.

The gauge dimensions, true yield strength, and ultimate tensile strength of the copper samples were compared with the same parameters found from the Copper Development Association (Copper Developement Association Inc., 2021), and Kiener and Minor nano crystalline samples (Kiener & Minor, 2011) (see Table I). A graphic comparison of values from Kiener and Minor and this dissertation is shown in Fig. 86.

Table I. Copper Gauge Section Comparison

Copper Gauge Section Comparison					
Sample Name	Height (μm)	Width (μm)	Depth (μm)	True Yield Strength (MPa)	True Ultimate Tensile Strength (MPa)
Copper 02	9.10	1.60	1.70	144.10	203.71
Copper 04	8.70	1.40	1.30	334.39	376.76
Copper 05	8.40	1.60	2.30	188.85	215.80
Copper 06	9.30	1.80	1.90	145.38	237.99
Copper 07	8.90	1.80	2.30	196.80	223.91
Copper 09	9.80	1.90	2.40	210.38	227.73
Copper 10	9.00	1.00	2.40	210.63	247.28
Copper Samples Standard Mean	9.03	1.59	2.04	204.36	247.60
Copper Development Association (Cold Rolled Copper)	Macroscopic (>1000 μm)	Macroscopic (>1000 μm)	Macroscopic (>1000 μm)	138 min.	221 min.
Kiener and Minor (nano crystalline)		.15	.15	636	

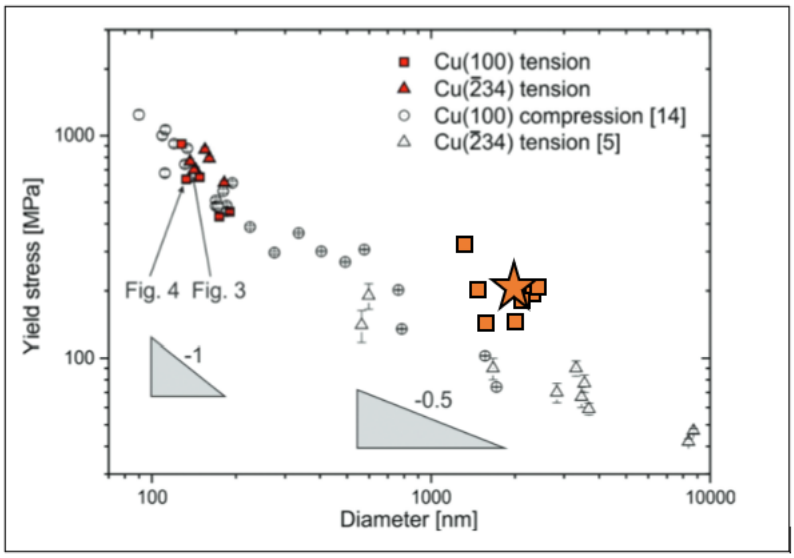

Figure 86. Yield stress vs diameter of nano tensile, nano compression, and micro-tensile strengths of copper tensile samples from Kiener and Minor (Kiener & Minor, 2011). The copper micro-tensile samples used in this dissertation presented in this paper had diameters ranging from 1000 to 3000 nm and an average yield strength of 204 MPa. The average yield strength is plotted as an orange star while the individual yield strengths are plotted as orange squares on a plot of the data from Kiener and Minor (Mauseth et al., 2023).

5.2 TRISO Particle Micro-tensile Characteristics

The gauge dimensions, detected load at fracture, engineering total strain, true total strain, and true ultimate tensile strength were obtained for each of the surrogate fueled, unirradiated fueled, and irradiated fueled TRISO particle buffer, IPyC, and buffer-IPyC interlayer micro-tensile samples. For standard statistics, the standard mean, standard deviation, coefficient of variation, standard error, and 95% confidence interval were determined for each of the samples (Tables II, IV, and VI). Graphs of true total strain, ultimate tensile strength, and true total strain versus ultimate tensile strength illustrate data spread (Fig. 88, 91, and 94). For Weibull statistics, the F values, X and Y linear regression values, shape parameter, intercept, scale parameter, R2, standard error of regression, P value, Weibull mean, Weibull mode, Weibull median, and Weibull variance were determined for each of the samples (Tables III, V, and VII). Plots of the Weibull probability density functions and survival functions can be seen in Fig. 89, 92, and 95. As mentioned in section

3.24, the buffer and IPyC samples were drawn radio-centrically (the middle/center) from within their respective layers and the buffer-IPyC interlayer samples were drawn from directly over the interfacial region, with the interface line running directly through the center of the gauge section of the micro-tensile samples. All samples were drawn from approximately 10 μm deep into the sample. All samples were drawn from individual TRISO particles (either from the same surrogate, unirradiated, or irradiated TRISO particle). It should be noted that there appear to be large variations in the mechanical properties of the tested materials. There are two main reasons for these variations. The first is the difference in porosity from sample to sample, which in turn directly impacts the observed stress due to internal differences in cross sectional area. This porosity difference could be due to the material in this dissertation being relatively heterogenous/inconsistent or to localized size effects due to the porosity of the material and size of the tensile gauge section. Conducting a tensile gauge size sensitivity analysis would either confirm or denounce the existence of these localized size effects (Carpinteri & Ferro, 1994; Karnati et al., 2022; Leguillon & Piat, 2008). The second reason for the spread in the results is that brittle materials (such as silicon and the tested IPyC/Buffer samples) possess strength distributions that are highly probabilistic in nature because their strength is highly dependent on flaw distributions within the material (Karnati et al., 2022). This second reason is why Weibull statistics were used for data analysis, in addition to standard statistics. It should also be noted that while the 95% confidence interval is useful for normal distributions, it does not accurately represent skewed distributions. However, seeing that the 95% confidence interval is unsuitable for skewed distributions should help the reader to realize why doing a Weibull analysis is important and why standard statistics is not enough for analyzing skewed distributions (Lu et al., 2002).

5.21 Surrogate Fueled TRISO Particles

Five buffer, eleven buffer-IPyC interlayer, and four IPyC micro-tensile samples from the surrogate fueled TRISO particle were tested for this dissertation. Select stress strain curves from the buffer (a), IPyC (b), and buffer-IPyC interlayer (c)(d) regions that highlight the unique stress strain curve shapes for each region are shown in Fig. 87.

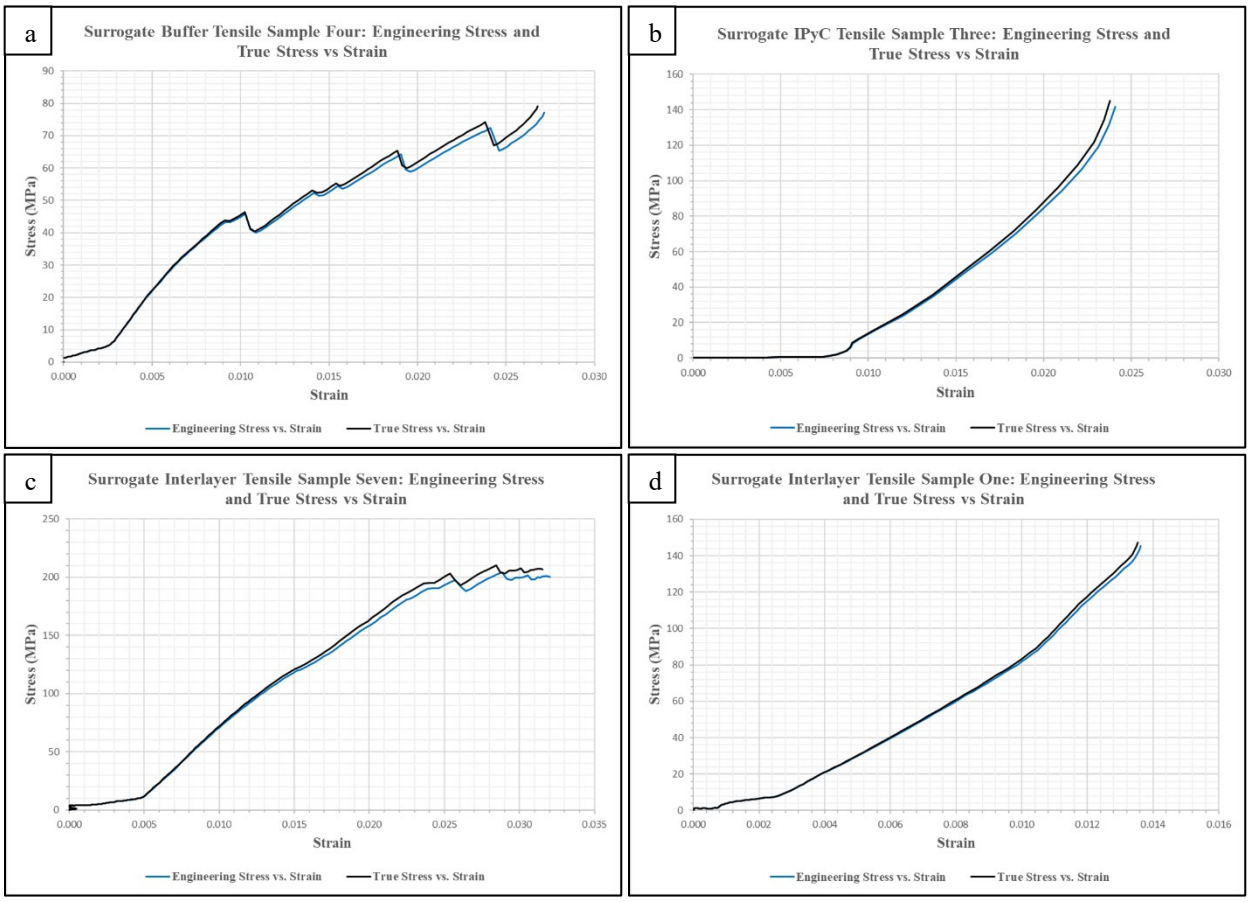

Figure 87. Graphs a) displays "rippling" as seen in the stress strain curve of surrogate buffer tensile sample four, b) displays sharp and abrupt fracture commonly seen in brittle materials as seen in the stress strain curve of surrogate IPyC tensile sample three, and c) and d) display both behaviors as seen in surrogate interlayer tensile samples seven and one (Mauseth et al., 2023).

Table II. Surrogate Fueled TRISO Particle Gauge Section Standard Statistics

Surrogate Fueled TRISO Particle Gauge Section Standard Statistics							
Sample Name	Height (μm)	Width (μm)	Depth (μm)	Detected Load at Fracture (μN)	Engineering Total Strain	True Total Strain	True Ultimate Tensile Strength (MPa)
Buffer 01	6.16	2.25	2.23	516.91	0.028	0.028	105.71
Buffer 02	6.30	2.01	2.33	764.39	0.027	0.026	168.15
Buffer 03	6.16	2.07	2.32	846.48	0.015	0.015	179.45
Buffer 04	6.08	2.09	2.36	369.62	0.041	0.040	77.90
Buffer 05	6.19	1.82	2.33	676.16	0.015	0.015	162.30
Interlayer 01	6.08	2.00	1.80	416.36	0.015	0.015	117.73
Interlayer 02	6.12	2.03	1.83	197.04	0.023	0.023	54.33
Interlayer 03	6.08	2.06	1.89	1113.30	0.019	0.019	290.75
Interlayer 04	6.12	2.05	2.01	196.34	0.045	0.044	49.86
Interlayer 05	6.16	2.06	1.87	520.87	0.048	0.047	142.35
Interlayer 06	6.26	1.91	0.95	254.34	0.026	0.026	144.40
Interlayer 07	6.19	2.00	0.79	367.64	0.024	0.024	237.95
Interlayer 08	6.19	1.95	0.98	219.00	0.018	0.017	116.38
Interlayer 09	6.27	2.01	0.96	349.28	0.026	0.026	186.74
Interlayer 10	6.41	1.84	1.02	521.39	0.026	0.026	286.74
Interlayer 11	8.50	2.00	2.00	513.26	0.017	0.017	130.54
IPyC 02	6.12	2.44	1.94	1322.95	0.062	0.060	297.68
IPyC 03	6.16	2.43	1.91	645.86	0.039	0.038	144.26
IPyC 04	6.05	2.43	1.98	675.22	0.053	0.051	147.35
IPyC 05	6.12	2.28	1.97	741.71	0.029	0.028	169.66
Buffer Standard Mean	6.18	2.05	2.31	-	0.025	0.025	138.70
Interlayer Standard Mean	6.40	1.99	1.46	-	0.026	0.026	159.80
IPyC Standard Mean	6.11	2.40	1.95	-	0.046	0.044	189.74
Buffer Standard Deviation	-	-	-	-	0.011	0.010	44.36
Interlayer Standard Deviation	-	-	-	-	0.011	0.011	82.68
IPyC Standard Deviation	-	-	-	-	0.015	0.014	72.85
Buffer Coefficient of Variation	-	-	-	-	0.42	0.41	0.32
Interlayer Coefficient of Variation	-	-	-	-	0.42	0.41	0.52
IPyC Coefficient of Variation	-	-	-	-	0.32	0.32	0.38
Buffer Standard Error	-	-	-	-	0.005	0.005	19.84
Interlayer Standard Error	-	-	-	-	0.003	0.003	24.93
IPyC Standard Error	-	-	-	-	0.007	0.007	36.42
Buffer 95% Confidence Interval SEM	-	-	-	-	0.016, 0.035	0.016, 0.034	99.82, 177.58
Interlayer 95% Confidence Interval SEM	-	-	-	-	0.020, 0.033	0.020, 0.032	110.94, 208.66
IPyC 95% Confidence Interval SEM	-	-	-	-	0.031, 0.060	0.031, 0.058	118.35, 261.13

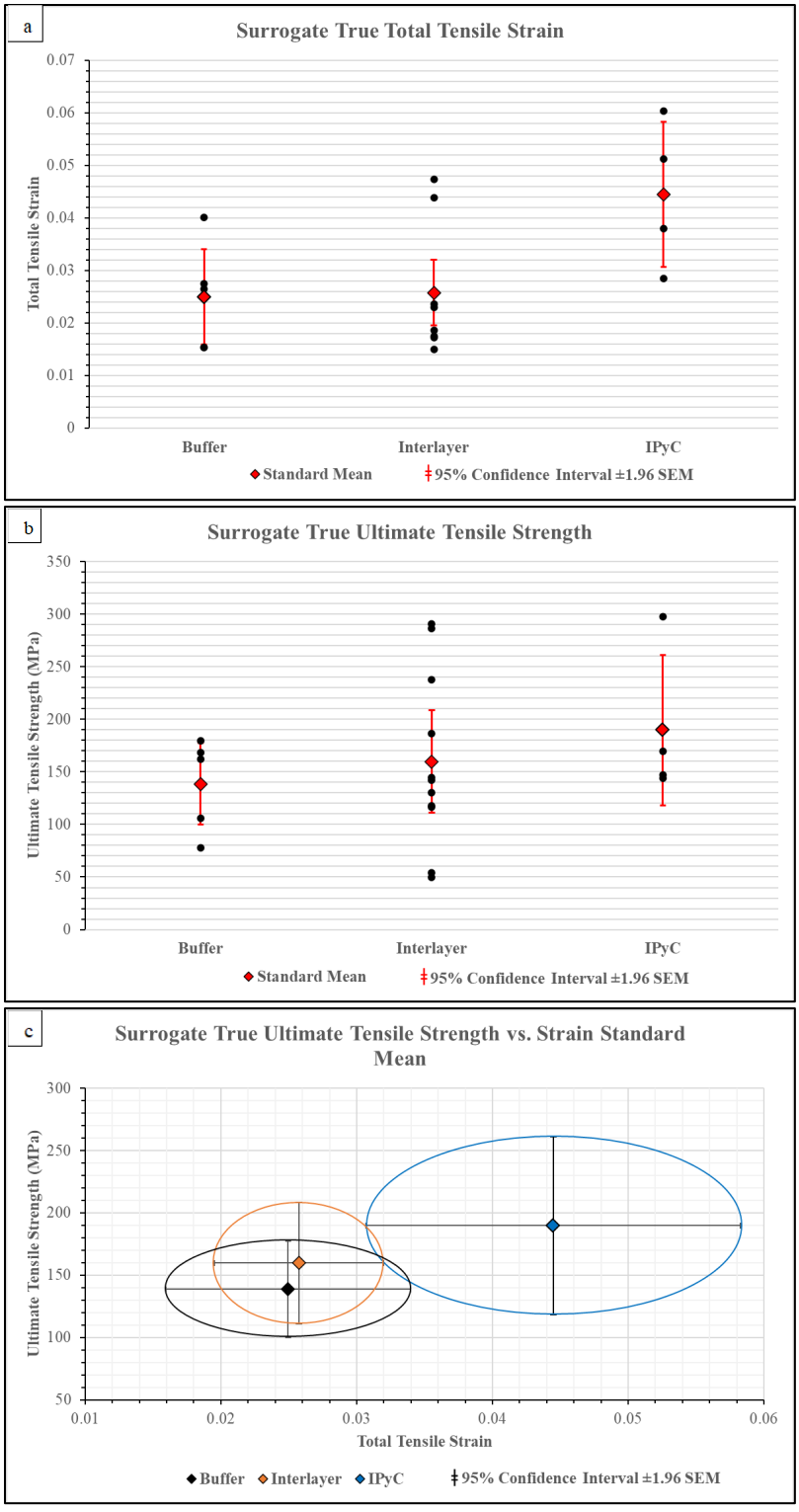

Figure 88. Graphs a) true total strain values for each of the surrogate particle regions micro-tensile samples along with 95% confidence interval, b) true ultimate tensile strength values along with 95% confidence interval, and c) the mean true total strain versus ultimate tensile strength with 95% confidence interval (Mauseth et al., 2023).

Table III. Surrogate Fueled TRISO Particle Weibull Statistics

Weibull Linear Regression Values				
Buffer True Strength (MPa)	Assigned Number	F	"X" ln(Strength at Failure)	"Y" ln(ln(1/(1-F)))
77.90	1	0.10	4.36	-2.25
105.71	2	0.30	4.66	-1.03
162.30	3	0.50	5.09	-0.37
168.15	4	0.70	5.12	0.19
179.45	5	0.90	5.19	0.83
Interlayer True Strength (MPa)				
49.86	1	0.05	3.91	-3.07
54.33	2	0.14	4.00	-1.92
116.38	3	0.23	4.76	-1.36
117.73	4	0.32	4.77	-0.96
130.54	5	0.41	4.87	-0.64
142.35	6	0.50	4.96	-0.37
144.40	7	0.59	4.97	-0.11
186.74	8	0.68	5.23	0.14
237.95	9	0.77	5.47	0.39
286.74	10	0.86	5.66	0.69
290.75	11	0.95	5.67	1.13
IPyC True Strength (MPa)				
144.26	1	0.13	4.97	-2.01
147.35	2	0.38	4.99	-0.76
169.66	3	0.63	5.13	-0.02
297.68	4	0.88	5.70	0.73

Two Parameter Weibull Distribution Values			
Parameter/Value	Buffer	Interlayer	IPyC
Shape Parameter, β	3.14	2.02	2.83
Scale Parameter, η	156.22	182.52	217.06
Intercept	-15.88	-10.51	-15.22
R^2	0.92	0.94	0.67
Standard Error of Regression	0.38	0.32	0.82
P-Value	1.37E-04	1.10E-10	1.10E-03
Weibull Mean (MPa)	139.80	161.73	193.36
Weibull Mode (MPa)	138.31	130.07	186.06
Weibull Median (MPa)	139.03	152.22	190.69
Weibull Variance (MPa)	48.72	83.84	74.05

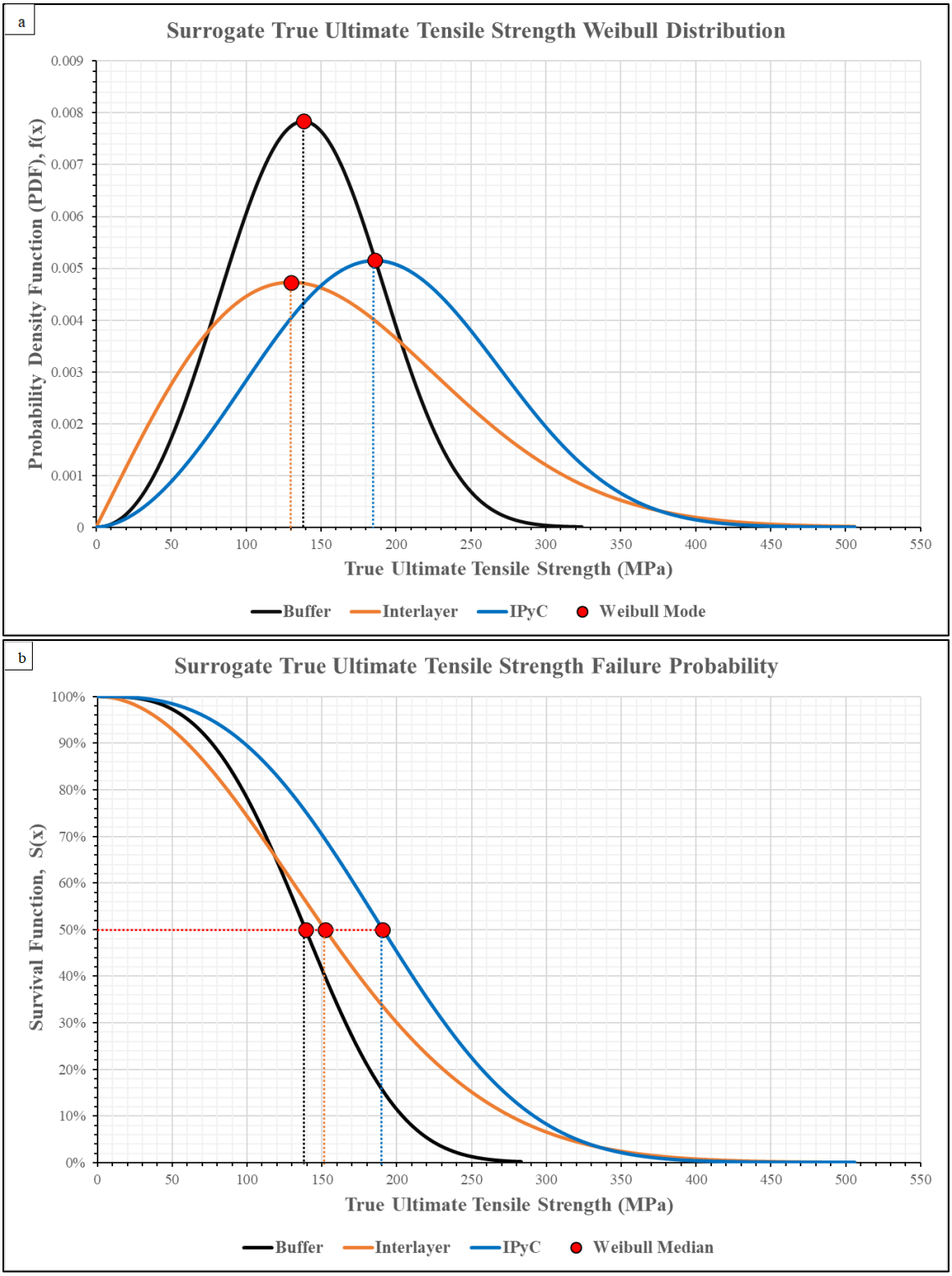

Figure 89. Graphs a) of the Weibull probability function versus ultimate tensile strength with associated Weibull modes and b) the Weibull survival function with associated Weibull medians for each of the surrogate particle regions (Mauseth et al., 2023).

5.22 Unirradiated Fueled TRISO Particles

Four buffer, twelve buffer-IPyC interlayer, and four IPyC micro-tensile samples from the unirradiated fueled TRISO particle were tested during this dissertation. Select stress strain curves from the buffer (a), IPyC (b), and buffer-IPyC interlayer (c)(d) regions that highlight the unique stress strain curve shapes for each region are shown in Fig. 90.

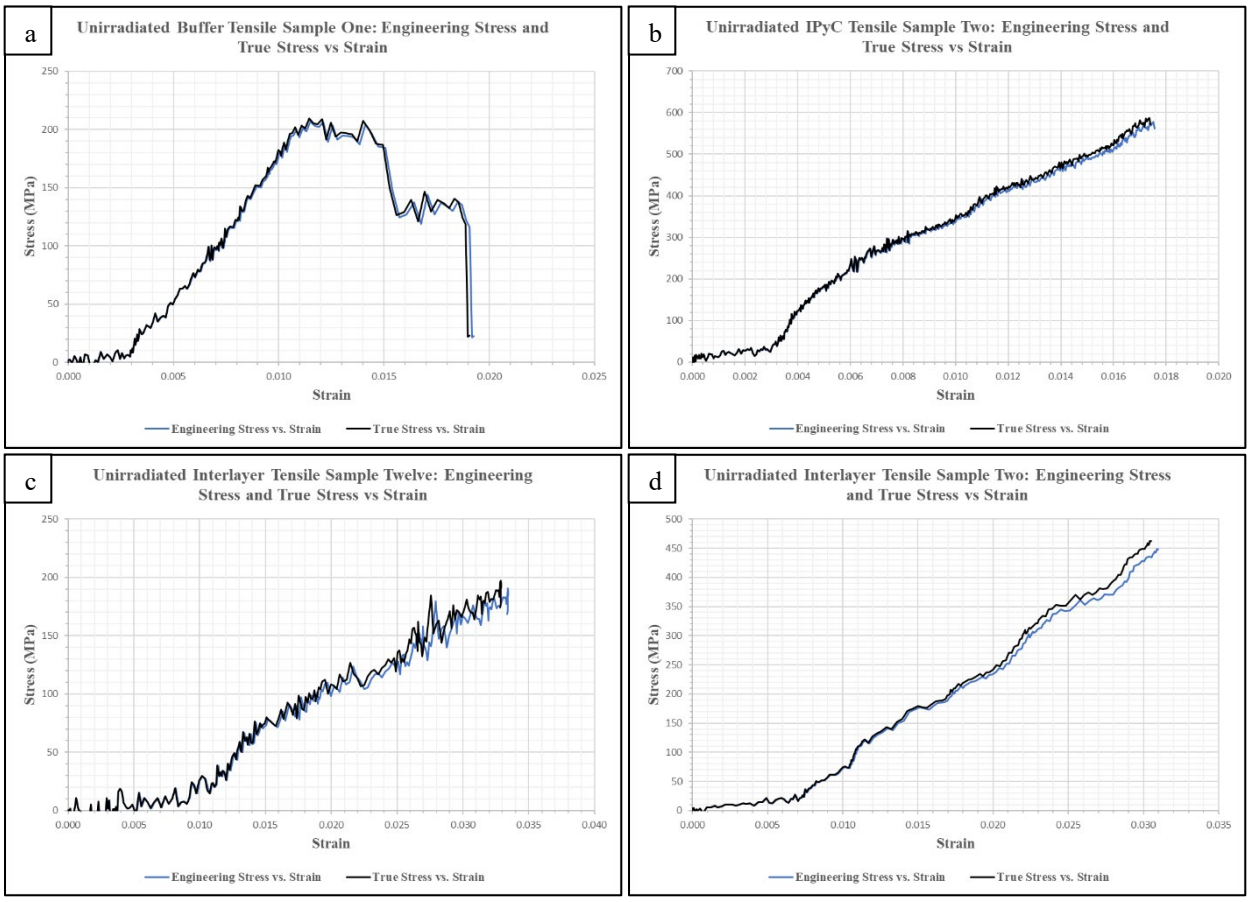

Figure 90. Graphs a) displays "rippling" as seen in the stress strain curve of unirradiated buffer tensile sample one, b) displays sharp and abrupt fracture commonly seen in brittle materials as seen in the stress strain curve of unirradiated IPyC tensile sample three, and c) and d) display both behaviors as seen in unirradiated interlayer tensile samples twelve and two.

Table IV. Unirradiated Fueled TRISO Particle Gauge Section Standard Statistics

Unirradiated Fueled TRISO Particle Gauge Section Standard Statistics							
Sample Name	Height (μm)	Width (μm)	Depth (μm)	Detected Load at Fracture (μN)	Engineering Total Strain	True Total Strain	True Ultimate Tensile Strength (MPa)
Buffer 01	6.26	2.18	1.59	713.50	0.012	0.011	209.26
Buffer 02	6.24	3.21	1.26	706.25	0.009	0.009	175.44
Buffer 03	6.52	2.65	1.30	670.16	0.007	0.007	196.02
Buffer 04	7.49	1.94	1.31	627.14	0.023	0.023	252.86
Interlayer 01	6.21	2.27	1.15	739.66	0.016	0.015	289.25
Interlayer 02	6.25	2.21	1.18	1163.03	0.031	0.030	462.58
Interlayer 03	6.22	2.40	1.06	984.07	0.041	0.040	404.54
Interlayer 04	6.21	2.18	0.97	774.90	0.021	0.021	373.82
Interlayer 05	6.15	2.25	1.36	1314.68	0.029	0.028	443.53
Interlayer 06	6.36	2.48	1.23	1191.82	0.033	0.033	404.23
Interlayer 07	6.29	2.37	1.09	1326.16	0.019	0.019	524.99
Interlayer 08	6.34	2.23	1.12	792.84	0.026	0.025	324.97
Interlayer 09	6.28	2.19	1.36	683.26	0.018	0.018	234.00
Interlayer 10	6.50	2.17	1.29	763.58	0.020	0.019	278.21
Interlayer 11	6.10	1.52	1.22	452.68	0.030	0.030	252.35
Interlayer 12	6.14	1.52	1.23	356.16	0.033	0.033	196.88
IPyC 01	6.24	2.46	1.10	1378.78	0.017	0.017	521.17
IPyC 02	6.29	2.37	0.97	1331.69	0.018	0.017	587.23
IPyC 04	6.21	2.30	1.07	1137.87	0.015	0.015	468.75
IPyC 05	6.29	2.35	1.34	1391.94	0.014	0.014	449.89
Buffer Standard Mean	6.63	2.50	1.36	-	0.013	0.013	208.39
Interlayer Standard Mean	6.26	2.15	1.19	-	0.026	0.026	349.11
IPyC Standard Mean	6.26	2.37	1.12	-	0.016	0.016	506.76
Buffer Standard Deviation	-	-	-	-	0.007	0.007	32.75
Interlayer Standard Deviation	-	-	-	-	0.008	0.008	101.99
IPyC Standard Deviation	-	-	-	-	0.001	0.001	61.54
Buffer Coefficient of Variation	-	-	-	-	0.56	0.56	0.16
Interlayer Coefficient of Variation	-	-	-	-	0.30	0.29	0.29
IPyC Coefficient of Variation	-	-	-	-	0.09	0.09	0.12
Buffer Standard Error	-	-	-	-	0.004	0.004	16.38
Interlayer Standard Error	-	-	-	-	0.002	0.002	29.44
IPyC Standard Error	-	-	-	-	0.001	0.001	30.77
Buffer 95% Confidence Interval SEM	-	-	-	-	0.006, 0.020	0.006, 0.019	176.30, 240.49
Interlayer 95% Confidence Interval SEM	-	-	-	-	0.022, 0.031	0.022, 0.030	291.40, 406.82
IPyC 95% Confidence Interval SEM	-	-	-	-	0.015, 0.018	0.015, 0.017	446.45, 567.07

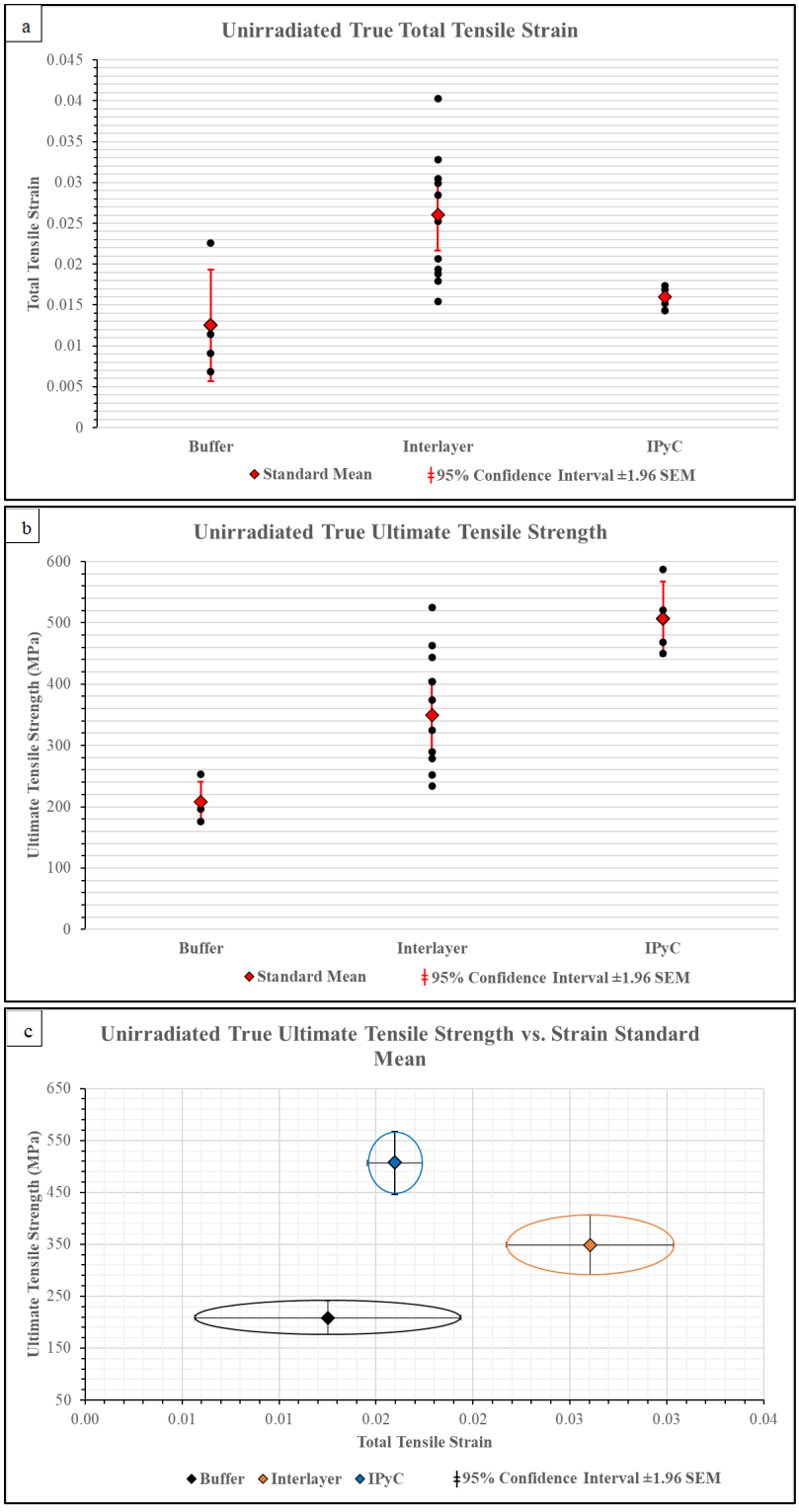

Figure 91. Graphs a) true total strain values for each of the unirradiated particle regions micro-tensile samples along with 95% confidence interval, b) true ultimate tensile strength values along with 95% confidence interval, and c) the mean true total strain versus ultimate tensile strength with 95% confidence interval.

Table V. Unirradiated Fueled TRISO Particle Weibull Statistics

Weibull Linear Regression Values				
Buffer True Strength (MPa)	Assigned Number	F	"X" ln(Strength at Failure)	"Y" ln(ln(1/(1-F)))
175.44	1	0.13	5.17	-2.01
196.02	2	0.38	5.28	-0.76
209.26	3	0.63	5.34	-0.02
252.86	4	0.88	5.53	0.73
Interlayer True Strength (MPa)				
196.88	1	0.04	5.28	-3.16
234.00	2	0.13	5.46	-2.01
252.35	3	0.21	5.53	-1.45
278.21	4	0.29	5.63	-1.06
289.25	5	0.38	5.67	-0.76
324.97	6	0.46	5.78	-0.49
373.82	7	0.54	5.92	-0.25
404.23	8	0.63	6.00	-0.02
404.54	9	0.71	6.00	0.21
443.53	10	0.79	6.09	0.45
462.58	11	0.88	6.14	0.73
524.99	12	0.96	6.26	1.16
IPyC True Strength (MPa)				
449.89	1	0.13	6.11	-2.01
468.75	2	0.38	6.15	-0.76
521.17	3	0.63	6.26	-0.02
587.23	4	0.88	6.38	0.73

Two Parameter Weibull Distribution Values			
Parameter/Value	Buffer	Interlayer	IPyC
Shape Parameter, β	7.32	3.96	9.26
Scale Parameter, η	221.56	385.36	532.80
Intercept	-39.53	-23.60	-58.13
R^2	0.92	0.96	0.89
Standard Error of Regression	0.40	0.26	0.47
P-Value	1.44E-03	3.10E-10	1.04E-03
Weibull Mean (MPa)	207.73	349.11	505.19
Weibull Mode (MPa)	217.16	358.11	526.27
Weibull Median (MPa)	210.74	351.33	512.12
Weibull Variance (MPa)	33.49	98.75	65.35

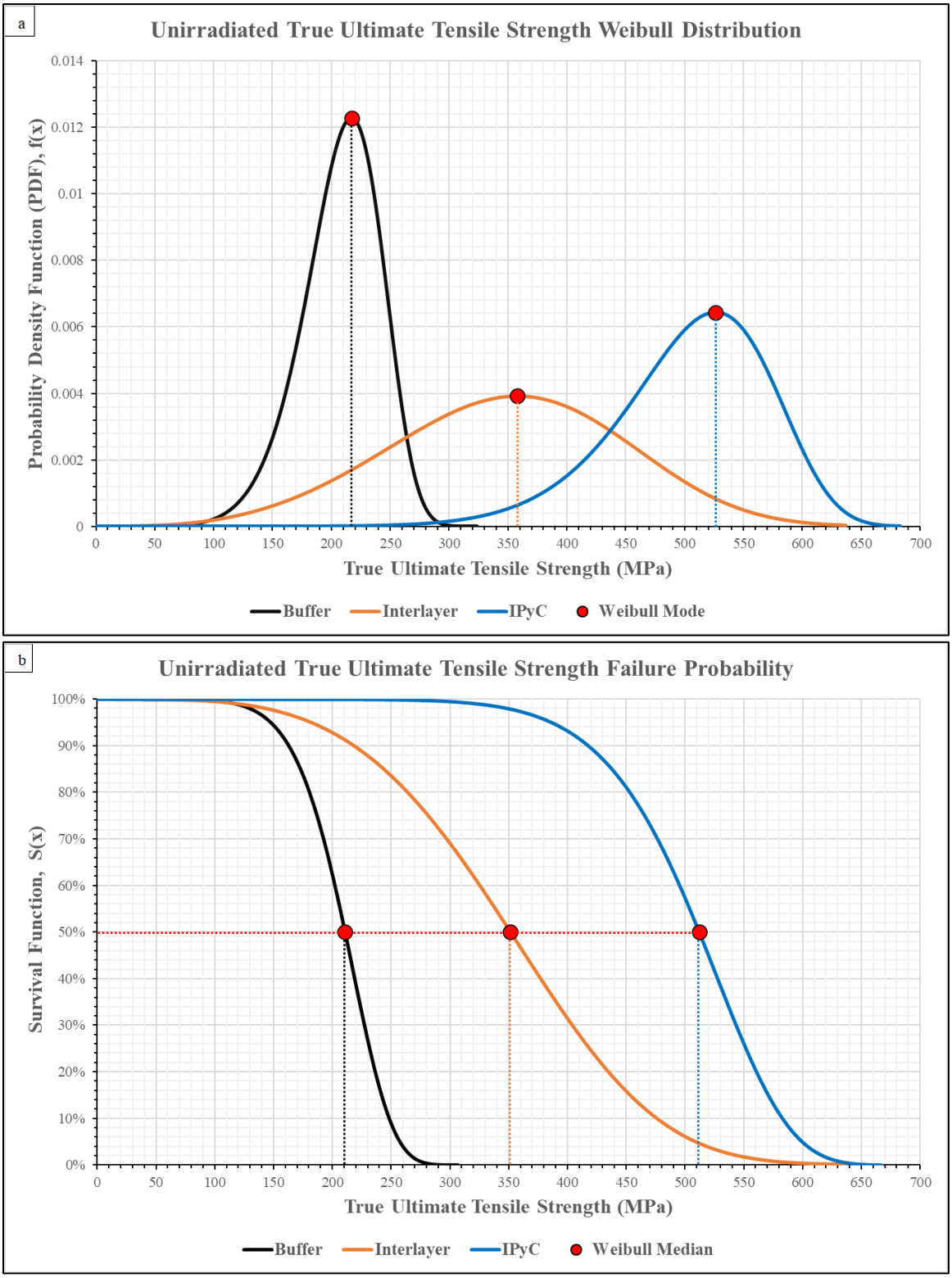

Figure 92. Graphs a) of the Weibull probability function versus ultimate tensile strength with associated Weibull modes and b) the Weibull survival function with associated Weibull medians for each of the unirradiated particle regions.

5.23 Irradiated Fueled TRISO Particles

Five buffer, nine buffer-IPyC interlayer, and four IPyC micro-tensile samples from the irradiated fueled TRISO particle were tested during this dissertation. Select stress strain curves from the buffer (a), IPyC (b), and buffer-IPyC interlayer (c)(d) regions that highlight the unique stress strain curve shapes for each region are shown in Fig. 93.

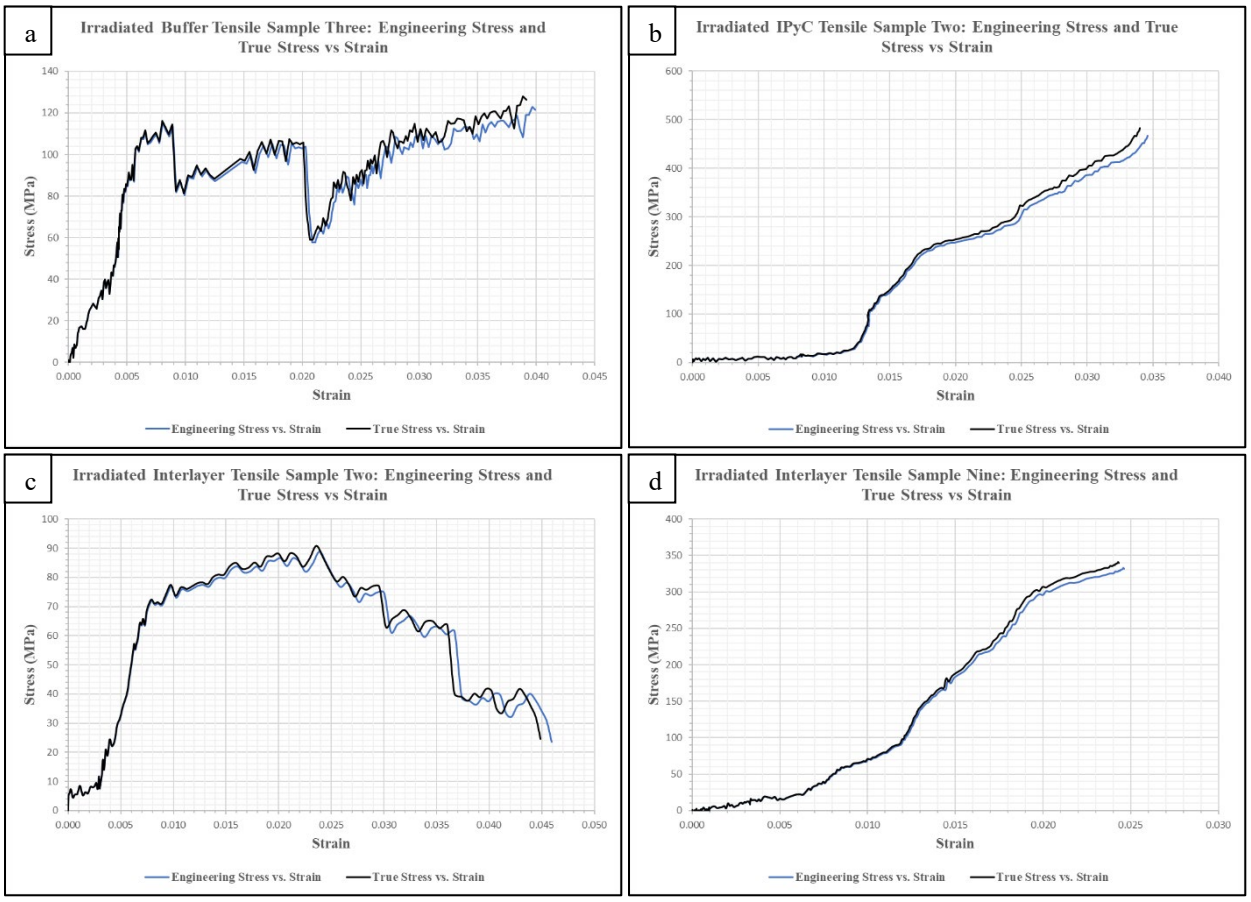

Figure 93. Graphs a) displays "rippling" as seen in the stress strain curve of irradiated buffer tensile sample three, b) displays sharp and abrupt fracture commonly seen in brittle materials as seen in the stress strain curve of irradiated IPyC tensile sample two, and c) and d) display both behaviors as seen in unirradiated interlayer tensile samples two and nine.

Table VI. Irradiated Fueled TRISO Particle Gauge Section Standard Statistics

Irradiated Fueled TRISO Particle Gauge Section Standard Statistics							
Sample Name	Height (μm)	Width (μm)	Depth (μm)	Detected Load at Fracture (μN)	Engineering Total Strain	True Total Strain	True Ultimate Tensile Strength (MPa)
Buffer 01	6.48	1.59	1.29	375.67	0.009	0.008	184.08
Buffer 02	6.33	1.77	1.18	224.58	0.003	0.003	107.70
Buffer 03	6.39	1.80	1.12	245.26	0.040	0.039	126.41
Buffer 04	6.32	1.85	1.24	138.33	0.005	0.005	60.48
Buffer 05	6.37	1.86	1.23	508.77	0.005	0.005	223.24
Interlayer 01	6.36	1.84	1.29	136.11	0.015	0.015	58.08
Interlayer 02	6.30	1.94	1.47	252.75	0.024	0.024	90.93
Interlayer 03	6.30	1.94	1.47	208.00	0.028	0.027	75.12
Interlayer 04	6.23	1.80	1.44	81.67	0.047	0.046	33.13
Interlayer 05	6.27	1.93	1.47	125.29	0.019	0.018	45.19
Interlayer 06	6.20	2.06	1.44	335.69	0.018	0.018	114.94
Interlayer 08	6.28	1.89	1.32	723.49	0.026	0.026	298.46
Interlayer 09	6.22	1.95	1.23	797.42	0.025	0.024	340.96
Interlayer 10	6.25	2.02	0.97	82.36	0.025	0.024	43.11
IPyC 02	6.38	2.03	1.22	1154.36	0.035	0.034	483.27
IPyC 03	6.36	2.02	1.30	734.08	0.019	0.019	284.25
IPyC 04	6.30	2.11	1.33	1055.35	0.025	0.025	386.67
IPyC 05	6.30	2.03	1.32	1237.47	0.032	0.031	476.57
Buffer Standard Mean	6.38	1.75	1.21	-	0.012	0.012	140.38
Interlayer Standard Mean	6.27	1.93	1.34	-	0.025	0.025	122.21
IPyC Standard Mean	6.33	2.05	1.29	-	0.028	0.027	407.69
Buffer Standard Deviation	-	-	-	-	0.016	0.015	64.07
Interlayer Standard Deviation	-	-	-	-	0.009	0.009	115.33
IPyC Standard Deviation	-	-	-	-	0.007	0.007	93.34
Buffer Coefficient of Variation	-	-	-	-	1.25	1.24	0.46
Interlayer Coefficient of Variation	-	-	-	-	0.37	0.37	0.94
IPyC Coefficient of Variation	-	-	-	-	0.25	0.25	0.23
Buffer Standard Error	-	-	-	-	0.007	0.007	28.66
Interlayer Standard Error	-	-	-	-	0.003	0.003	38.44
IPyC Standard Error	-	-	-	-	0.003	0.003	46.67
Buffer 95% Confidence Interval SEM	-	-	-	-	0.000, 0.026	0.000, 0.026	84.22, 196.55
Interlayer 95% Confidence Interval SEM	-	-	-	-	0.019, 0.031	0.019, 0.031	46.87, 197.56
IPyC 95% Confidence Interval SEM	-	-	-	-	0.021, 0.034	0.021, 0.034	316.22, 499.16

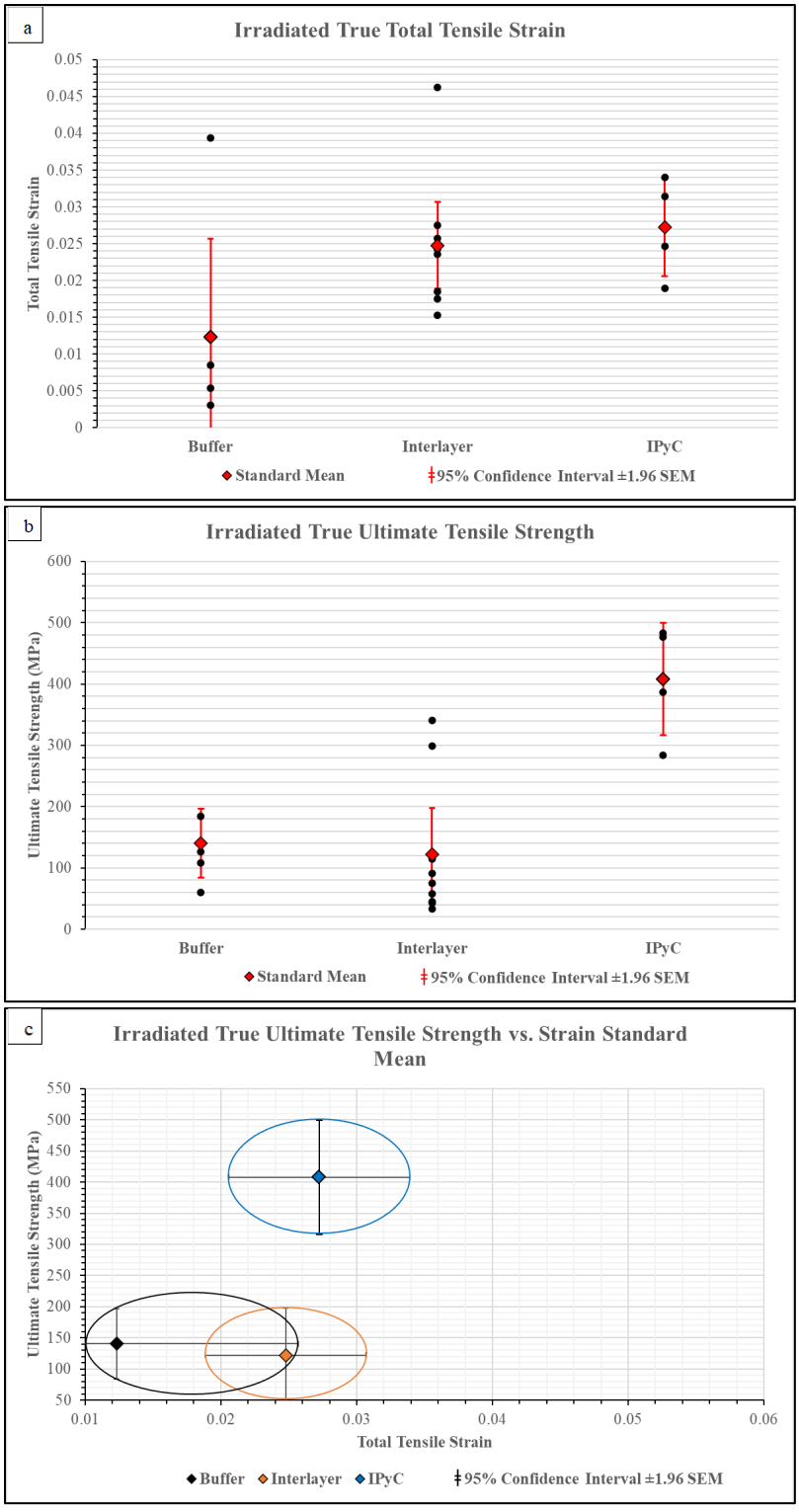

Figure 94. Graphs a) true total strain values for each of the irradiated particle regions micro-tensile samples along with 95% confidence interval, b) true ultimate tensile strength values along with 95% confidence interval, and c) the mean true total strain versus ultimate tensile strength with 95% confidence interval.

Table VII. Irradiated Fueled TRISO Particle Weibull Statistics

Weibull Linear Regression Values				
Buffer True Strength (MPa)	Assigned Number	F	"X" ln(Strength at Failure)	"Y" ln(ln(1/(1-F)))
60.48	1	0.10	4.10	-2.25
107.70	2	0.30	4.68	-1.03
126.41	3	0.50	4.84	-0.37
184.08	4	0.70	5.22	0.19
223.24	5	0.90	5.41	0.83
Interlayer True Strength (MPa)				
33.13	1	0.06	3.50	-2.86
43.11	2	0.17	3.76	-1.70
45.19	3	0.28	3.81	-1.12
58.08	4	0.39	4.06	-0.71
85.54	5	0.50	4.45	-0.37
90.93	6	0.61	4.51	-0.06
114.94	7	0.72	4.74	0.25
298.46	8	0.83	5.70	0.58
340.96	9	0.94	5.83	1.06
IPyC True Strength (MPa)				
284.25	1	0.13	5.65	-2.01
386.67	2	0.38	5.96	-0.76
476.57	3	0.63	6.17	-0.02
483.27	4	0.88	6.18	0.73

Two Parameter Weibull Distribution Values			
Parameter/Value	Buffer	Interlayer	IPyC
Shape Parameter, β	2.25	1.34	4.57
Scale Parameter, η	163.14	133.68	446.32
Intercept	-11.44	-6.54	-27.90
R^2	0.98	0.83	0.94
Standard Error of Regression	0.17	0.54	0.35
P-Value	3.29E-04	4.87E-09	7.95E-04
Weibull Mean (MPa)	144.50	122.82	407.68
Weibull Mode (MPa)	125.48	47.53	422.87
Weibull Median (MPa)	138.57	101.60	411.94
Weibull Variance (MPa)	68.08	92.88	101.29

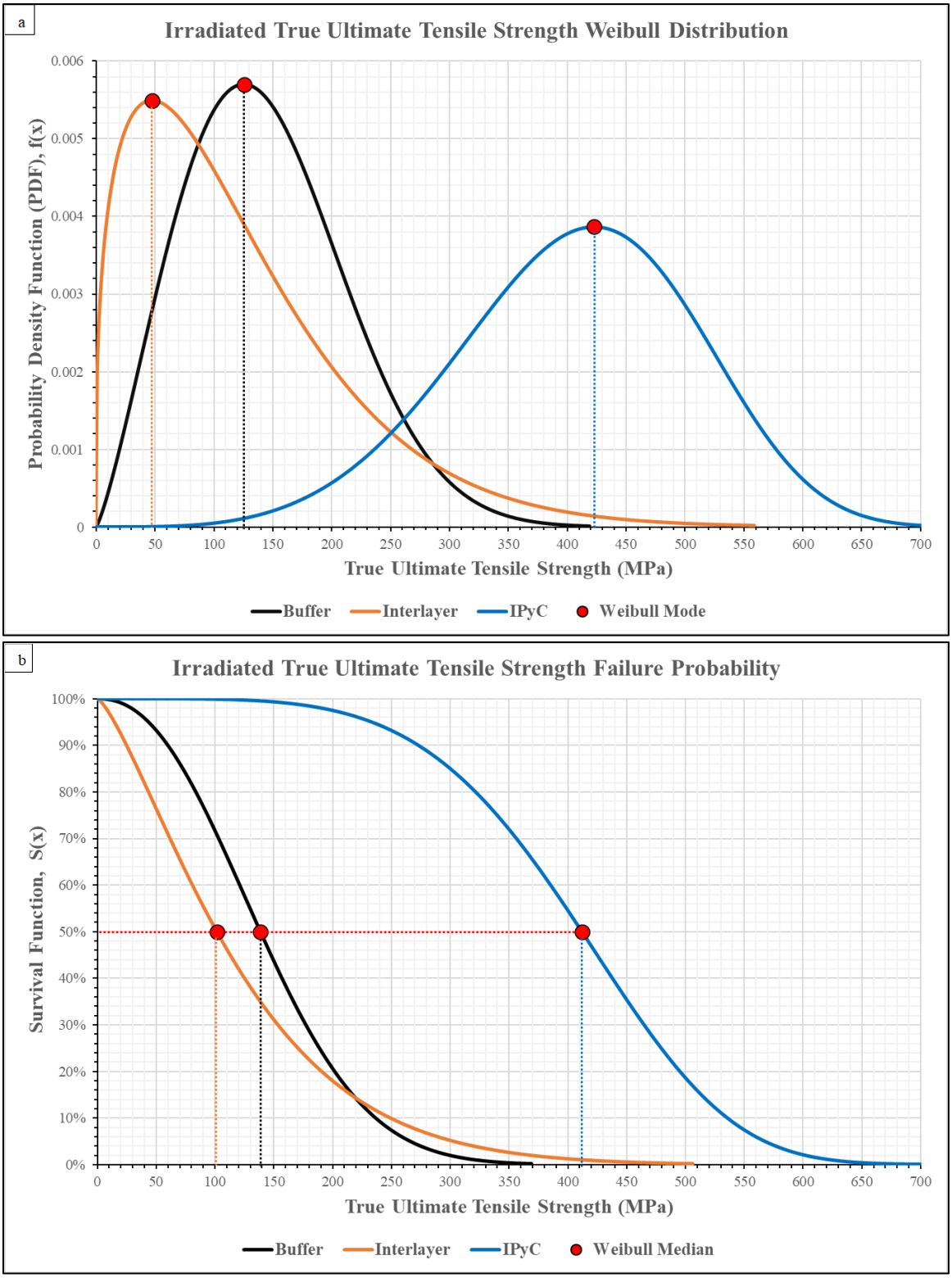

Figure 95. Graphs a) of the Weibull probability function versus ultimate tensile strength with associated Weibull modes and b) the Weibull survival function with associated Weibull medians for each of the irradiated particle regions.

6.0 Discussion and Analysis

Of the materials used for tensile testing technique verification, only the copper samples yielded useful results (Table I). These results were compared to tensile strength data from the Copper Development Institute, which were similar. Copper tensile strength data from Kiener and Minor (Kiener & Minor, 2011) were not similar to verification data; however, as can be seen in Fig. 86, the verification data is consistent with the gauge diameter trend seen in Kiener and Minor. The strength disparity is due to crystalline size effects on the ultimate tensile strength of the samples. When accounting for these crystalline size effects, the verification data compare well with tensile strengths reported by both the Copper Development Association and Kiener and Minor (Mauseth et al., 2023).

Comparing micro-tensile results between the buffer, IPyC, and buffer-IPyC interlayer samples from the individual TRISO particles revealed both expected and unexpected behaviors. As seen in Fig. 89b, 92b, and 95b, the buffer layer had significantly less median ultimate tensile strength than the IPyC layer in all TRISO particles tested (surrogate, unirradiated, and irradiated). This was expected, as the buffer region is porous, resulting in a relatively low solid material cross sectional area compared to IPyC. The smaller cross sectional area and more microstructural defects due to porosity in the buffer layer micro-tensile samples resulted in localized stresses during testing and a lower ultimate tensile strength (HASSELMAN, 1969). As seen in Fig. 87a, 90a, and 93a, the stress strain curves from buffer layer tensile testing had deviations/rippling, which was likely caused by the fracture propagation being slowed down by the pores (X. Zhang et al., 2019). The IPyC layer micro-tensile samples' stress strain curves were similar to those for classic brittle materials, with a straight line and abrupt fracture (Fig. 87b, 90b, and 93b). Due to the relative size of the pores in comparison to the buffer micro-tensile samples gauge section, large variations in

the tensile results were seen and is a limiting factor of using this testing technique (Mauseth et al., 2023). Unexpected behavior was displayed by the buffer-IPyC interlayer micro-tensile samples. As illustrated in Fig. 98, all buffer-IPyC interlayer samples fractured either in the buffer region or at the buffer-IPyC interface, which is consistent with observations made in the AGR-2 study by Stempien et al. and with the engineered delamination behavior TRISO particles are designed to exhibit at the buffer-IPyC interface (Stempien et al., 2021). Because each buffer-IPyC interlayer sample fractured either within the buffer region or at the buffer-IPyC interface, it was expected that the buffer-IPyC interlayer samples micro-tensile and stress strain properties would be similar to the pure buffer layer properties. However, the buffer-IPyC interlayer sample fractures occurred at higher median ultimate tensile strengths than that exhibited by the pure buffer layer samples from the surrogate and unirradiated TRISO particles (Fig. 89b and 92b) and at a lower median ultimate tensile strength than that exhibited by the pure buffer layer samples from the irradiated TRISO particle (Fig. 95b). Additionally, while both the buffer and IPyC layer samples micro-tensile tests resulted in fairly consistent stress strain curve shapes (Fig. 87a, 90a, 93a, and 87b, 90b, 93b), some of the buffer-IPyC interlayer samples exhibited stress strain curves similar to the buffer layer samples and some similar to the IPyC layer samples (Fig. 87c, 90c, 93c, and 87d, 90d, 93d). Furthermore, while the buffer-IPyC interlayer micro-tensile samples exhibited preferential fracture locations near the buffer-IPyC interface (Fig. 98), both the buffer and IPyC layer micro-tensile samples fractured at seemingly random locations along their gauge sections (Fig. 96 and 97), indicative of homogeneous brittle materials with randomly dispersed defects (HASSELMAN, 1969). Due to the different ultimate tensile strength, stress strain, and fracture behaviors demonstrated between the buffer, IPyC, and buffer-IPyC interlayer region samples across all TRISO particles tested (surrogate, unirradiated, and irradiated), it is clear that the buffer-IPyC

interlayer region must be treated as having material characteristics distinct from the buffer and IPyC layers for modeling and validation purposes.

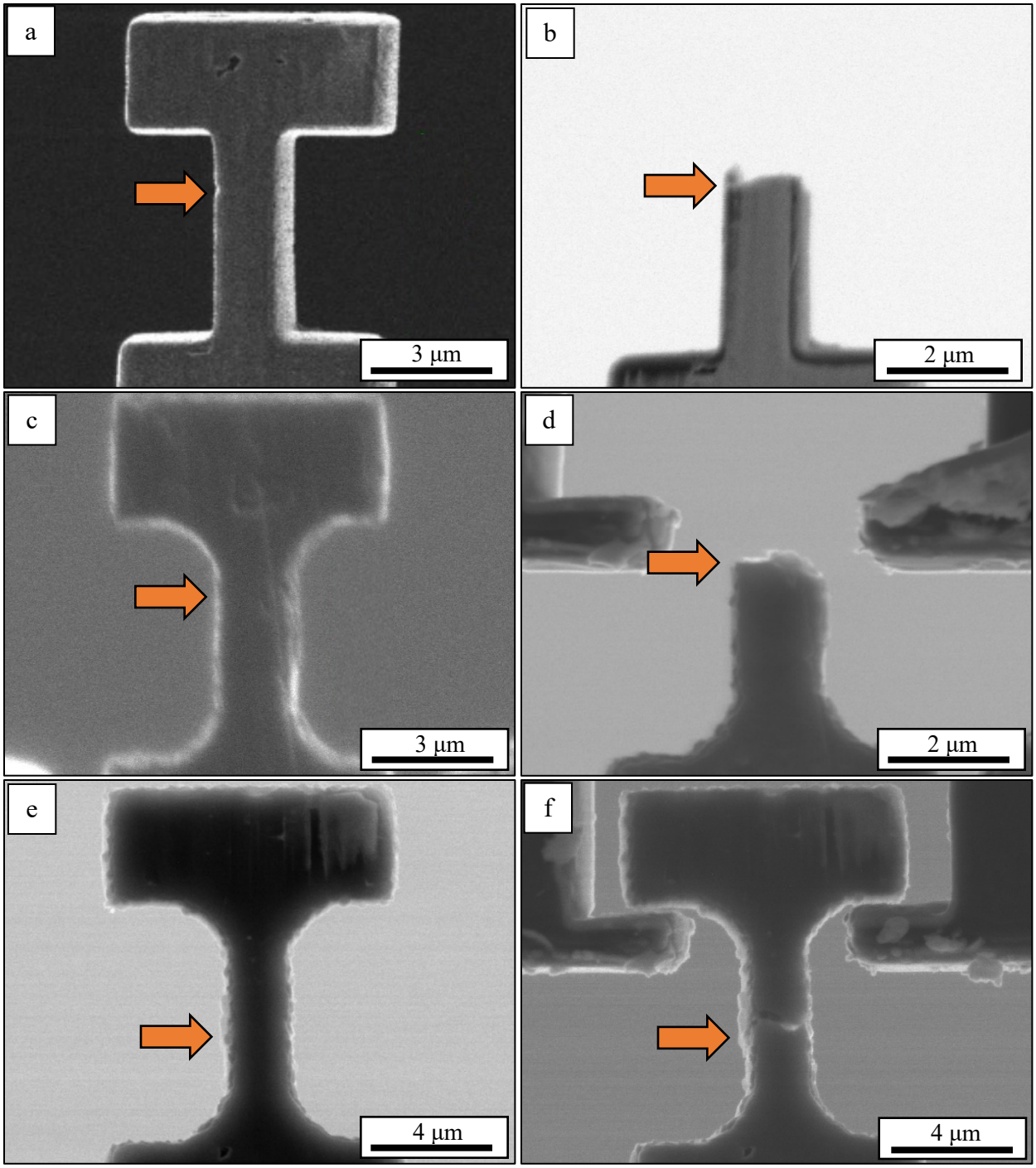

Figure 96. Images of surrogate TRISO particle IPyC layer sample three a) before and b) after fracture, unirradiated TRISO particle IPyC layer sample four c) before and d) after fracture, and irradiated TRISO particle IPyC layer sample three e) before and f) after fracture. The orange arrows denote the location of fracture for both the before and after fracture images.

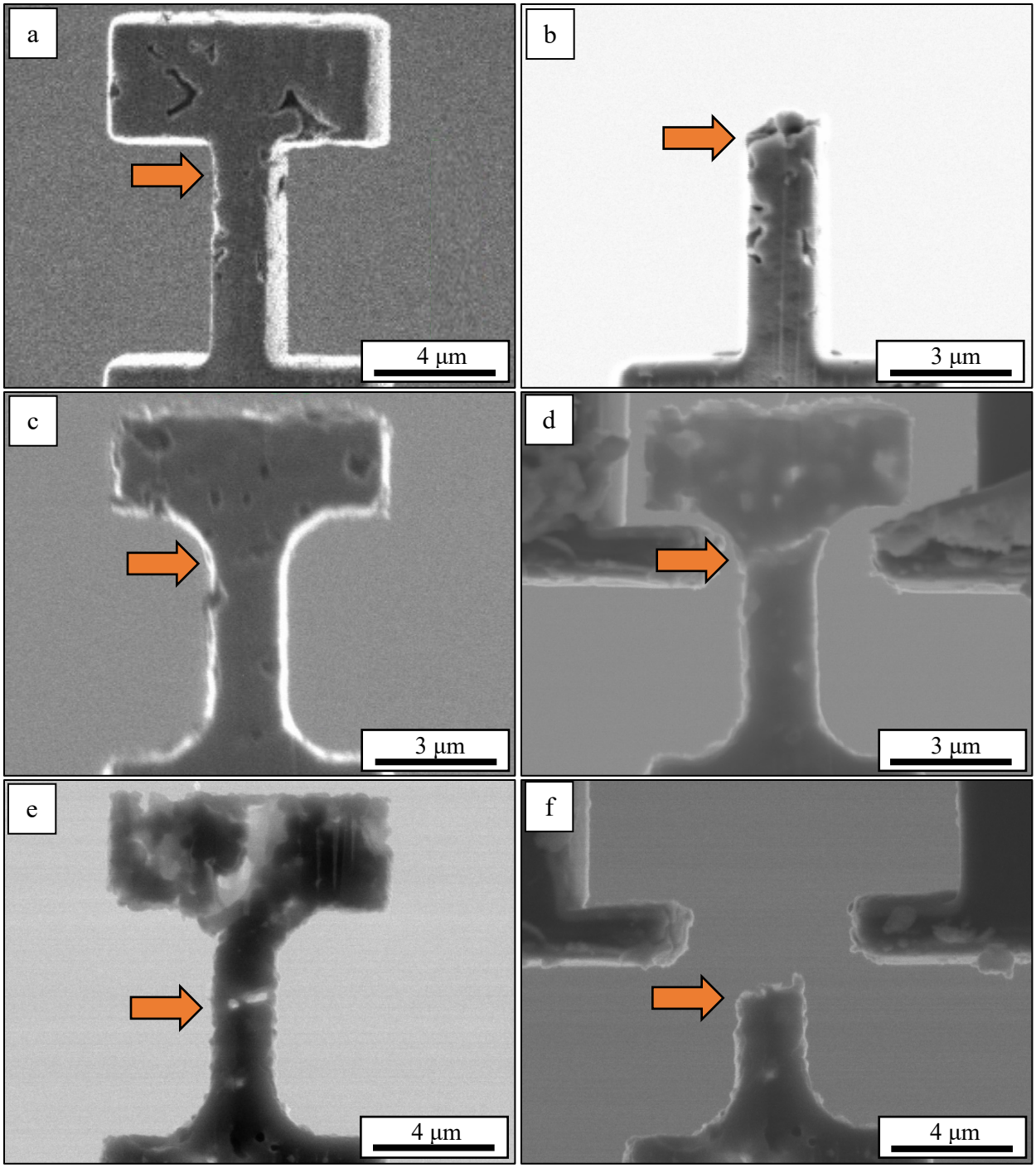

Figure 97. Images of surrogate TRISO particle buffer layer sample five a) before and b) after fracture, unirradiated TRISO particle buffer layer sample three c) before and d) after fracture, and irradiated TRISO particle buffer layer sample three e) before and f) after fracture. The orange arrows denote the location of fracture for both the before and after fracture images.

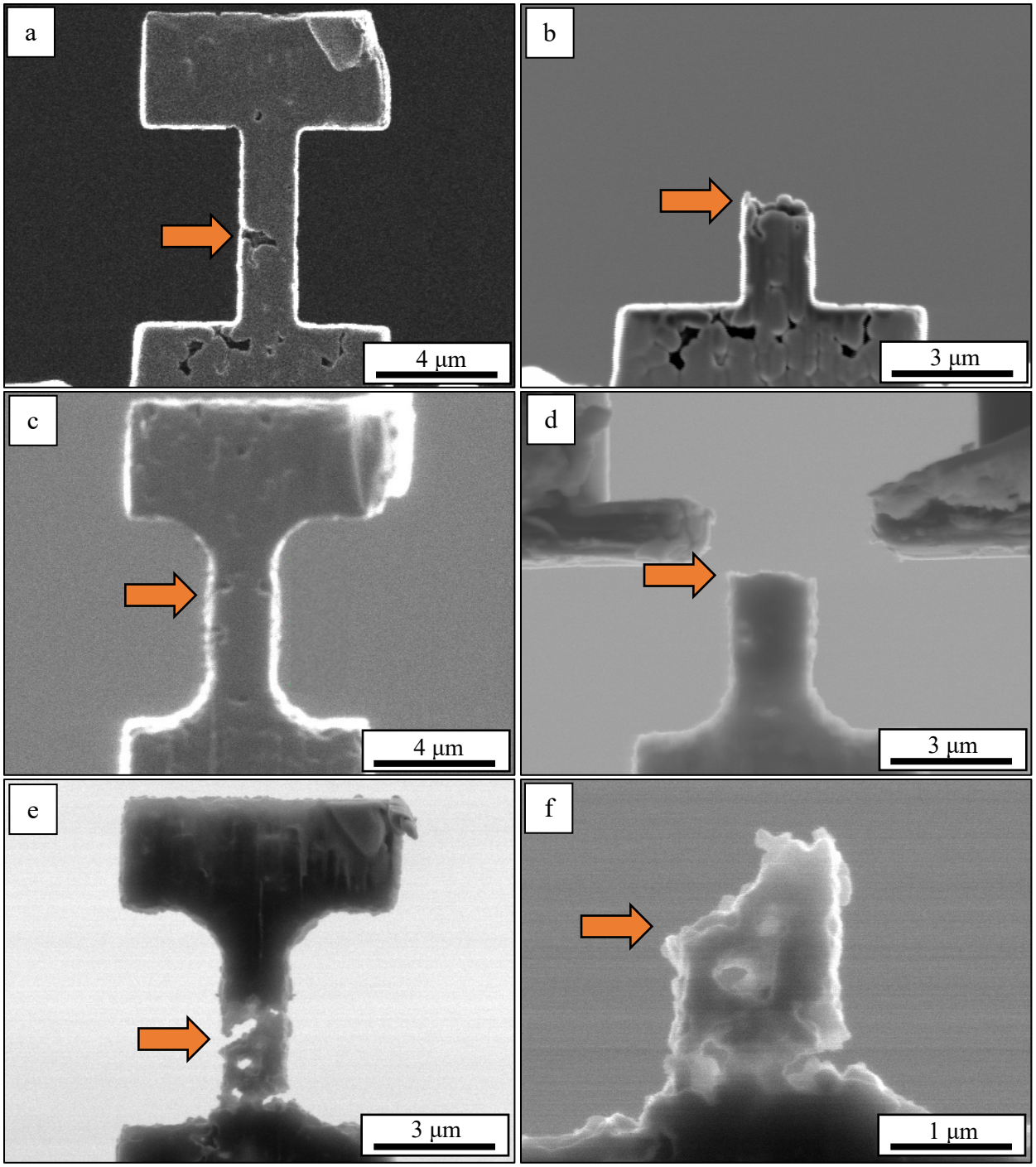

Figure 98. Images of surrogate TRISO particle buffer-IPyC interlayer sample nine a) before and b) after fracture, unirradiated TRISO particle buffer-IPyC interlayer sample seven c) before and d) after fracture, and irradiated TRISO particle buffer-IPyC interlayer sample ten e) before and f) after fracture. The orange arrows denote the location of fracture for both the before and after fracture images.

When comparing micro-tensile results between different TRISO particles, two distinct comparisons should be made: one between ultimate tensile strengths of samples from the surrogate and unirradiated TRISO particles and one between ultimate tensile strengths of samples from the unirradiated and irradiated TRISO particles. Samples from the surrogate and unirradiated TRISO particles have in common that they are both unirradiated; however, they were produced in different conditions, resulting in different layer properties (especially density) (PBMR program vs AGR program). As such, for these samples, the ultimate tensile strength is the dependent variable, the fabrication condition/material density is the independent variable, and the irradiation condition is the control variable. Samples from the unirradiated and irradiated TRISO particles have similar fabrication conditions/material densities (both AGR program) but have different irradiation conditions. Therefore, the ultimate tensile strength is the dependent variable, the irradiation condition is the independent variable, and the fabrication condition/material density is the control variable. As the surrogate and irradiated TRISO particle individual layer samples possess both different fabrication conditions/material densities (PBMR program vs. AGR program) and irradiation conditions (unirradiated vs. irradiated), a control variable is not possible and a comparison of the ultimate tensile strengths of layers from these particles is of no value. When comparing the surrogate and unirradiated TRISO particles individual layer samples ultimate tensile strengths, it was clear that every single layer from the unirradiated TRISO particle was significantly stronger than its corresponding surrogate TRISO particle layer (Tables VIII, IX, X and Fig. 99b, 100b, 101b). While the buffer and buffer-IPyC interlayer micro-tensile sample results from this dissertation are novel and difficult to compare to literature, other works have investigated properties in materials similar to the surrogate and unirradiated IPyC layers presented in this dissertation. When comparing the surrogate and unirradiated IPyC layer results in this dissertation

to the strength plot in the study done by Zhang et al. (2019), it appears the surrogate IPyC layer samples in this dissertation are on the low end of the strength range while the unirradiated IPyC layer samples are closer to the middle of the strength range of reference PyC material. The strength of the reference PyC ranged from ~150 MPa to 1.60 ± 0.55 GPa. The median ultimate tensile strength of the surrogate IPyC layer reported in this dissertation was ~191 MPa, while the median ultimate tensile strength result of the unirradiated IPyC layer was ~512 MPa (Stein et al., 2017; H. Zhang et al., 2015; X. Zhang et al., 2019). Additionally, the surrogate IPyC layer has a relatively low density (1.67 g/cm^3 vs 1.9 g/cm^3 or higher typically found in PyC materials and in the unirradiated IPyC layer in this dissertation). The low tensile strength and density of the surrogate IPyC layer samples in this dissertation align with the trends seen in Zhang et al. (2015), which suggests density has a stronger effect on the mechanical properties of PyC for densities below 1.9 g/cm^3 (Zhang et al., 2015).

When comparing the unirradiated and irradiated TRISO particles individual layer samples ultimate tensile strengths, it was clear that every single layer from the unirradiated TRISO particle was significantly stronger than its corresponding irradiated TRISO particle layer (Tables VIII, IX, X and Fig. 99b, 100b, 101b). Most apparent, however, was the drastic difference in the ultimate tensile strength between the unirradiated and irradiated TRISO particles buffer-IPyC interlayer samples (Table X and Fig. 101b). In conjunction with the reduced ultimate tensile strength, there appeared to be a noticeable increase in porosity in layers due to irradiation. This effect was most notable in the buffer-IPyC interlayer samples (Fig. 98c and 98e). The author suggests that the increase in porosity with irradiation was due to void volume formation and densification/contraction of the buffer layer resulting in incomplete delamination of the buffer-IPyC interface (Paul A. Demkowicz et al., 2015; Stempien et al., 2021; Was, 2007). As previously

discussed in regards to the buffer layer, increased porosity results in a reduced solid material cross sectional area and increase in microstructural defects, leading to an increase in localized stresses during tensile testing and a lower ultimate tensile strength (HASSELMAN, 1969). The irradiation induced increase in porosity in conjunction with reduced ultimate tensile strength of buffer-IPyC interlayer region suggests that irradiation induced porosity is the primary cause of mechanical failure in the TRISO particles' buffer-IPyC interlayer material system.

Further analysis of the experimental data was conducted with the application of standard and Weibull statistics. As seen in Fig. 91c, the confidence interval spread suggests the samples from buffer, IPyC, and buffer-IPyC interlayer regions of the unirradiated TRISO particle display distinct material properties. In contrast, buffer and buffer-IPyC interlayer samples from the surrogate and irradiated TRISO particles display similar behavior, distinct from the IPyC samples from the same particles (Fig. 88c and 94c). As mentioned in section 5.2, due to the highly probabilistic nature of the behavior of brittle materials, Weibull statistics are needed to help further unveil the material properties from these TRISO particle layer regions. Of particular interest is the ability of Weibull statistics to model many different types of distributions with a high level of accuracy, with the fundamental variable of interest being the Weibull modulus/shape parameter, β. Analogous to the evaluation and comparison of the ultimate tensile strengths between the different TRISO particles individual layers, two distinct comparisons should be made: one between the Weibull modulus/shape parameters of data from surrogate and unirradiated TRISO particles and one between the Weibull modulus/shape parameters of data from unirradiated and irradiated TRISO particles. When comparing these parameters from the surrogate and unirradiated TRISO particles, it was clear that every layer from the unirradiated TRISO particle had a significantly higher Weibull modulus/shape parameter than its corresponding surrogate TRISO particle layer

(Tables VIII, IX, X and Fig. 99a, 100a, 101a) . Much like in the ultimate tensile strength analysis, while the buffer and buffer-IPyC interlayer Weibull modulus/shape parameters from this dissertation are novel and difficult to compare to literature, other works have investigated the Weibull modulus/shape parameter of PyC which can be compared to the surrogate and unirradiated IPyC layers found in this dissertation. The Weibull modulus/shape parameter observed in the PARFUME handbook is 9.5 for PyC with a density of 1.9 g/cm^3 (Miller et al., 2018). The Weibull modulus/shape parameter for data from the surrogate particles' IPyC layer in this dissertation is 2.83 with a density of 1.67 g/cm^3 and the Weibull modulus/shape parameter for data from the unirradiated particles' IPyC layer is 9.26 with a density of 1.85-1.95 g/cm^3. While the unirradiated IPyC layer parameters are in almost perfect agreement with the reference PyC material, the surrogate IPyC layer parameter is significantly lower, indicative of the relatively large variation in the low tensile strengths observed in the surrogate particles IPyC layer samples. As mentioned in section 5.2, this variation could mean either that the surrogate IPyC layer material is relatively heterogenous/inconsistent in comparison to the reference PyC or that there are localized size effects due to the size of the tensile gauge section. Conducting a tensile gauge size sensitivity analysis would address the question of localized size effects (Carpinteri & Ferro, 1994; Karnati et al., 2022; Leguillon & Piat, 2008). When comparing the Weibull modulus/shape parameters for data from unirradiated and irradiated TRISO particles, again it was clear that every layer from the unirradiated TRISO particle had a significantly higher parameter value than its corresponding irradiated TRISO particle layer (Tables VIII, IX, X and Fig. 99a, 100a, 101a) . Just like with the ultimate tensile strength analysis, the most apparent impact of irradiation was the very low value of the Weibull modulus/shape parameter of data from the buffer-IPyC interlayer regions (Table X and Fig. 101a). This major reduction in the Weibull modulus/shape parameter with irradiation

is clearly a result of the increased heterogeneity due to irradiation induced porosity and the associated reduction in ultimate tensile strength. In conjunction with the evident increase in buffer-IPyC interlayer porosity and reduced ultimate tensile strength with irradiation, the major reduction of the Weibull modulus/shape parameter is further evidence that irradiation induced porosity is the primary cause of mechanical failure in the TRISO particles buffer-IPyC interlayer material system.

Table VIII. IPyC Layer Properties Comparison

IPyC Tensile Sample Mechanical Values	Surrogate	Unirradiated	Irradiated
Average True Ultimate Tensile Strength (MPa)	189.74	506.76	407.69
Average True Total Strain	0.04	0.02	0.03
Average Elastic Modulus (GPa)	4.38	31.69	15.06
Weibull Modulus/Shape Parameter, β	2.83	9.26	4.57
Weibull Mode (MPa)	186.06	526.27	422.87
Weibull Median (MPa)	190.69	512.12	411.94

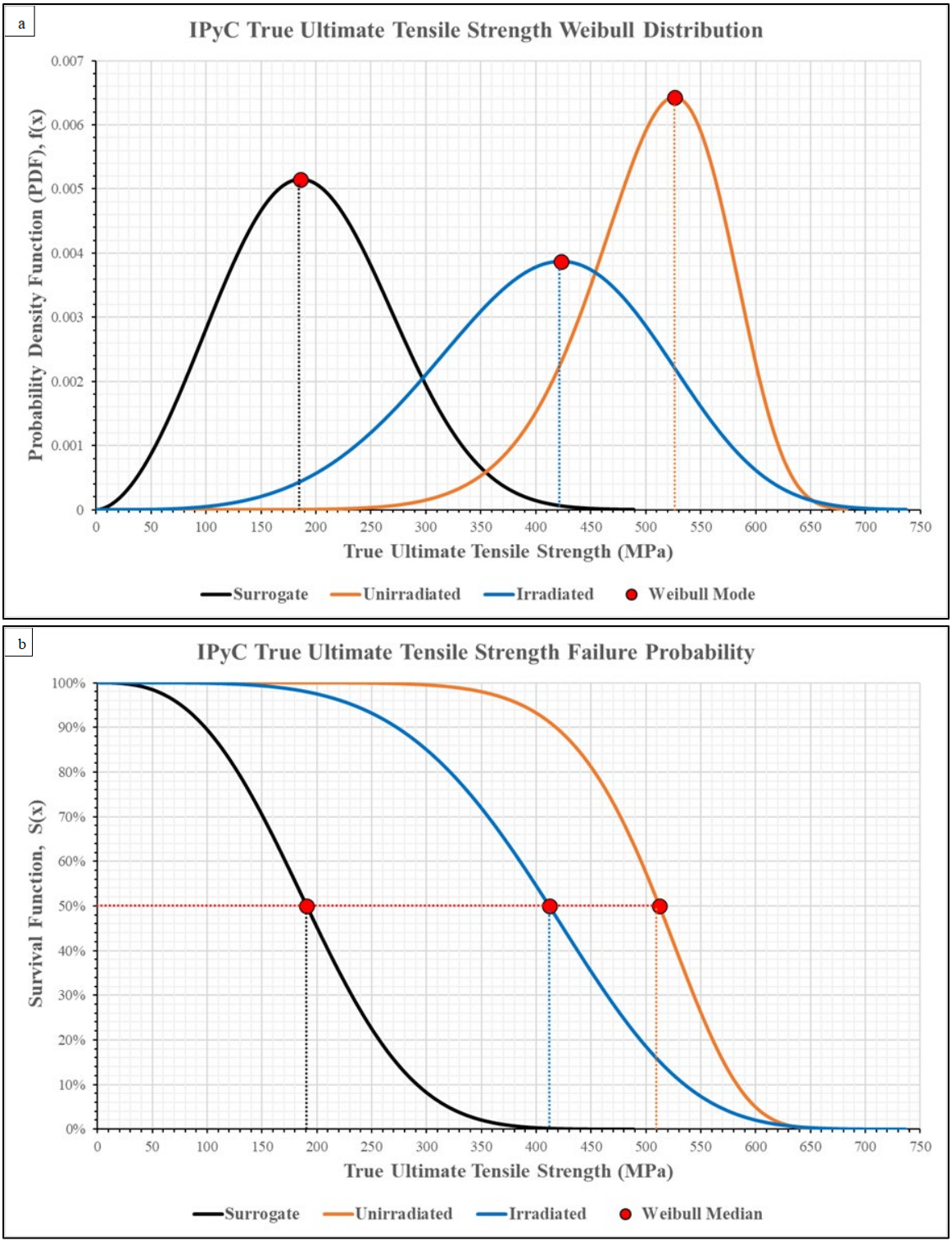

Figure 99. Graphs a) of the Weibull probability function versus ultimate tensile strength with associated Weibull modes and b) the Weibull survival function with associated Weibull medians for each of the TRISO particles IPyC layer regions.

Table IX. Buffer Layer Properties Comparison

Buffer Tensile Sample Mechanical Values	Surrogate	Unirradiated	Irradiated
Average True Ultimate Tensile Strength (MPa)	138.70	208.39	140.38
Average True Total Strain	0.03	0.01	0.01
Average Elastic Modulus (GPa)	6.89	19.35	22.83
Weibull Modulus/Shape Parameter, β	3.14	7.32	2.25
Weibull Mode (MPa)	138.31	217.16	125.48
Weibull Median (MPa)	139.03	210.74	138.57

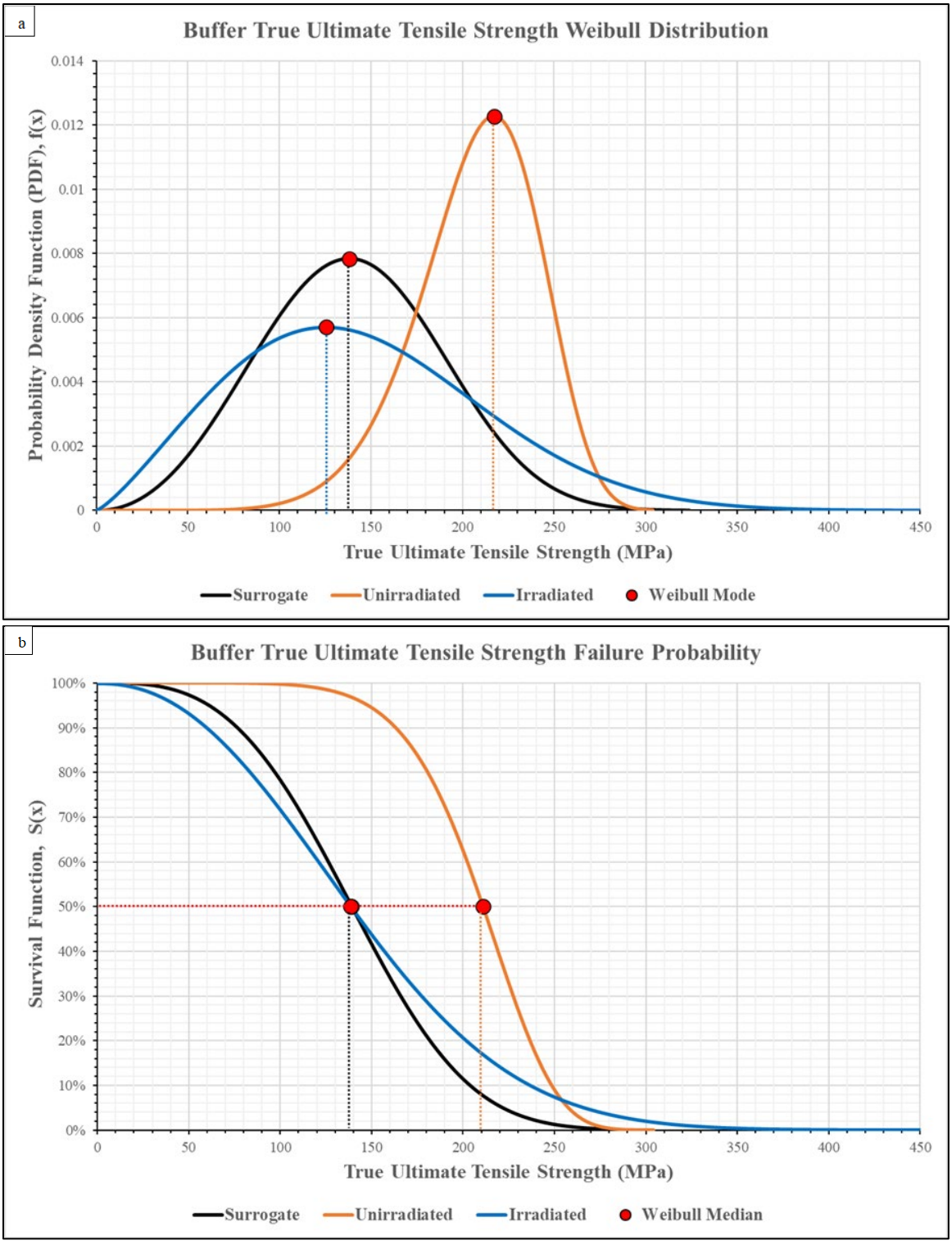

Figure 100. Graphs a) of the Weibull probability function versus ultimate tensile strength with associated Weibull modes and b) the Weibull survival function with associated Weibull medians for each of the TRISO particles buffer layer regions.

Table X. Buffer-IPyC Interlayer Properties Comparison

Interlayer Tensile Sample Mechanical Values	Surrogate	Unirradiated	Irradiated
Average True Ultimate Tensile Strength (MPa)	159.80	349.11	122.21
Average True Total Strain	0.03	0.03	0.03
Average Elastic Modulus (GPa)	7.11	14.38	5.30
Weibull Modulus/Shape Parameter, β	2.02	3.96	1.34
Weibull Mode (MPa)	130.07	358.11	47.53
Weibull Median (MPa)	152.22	351.33	101.60

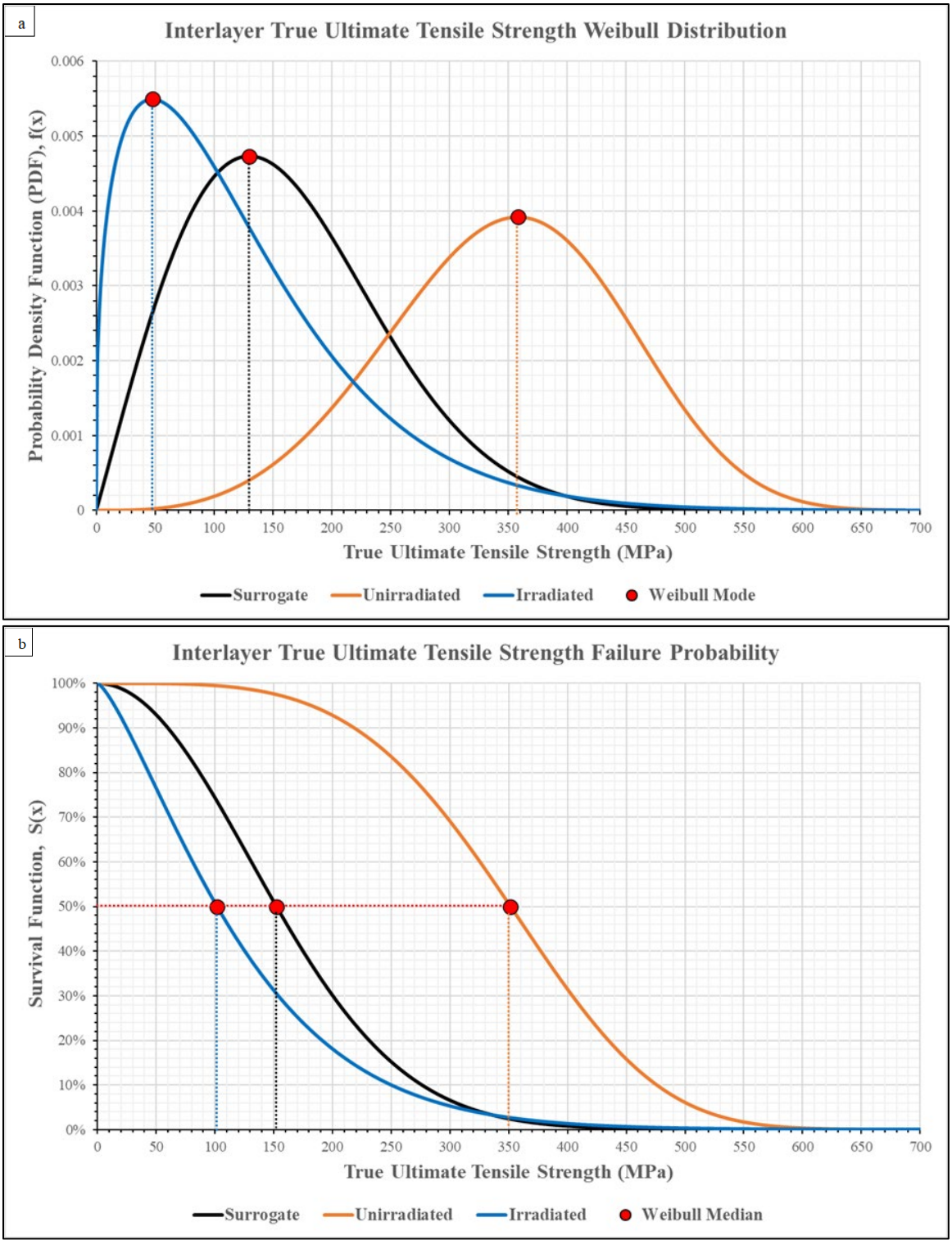

Figure 101. Graphs a) of the Weibull probability function versus ultimate tensile strength with associated Weibull modes and b) the Weibull survival function with associated Weibull medians for each of the TRISO particles buffer-IPyC interlayer regions.

7.0 Conclusion and Future Works

Through the course of work presented in this dissertation, the micro-tensile sample fabrication technique was refined. Initial application of the technique to copper micro-tensile samples allowed for verification of the technique.

Numerous surrogate, unirradiated, and irradiated TRISO particle micro-tensile samples from the buffer, IPyC, and buffer-IPyC interlayer regions were fabricated and tested. While the pure buffer samples were weakest and the pure IPyC samples were strongest for the surrogate and unirradiated TRISO particles, the buffer-IPyC interlayer samples were weakest and the pure IPyC samples were strongest for the irradiated TRISO particles. All buffer-IPyC interface samples fractured either in the buffer layer region or at the buffer-IPyC interface, yet some of the interlayer samples displayed stress strain and fracture behavior more like the IPyC layer than the buffer layer. Due to the different ultimate tensile strength, stress strain, and fracture behaviors demonstrated by buffer, IPyC, and buffer-IPyC interlayer region samples from the TRISO particles tested (surrogate, unirradiated, and irradiated), it is clear that the buffer-IPyC interlayer region must be treated as having material characteristics distinct from the buffer and IPyC layers for modeling and validation purposes.

While the sample size was limited, application of standard and Weibull statistics to the experimental data broadened the scope of data analysis. The analysis showed that the unirradiated TRISO particle micro-tensile samples had both higher median ultimate tensile strengths and Weibull modulus/shape parameters than both the surrogate and irradiated TRISO particles micro-tensile samples for all regions (buffer, IPyC, and buffer-IPyC). Most apparent, however, were the significantly lower values of median ultimate tensile strength and Weibull modulus/shape parameter for the irradiated TRISO particle buffer-IPyC layer in comparison to the unirradiated

particle layer. In conjunction with the clear increase in porosity of the buffer-IPyC interlayer region with irradiation, the significantly lower ultimate tensile strength and Weibull modulus/shape parameter values of the irradiated particles buffer-IPyC interlayer region is evidence that irradiation induced porosity is the primary cause of mechanical failure in the TRISO particles buffer-IPyC interlayer material system.

As stated in the introduction, it should be noted that the tensile data reported in this dissertation is part of an overall effort working towards establishing micro-tensile testing as a viable technique to measure layer properties of TRISO particles. The sensitivity of the results to tensile gauge length and the impact of gauge width relative to the porosity distribution and pore size was not studied. As such, the accuracy of the data is questionable in that it may not be representative of modern TRISO fuel particles (though the data may be precise). The differences in the tensile properties shown in this dissertation provide context on the relative layer properties, but the values of the measured Weibull parameters, ultimate tensile strength, and ultimate tensile strain may not be representative of real fuel systems. A tensile gauge size sensitivity analysis for the buffer layer is recommended in order to characterize any porosity and/or localized size effects on the tensile strength (Mauseth et al., 2023).

Plans are in place to further analyze the unirradiated and irradiated TRISO particles' buffer, IPyC, and buffer-IPyC interlayer regions via TEM analysis (bright field, HAADF-STEM, diffraction, EELS, and EDS) as part of DOE NEUP 17251, with the buffer-IPyC interlayer regions also to be analyzed through APT-TEM correlation as part of NSUF RTE 4634. Additionally, thermally stressed micro-tensile testing and analysis of the surrogate TRISO particles buffer-IPyC interlayer region as part of DOE NEUP 17251 will comprise the master's thesis research for Mr. Charlie Rivera.

8.0 References

Amouyal, Y., & Schmitz, G. (2016). Atom probe tomography-A cornerstone in materials characterization. MRS Bulletin, 41(1), 13–18. https://doi.org/10.1557/mrs.2015.313

Anderson, T. L. (1995). Fracture mechanics 2nd Edn, publ. CRC, Boca Raton, Florida, USA.

Ando, M., Tanigawa, H., Kurotaki, H., & Katoh, Y. (2018). Mechanical properties of neutron irradiated F82H using micro-tensile testing. Nuclear Materials and Energy, 16, 258–262. https://doi.org/10.1016/j.nme.2018.07.008

Bauer, J., Schroer, A., Schwaiger, R., Tesari, I., Lange, C., Valdevit, L., & Kraft, O. (2015). Push-to-pull tensile testing of ultra-strong nanoscale ceramic-polymer composites made by additive manufacturing. Extreme Mechanics Letters, 3, 105–112. https://doi.org/10.1016/j.eml.2015.03.006

Bellan, C., & Dhers, J. (2004). Evaluation of Young modulus of CVD coatings by different techniques. Thin Solid Films, 469–470(SPEC. ISS.), 214–220. https://doi.org/10.1016/j.tsf.2004.08.182

Bower, G. R., Ploger, S. A., Demkowicz, P. A., & Hunn, J. D. (2017). Measurement of kernel swelling and buffer densification in irradiated UCO-TRISO particles. Journal of Nuclear Materials, 486(June), 339–349. https://doi.org/10.1016/j.jnucmat.2017.01.006

Browning, N. D., Wallis, D. J., Nellistt, + P D, & Pennycookt, S. J. (1997). EELS in the STEM: Determination of Materials Properties on the Atomic Scale (Vol. 28, Issue 97).

Byun, T. S., Hunn, J. D., Miller, J. H., Snead, L. L., & Kim, J. W. (2010). Evaluation of fracture stress for the SiC layer of TRISO-coated fuel particles using a modified crush test method. International Journal of Applied Ceramic Technology, 7(3), 327–337. https://doi.org/10.1111/j.1744-7402.2009.02462.x

Byun, T. S., Kim, J. W., Dunbar, I., & Hunn, J. D. (2008). Fracture Stress Data for SiC Layers in TRISO-Coated Fuel Particles.

ÇAPAR, Y. (2021). Engineering Stress/Strain vs True Stress/Strain. https://yasincapar.com/engineering-stress-strain-vs-true-stress-strain/

Carpinteri, A., & Ferro, G. (1994). Size effects on tensile fracture properties: a unified explanation based on disorder and fractality of concrete microstructure. In Materials and Structures (Vol. 27).

Chapin, D., Kiffer, S., & Nestell, J. (2004). The Very High Temperature Reactor: A Technical Summary.

Copper Developement Association Inc. (2021). Fundamentals: Types of Copper and Properties. https://www.copper.org/applications/architecture/arch_dhb/technical-discussion/fundamentals/intro.html

Dieter, G. E. (1961). Mechanical Metallurgy (R. F. Mehl & M. B. Bever, Eds.). McGraw-Hill Book Company, Inc.

EELS | Gatan, Inc. (n.d.). Retrieved February 14, 2023, from https://www.gatan.com/techniques/eels#

Essential Knowledge Briefings Electron probe microanalysis. (2015). www.essentialknowledgebriefings.com

Frazer, D., Szornel, J., Krumwiede, D. L., Terrani, K. A., & Hosemann, P. (2017). Evaluation of the Mechanical Properties of TRISO Particles Using Nanoindentation and Ring Compression Testing. Experimental Mechanics, 57(7), 1081–1090. https://doi.org/10.1007/s11340-017-0277-z

Fu, Z., van Rooyen, I. J., Bachhav, M., & Yang, Y. (2020). Microstructure and fission products in the UCO kernel of an AGR-1 TRISO fuel particle after post irradiation safety testing. Journal of Nuclear Materials, 528, 151884. https://doi.org/https://doi.org/10.1016/j.jnucmat.2019.151884

Gault, B., Chiaramonti, A., Cojocaru-Mirédin, O., Stender, P., Dubosq, R., Freysoldt, C., Makineni, S. K., Li, T., Moody, M., & Cairney, J. M. (2021). Atom probe tomography. Nature Reviews Methods Primers, 1(1), 51. https://doi.org/10.1038/s43586-021-00047-w

Gerczak, T. J., Hunn, J. D., Morris, R. N., Montgomery, F. C., Skitt, D. J., Baldwin, C. A., Dyer, J. A., & Eckhart, B. D. (2020). Analysis of fission product distribution and composition in the TRISO layers of AGR-2 fuel. Nuclear Engineering and Design, 364. https://doi.org/10.1016/j.nucengdes.2020.110656

Giannuzzi Lucille A. and Prenitzer, B. I. and K. B. W. (2005). Ion - Solid Interactions. In F. A. Giannuzzi Lucille A. and Stevie (Ed.), Introduction to Focused Ion Beams: Instrumentation, Theory, Techniques and Practice (pp. 13–52). Springer US. https://doi.org/10.1007/0-387-23313-X_2

Griesbach, C., Gerczak, T., Zhang, Y., & Thevamaran, R. (2023). Microstructural heterogeneity of the buffer layer of TRISO nuclear fuel particles. Journal of Nuclear Materials, 574. https://doi.org/10.1016/j.jnucmat.2022.154219

Griffith, A. (1921). The phenomena of rupture and flow in solids Philosophical Transactions, volume 221 of pp. 163-198. Royal Society of London A.

Gussev, M. N., Howard, R. H., Terrani, K. A., & Field, K. G. (2017). Sub-size tensile specimen design for in-reactor irradiation and post-irradiation testing. Nuclear Engineering and Design, 320, 298–308. https://doi.org/10.1016/j.nucengdes.2017.06.008

Hales, J. D., Williamson, R. L., Novascone, S. R., Perez, D. M., Spencer, B. W., & Pastore, G. (2013). Multidimensional multiphysics simulation of TRISO particle fuel. Journal of Nuclear Materials, 443(1–3), 531–543. https://doi.org/10.1016/j.jnucmat.2013.07.070

HASSELMAN, D. P. H. (1969). Griffith Flaws and the Effect of Porosity on Tensile Strength of Brittle Ceramics. Journal of the American Ceramic Society, 52(8), 457–457. https://doi.org/10.1111/J.1151-2916.1969.TB11982.X

Honorato, E. (2011). The High Temperature Reactor and the TRISO coated fuel particle (Part I) | GrInAEr-Lab. https://eddiehonorato.wordpress.com/2011/11/04/the-high-temperature-reactor-and-the-triso-coated-fuel-particle-part-i/

Hunn, J. D., Baldwin, C. A., Gerczak, T. J., Montgomery, F. C., Morris, R. N., Silva, C. M., Demkowicz, P. A., Harp, J. M., & Ploger, S. A. (2014). Detection and Analysis of Particles with Failed SiC in AGR-1 Fuel Compacts. https://doi.org/10.1016/j.nucengdes.2015.12.011.

Hunn, J. D., & Lowden, R. A. (n.d.). Property Versus Process Trends for Inner-Pyrocarbon Layers in TRISO-Coated Particle Fuel.

IAEA. (n.d.). PrismaticHTR.

Irwin, G. R. (1956). Onset of fast crack propagation in high strength steel and aluminum alloys.

Jiang, S., Tu, J., Yang, X., & Gui, N. (2019). A review of pebble flow study for pebble bed high temperature gas-cooled reactor. Experimental and Computational Multiphase Flow, 1(3), 159–176. https://doi.org/10.1007/s42757-019-0006-1

Jiang, W., Hales, J. D., Spencer, B. W., Collin, B. P., Slaughter, A. E., Novascone, S. R., Toptan, A., Gamble, K. A., & Gardner, R. (2021). TRISO particle fuel performance and failure analysis with BISON. Journal of Nuclear Materials, 548. https://doi.org/10.1016/j.jnucmat.2021.152795

Jiang, W., Singh, G., Hales, J. D., Toptan, A., Spencer, B. W., Novascone, S. R., Dhulipala, S. L. N., & Prince, Z. M. (2022). Efficient high-fidelity TRISO statistical failure analysis using Bison: Applications to AGR-2 irradiation testing. Journal of Nuclear Materials, 562. https://doi.org/10.1016/j.jnucmat.2022.153585

Kabel, J., Edwards, T. E. J., Sharma, A., Michler, J., & Hosemann, P. (2021). Direct observation of the elasticity-texture relationship in pyrolytic carbon via in situ micropillar compression and digital image correlation. Carbon, 182, 571–584. https://doi.org/10.1016/j.carbon.2021.06.045

Kallman, B. (2013). The Very High Temperature Reactor. http://large.stanford.edu/courses/2013/ph241/kallman1/

Karnati, S., Isanaka, S. P., Zhang, Y., Liou, F. F., & Schulthess, J. L. (2022). A Comparative Study on Representativeness and Stochastic Efficacy of Miniature Tensile Specimen Testing. Materials Performance and Characterization, 11(3). https://doi.org/10.1520/MPC20210136

Kiener, D., & Minor, A. M. (2011). Source truncation and exhaustion: Insights from quantitative in situ TEM tensile testing. Nano Letters, 11(9), 3816–3820. https://doi.org/10.1021/nl201890s

Klein, N. D., Hurley, K. R., Feng, Z. V., & Haynes, C. L. (2015). Dark field transmission electron microscopy as a tool for identifying inorganic nanoparticles in biological matrices. Analytical Chemistry, 87(8), 4356–4362. https://doi.org/10.1021/acs.analchem.5b00124

Lee, H. M., Park, K. Il, Park, J. Y., Kim, W. J., & Kim, D. K. (2015). High-temperature fracture strength of a CVD-SiC coating layer for TRISO nuclear fuel particles by a micro-tensile test. Journal of the Korean Ceramic Society, 52(6), 441–448. https://doi.org/10.4191/kcers.2015.52.6.441

Leguillon, D., & Piat, R. (2008). Fracture of porous materials - Influence of the pore size. Engineering Fracture Mechanics, 75(7), 1840–1853. https://doi.org/10.1016/j.engfracmech.2006.12.002

Leng, B., van Rooyen, I. J., Wu, Y. Q., Szlufarska, I., & Sridharan, K. (2016). STEM-EDS analysis of fission products in neutron-irradiated TRISO fuel particles from AGR-1 experiment. Journal of Nuclear Materials, 475, 62–70. https://doi.org/10.1016/j.jnucmat.2016.03.008

Li, R., Liu, B., & Verfondern, K. (2019). The study of irradiation-induced failure behavior for the TRISO-coated fuel particle in HTGR. Journal of Nuclear Materials, 516, 214–227. https://doi.org/10.1016/j.jnucmat.2019.01.029

Longer Term Accident Tolerant Fuel Technologies. (2021). In NRC.gov. https://www.nrc.gov/reactors/atf/longer-term.html

López-Honorato, E., Meadows, P. J., Shatwell, R. A., & Xiao, P. (2010). Characterization of the anisotropy of pyrolytic carbon by Raman spectroscopy. Carbon, 48(3), 881–890. https://doi.org/10.1016/j.carbon.2009.11.010

Lu, C., Danzer, R., & Fischer, F. D. (2002). Fracture statistics of brittle materials: Weibull or normal distribution. Physical Review E, 65(6), 067102. https://doi.org/10.1103/PhysRevE.65.067102

Mae, C. (2014). EBSD Determined Grain and Grain Boundary Characteristic Correlation with Deposition and Annealing Temperatures of the CVD coated SiC Layer of TRISO Particle Nuclear Fuel COMMITTEE APPROVAL. Idaho State University.

Materials and Fuels Complex - Shielded FEI Quanta 3D FEG. (n.d.). Retrieved February 14, 2023, from

https://mfc.inl.gov/SitePages/Instruments/Irradiated%20Materials%20Characterization%20Laboratory/Shielded%20FEI%20Quanta%203D%20FEG.aspx

Mauseth, T. (2021). Development of a Sample Preparation Technique for Determining the Tensile Strength of Select Layers and Layer Interfaces of TRISO Particles. Idaho State University.

Mauseth, T., Dunzik-Gougar, M. Lou, Meher, S., & van Rooyen, I. (2023). Determining the Tensile Strength of Fuel Surrogate TRISO-coated Particle Buffer, IPyC, and Buffer-IPyC Interlayer Regions. Journal of Nuclear Materials.

McSwiggen & Associates, -Tech Note: WDS vs EDS. (n.d.). Retrieved February 19, 2023, from http://www.mcswiggen.com/TechNotes/WDSvsEDS.htm

Miller, G. K., Petti, D. A., Maki, J. T., Knudson, D. L., & Skerjanc, W. F. (2018). PARFUME Theory and Model Basis Report. http://www.inl.gov

Mohr, D. L., Wilson, W. J., & Freund, R. J. (2021). Statistical Methods. Statistical Methods, 1–754. https://doi.org/10.1016/B978-0-12-823043-5.00015-1

NanoScan. (2018). Nanoindentation - Nanohardness testers NanoScan. http://nanoscan.info/eng/methods/nanoindentation

Nanoscience Instruments. (2021). Nanoindentation. In Nanoindentation. https://www.nanoscience.com/techniques/nanoindentation/

Office of Nuclear Energy. (2009). Advanced Gas Reactor Fuel Program's TRISO Particle Fuel Sets A New World Record For Irradiation Performance | Department of Energy. In U.S. Department of Energy. https://www.energy.gov/ne/articles/advanced-gas-reactor-fuel-programs-triso-particle-fuel-sets-new-world

Parma, E. J., Pickard, P. S., & Suo-Anttila, A. J. (2003). SANDIA REPORT Concepts for Electrical Power Generation and Hydrogen Production. http://www.doe.gov/bridge

Paul A. Demkowicz, John D. Hunn, Robert N. Morris, Isabella van Rooyen, Tyler Gerczak, Jason M. Harp, & Scott A. Ploger. (2015). AGR-1 Post Irradiation Examination Final Report. https://doi.org/10.2172/1236801

PBMR. (2017). PBMR - How the PBMR fuel works. http://www.pbmr.co.za/index2.asp?Content=224

PI 88 SEM PicoIndenter ®. (2020). https://airtable.com/shrrfypV1Wg7J9ULa

Quinn, J. B., & Quinn, G. D. (2010). A practical and systematic review of Weibull statistics for reporting strengths of dental materials. In Dental Materials (Vol. 26, Issue 2, pp. 135–147). https://doi.org/10.1016/j.dental.2009.09.006

Reichardt, A., Ionescu, M., Davis, J., Edwards, L., Harrison, R. P., Hosemann, P., & Bhattacharyya, D. (2019). In situ Micro tensile testing of He +2 ion irradiated and implanted single crystal nickel film. https://www.sciencedirect.com/science/article/pii/S1359645415006059e8d1b9e18a5dfbb60ac5b2b0547f3cedhttps://www.elsevier.com/open-access/userlicense/1.0/2

Reznik, B., & Hüttinger, K. J. (2002). On the terminology for pyrolytic carbon. Carbon, 40(4), 621–624. https://doi.org/10.1016/S0008-6223(01)00282-2

Rinne, H. (2008). The Weibull Distribution : A Handbook. The Weibull Distribution. https://doi.org/10.1201/9781420087444

Rohbeck, N., & Xiao, P. (2016). Evaluation of the mechanical performance of silicon carbide in TRISO fuel at high temperatures. Nuclear Engineering and Design, 306, 52–58. https://doi.org/10.1016/j.nucengdes.2016.05.040

Sakata, T., Ogiwara, T., Takahashi, H., & Sekine, T. (1999). Investigation of Ga contamination due to analysis by dual beam FIB. Proceedings of the Asian Test Symposium, 389–393. https://doi.org/10.1109/ats.1999.810780

Shih, C., Katoh, Y., Leonard, K. J., Bei, H., & Lara-Curzio, E. (2013). Determination of interfacial mechanical properties of ceramic composites by the compression of micro-pillar test specimens. Journal of Materials Science, 48(15), 5219–5224. https://doi.org/10.1007/s10853-013-7311-z

Skerjanc, W. F., Maki, J. T., Collin, B. P., & Petti, D. A. (2016). Evaluation of design parameters for TRISO-coated fuel particles to establish manufacturing critical limits using PARFUME. Journal of Nuclear Materials, 469, 99–105. https://doi.org/10.1016/j.jnucmat.2015.11.027

Skewed Distribution: Definition & Examples - Statistics By Jim. (n.d.). Retrieved August 22, 2023, from https://statisticsbyjim.com/basics/skewed-distribution/

Stein, I. Y., Constable, A. J., Morales-Medina, N., Sackier, C. V., Devoe, M. E., Vincent, H. M., & Wardle, B. L. (2017). Structure-mechanical property relations of non-graphitizing pyrolytic carbon synthesized at low temperatures. Carbon, 117, 411–420. https://doi.org/10.1016/j.carbon.2017.03.001

Stempien, J. D., Hunn, J. D., Morris, R. N., Gerczak, T. J., & Demkowicz, P. A. (2021). AGR-2 TRISO Fuel Post-Irradiation Examination Final Report. http://www.ART.INL.gov

Ted Pella. (2020). Focused Ion Beam Sample Holder, FIB Lift-out Grids, Silicon Aperture Frames. In Ted Pella, Inc. https://www.tedpella.com/grids_html/4510half.htm.aspx#10FIBC05

THERMO FISHER SCIENTIFIC. (2021). Focused ion beam scanning electron microscope - Versa 3D. https://www.directindustry.com/prod/thermo-fisher-scientific-materials-structural/product-123345-1401265.html

Tivol, W. F. (2010). Selected Area Electron Diffraction and its Use in Structure Determination. Microscopy Today, 18(4), 22–28. https://doi.org/10.1017/s1551929510000441

van Rooyen, I. (n.d.). Statement of Work Effects of Neutron Irradiation on the Micro/Nano Scale Structure and Fission Product Distribution of TRISO-Coated Particle Fuel Kernels from AGR Experiments.

Van Rooyen I. (2011). Effects of Phosphorous Doping and Very High Temperature on the Nanostructures of Silicon Carbide and TRISO Coated Particles. Nelson Mandela Metropolitan University.

Van Rooyen, I. J., Dunzik-Gougar, M. L., Van, P. M., Trowbridge, R. T., Van Rooyen, P. M., & Trowbridge, T. (2012). On Techniques to Characterize and Correlate Grain Size, Grain Boundary Orientation and the Strength of the SiC Layer of TRISO Coated Particles: A Preliminary Study HTR 2012 On Techniques to Characterize and Correlate Grain Size, Grain Boundary Orientation and the Strength of the SiC Layer of TRISO Coated Particles: A Preliminary Study.

van Rooyen, I. J., Fu, Z., Yang, Y., Holesinger, T. G., Bachhav, M., van Rooyen, I. J., Yang, Y., & Bachhav, M. (2018). Microstructure and Fission Product Distribution Examination in the UCO Kernel of TRISO Fuel Particles Microstructure and Fission Product Distribution Examination in the UCO Kernel of TRISO Fuel Particles Microstructure and Fission Product Distribution Examination in the UCO Kernel of TRISO Fuel Particles. http://www.inl.gov

van Rooyen, I. J., Lillo, T. M., Wen, H. M., Hill, C. M., Holesinger, T. G., Wu, Y. Q., Aguiara, J. A., & Aguiar, J. A. (2016). MICRO/NANO-STRUCTURAL EXAMINATION AND FISSION PRODUCT IDENTIFICATION IN NEUTRON IRRADIATED AGR-1 TRISO FUEL 2016 International Topical Meeting on High Temperature Reactor Technology (HTR

2016) MICRO/NANO-STRUCTURAL EXAMINATION AND FISSION PRODUCT IDENTIFICATION IN NEUTRON IRRADIATED AGR-1 TRISO FUEL.

van Rooyen, I. J., Lillo, T. M., & Wu, Y. Q. (2014). Identification of silver and palladium in irradiated TRISO coated particles of the AGR-1 experiment. Journal of Nuclear Materials, 446(1–3), 178–186. https://doi.org/10.1016/j.jnucmat.2013.11.028

van Rooyen, I. J., Miller, B., Janney, D., Riesterer, J., Demkowicz, P., Harp, J., & Ploger, S. A. (2012). Electron Microscopic Examination of Irradiated TRISO Coated Particles of Compact 6-3-2 of AGR-1 Experiment. http://www.inl.gov

van Rooyen, I. J., Nabielek, H., Neethling, J. H., Kania, M. J., & Petti, D. A. (2014). Progress in Solving the Elusive Ag Transport Mechanism in TRISO Coated Particles: "What is new?" (HTR2014-31261). Proceedings of the HTR 2014, Weihai, China, October 2014, Paper 31261.

Van Rooyen, I. J., Neethling, J. H., & Van Rooyen, P. M. (2010). The influence of annealing temperature on the strength of TRISO coated particles. Journal of Nuclear Materials, 402(2–3), 136–146. https://doi.org/10.1016/j.jnucmat.2010.05.009

Verfondern, K., Nabielek, H., Kania, M. J., & Allelein, H.-J. für E. K. N. E. und R. (IEK-6). (2013). High-quality Thorium TRISO fuel performance in HTGRs (Vol. 174). Forschungszentrum Jülich GmbH Zentralbibliothek. https://juser.fz-juelich.de/record/136815/files/FZJ-2013-03397.pdf

Vo, H. T., Reichardt, A., Frazer, D., Bailey, N., Chou, P., & Hosemann, P. (2017). In Situ Micro-Tensile Testing on Proton Beam-Irradiated Stainless Steel. http://www.elsevier.com/open-access/userlicense/1.0/

Was, G. S. (Ed.). (2007). Irradiation-Induced Voids and Bubbles. In Fundamentals of Radiation Materials Science: Metals and Alloys (pp. 343–431). Springer Berlin Heidelberg. https://doi.org/10.1007/978-3-540-49472-0_8

Wavelength-dispersive spectroscopy (WDS). (n.d.). Retrieved February 19, 2023, from https://serc.carleton.edu/research_education/geochemsheets/wds.html

Wei, H., Zhang, J., Jian, X., Zhang, Y., Li, L., Ding, S., & Ren, Q. (2021). Effects of the key parameters of TRISO particle buffer layer on in-pile thermo-mechanical behavior in FCM fuel pellets. Journal of Nuclear Materials, 551. https://doi.org/10.1016/j.jnucmat.2021.152977

Wen, H., van Rooyen, I. J., Hill, C. M., Trowbridge, T. L., & Coryell, B. D. (2015). Fission products distribution in triso coated fuel particles irradiated to 3.22 x 1021 n/cm2 fast fluence at 1092°c. ASME 2015 Nuclear Forum, NUCLRF 2015, Collocated with the ASME 2015 Power Conference, the ASME 2015 9th International Conference on Energy Sustainability, and the ASME 2015 13th International Conference on Fuel Cell Science, Engineering and Technology. https://doi.org/10.1115/NUCLRF201549695

Wereszczak, A. A., Jadaan, O. M., Lin, H. T., Champoux, G. J., & Ryan, D. P. (2007). Hoop tensile strength testing of small diameter ceramic particles. In Journal of Nuclear Materials (Vol. 361, Issue 1, pp. 121–125). https://doi.org/10.1016/j.jnucmat.2006.11.013

Wolff, A. (2020). Focused ion beams: An overview of the technology and its capabilities - 2020 - Wiley Analytical Science. https://analyticalscience.wiley.com/do/10.1002/was.00070009

Wolfgong, W. J. (2016). Chemical analysis techniques for failure analysis: Part 1, common instrumental methods. In Handbook of Materials Failure Analysis with Case Studies from the

Aerospace and Automotive Industries (pp. 279–307). Elsevier Inc. https://doi.org/10.1016/B978-0-12-800950-5.00014-4

Wright, K. E., Stempien, J. D., & van Rooyen, I. J. (2021). EPMA-based mass balance method for quantitative fission product distribution comparison between TRISO particles. MRS Advances, 6(47–48), 1020–1025. https://doi.org/10.1557/s43580-021-00166-2

Wright, K. E., Stempien, J., Jiang, W., & van Rooyen, I. J. (2022). Fission product distribution in irradiated safety-tested and as-irradiated AGR-2 TRISO particles. Journal of Nuclear Materials, 559. https://doi.org/10.1016/j.jnucmat.2021.153468

Wright, K. E., & van Rooyen, I. J. (2016). ELECTRON PROBE MICROANALYSIS OF IRRADIATED AND 1600°C SAFETY-TESTED AGR-1 TRISO FUEL PARTICLES WITH LOW AND HIGH RETAINED 110M AG 2016 ANS Winter Meeting and Nuclear Technology Expo ELECTRON PROBE MICROANALYSIS OF IRRADIATED AND 1600°C SAFETY-TESTED AGR-1 TRISO FUEL PARTICLES WITH LOW AND HIGH RETAINED 110M AG.

Zhang, H., López-Honorato, E., & Xiao, P. (2015). Fluidized bed chemical vapor deposition of pyrolytic carbon-III. Relationship between microstructure and mechanical properties. Carbon, 91, 346–357. https://doi.org/10.1016/j.carbon.2015.05.009

Zhang, X., Zhong, L., Mateos, A., Kudo, A., Vyatskikh, A., Gao, H., Greer, J. R., & Li, X. (2019). Theoretical strength and rubber-like behaviour in micro-sized pyrolytic carbon. Nature Nanotechnology, 14(8), 762–769. https://doi.org/10.1038/s41565-019-0486-y

Zuo, J.-M. (2006). Electron Nanocrystallography. In Handbook of Microscopy for Nanotechnology (pp. 567–599). Kluwer Academic Publishers. https://doi.org/10.1007/1-4020-8006-9_18